INTERNATIONAL ATOMIC ENERGY AGENCY
INTERNATIONAL CENTRE FOR THEORETICAL PHYSICS

SMR: 960/8

WORKSHOP ON NONLINEAR CONTROL AND CONTROL OF CHAOS

(17 - 28 June 1996)

"Nonlinear Dynamics in Chemistry and Control of Chaos"

presented by:

Kenneth Showalter

West Virginia University
Department of Chemistry
Morgantown, West Virginia 26506-6045
U.S.A.

Controlling chaos in the Belousov-Zhabotinsky reaction

Valery Petrov, Vilmos Gáspár, Jonathan Masere
& Kenneth Showalter

Reprinted from Nature, Vol. 361, January 21, 1993 Issue

Controlling chaos in the Belousov–Zhabotinsky reaction

Valery Petrov, Vilmos Gáspár*, Jonathan Masere & Kenneth Showalter*

Department of Chemistry, West Virginia University, Morgantown, West Virginia 26506-6045, USA

DETERMINISTIC chaos is characterized by long-term unpredictability arising from an extreme sensitivity to initial conditions. Such behaviour may be undesirable, particularly for processes dependent on temporal regulation. On the other hand, a chaotic system can be viewed as a virtually unlimited reservoir of periodic behaviour which may be accessed when appropriate feedback is applied to one of the system parameters[1]. Feedback algorithms have now been successfully applied to stabilize periodic oscillations in chaotic laser[2], diode[3], hydrodynamic[4] and magnetoelastic[5] systems, and more recently in myocardial tissue[6]. Here we apply a map-based, proportional-feedback algorithm[7,8] to stabilize periodic

* Permanent address of V. G. is: Department of Physical Chemistry, Kossuth L. University, PO Box 7, 4010 Debrecen, Hungary. Correspondence should be addressed to K.S.

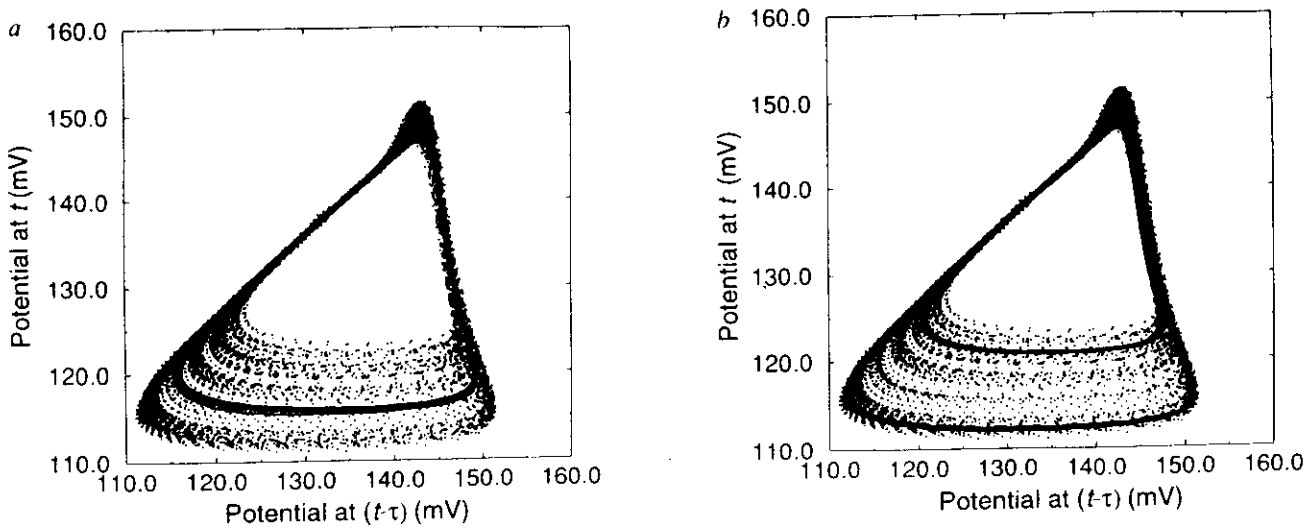

FIG. 1 Stabilized period-1 and period-2 limit cycles embedded in strange attractor of the BZ reaction. Scattered points show chaotic trajectory in time-delay phase space ($\tau = 13$ s) with a reactor residence time of 2.8×10^3 s and concentrations, after mixing, of [malonic acid] $= 2.22 \times 10^{-1}$ M, $[Ce_2(SO_4)_3] = 4.50 \times 10^{-4}$ M, $[NaBrO_3] = 1.02 \times 10^{-1}$ M and $[H_2SO_4] = 0.200$ M. Solid curves show (*a*) period-1 limit cycle stabilized by using $A_s = 33.0$ mV and $g = 18.0$ in equation (1) and (*b*) period-2 limit cycle stabilized by using $A_s = 26.9$ mV and $g = 33.4$. Reaction was carried out in a continuously stirred tank reactor (volume 34.0 ml, stirring rate 1,800 r.p.m.) maintained at 28.0 ± 0.1 °C and fed with separate solutions of malonic acid, cerous sulphate and sodium bromate. Two peristaltic pumps were used, with the malonic acid solution delivered at a fixed flow rate by one, and the cerium and bromate solutions (acidified with sulphuric acid) delivered by the other at a rate regulated by a computer. The potential of a bromide-ion-selective electrode was monitored and collected at a frequency of 10 Hz by a 16-bit data-acquisition board. Moving averages of 10 values were calculated and stored each second, and these values were numerically filtered using a 5-s characteristic period.

behaviour in the chaotic regime of an oscillatory chemical system: the Belousov–Zhabotinsky reaction.

The dynamical behaviour of a chaotic system can be visualized by the strange attractor (an attractor in which the trajectory never exactly repeats itself) traced out by its trajectory in phase space. An infinite number of unstable periodic orbits are embedded in such an attractor, each characterized by a distinct number of oscillations per period. In low-dimensional systems, these orbits are simple saddle-type limit cycles with an attracting stable manifold and a repelling unstable manifold. A general algorithm for stabilizing such orbits, based on targeting the stable manifold of the limit cycle by applying perturbations to a system constraint, has been developed by Ott, Grebogi and Yorke[1] (OGY). The stable manifold is found in a particular Poincaré section in the phase space, and it is targeted in this section each period of oscillation. For systems exhibiting low-dimensional chaos characterized by effectively one-dimensional maps, the OGY method can be reduced to a simple map-based algorithm[7,8]. The simplified method is more convenient in experimental applications because it minimizes the targeting procedures, and it has been used to control chaos in laser[2] and diode[3] systems.

The best-studied example of an oscillatory chemical system is the Belousov-Zhabotinsky (BZ) reaction, in which Ce(IV)/Ce(III) catalyses the oxidation and bromination of $CH_2(COOH)_2$ (malonic acid) by BrO_3^- in H_2SO_4. If the reaction is carried out in a continuous-flow stirred-tank reactor, the flow rate of the reactants into the tank ultimately determines whether the system exhibits steady-state, periodic or chaotic behaviour. Here we use conditions similar to the low-flow-rate Texas experiments[9–11], which ensure that the system is maintained within the chaotic regime (see Fig. 1). An important difference in our experiment is that we apply feedback to the system by perturbing the rate at which the cerium and bromate solutions are fed into the tank (the flow rate of the malonic acid being fixed), permitting the targeting and stabilization of periodic behaviour within the chaotic regime.

Figure 1*a* shows the strange attractor and the stabilized period-1 limit cycle for the BZ reaction. The time-delay phase portrait was reconstructed *in situ* from smoothed values of the potential of a bromide electrode. Except for small positive and negative perturbations to the flow rate of the bromate and cerium reactant stream, the operating conditions were identical for the chaotic and periodic behaviour. Figure 1*b* shows the stabilized period-2 limit cycle embedded in the strange attractor, again obtained with the same average reactant-stream flow rate. The oscillatory behaviour can be switched between period-1, period-2 and chaos by simple adjustments of the proportional feedback. Each time the controlling experiment was repeated (more than 10 times), a bifurcation diagram was first constructed to locate a suitably wide range of chaotic behaviour arising from a period-doubling cascade. The flow rate of the bromate and cerium reactant stream was chosen as the bifurcation parameter, as this choice gave the widest range of period-doubling chaos.

The control algorithm takes advantage of the predictable evolution of a chaotic system in the vicinity of a fixed point in the next-amplitude map, corresponding to a particular unstable periodic orbit. Shown in Fig. 2*a* is the next-amplitude map for the strange attractor and the period-1 orbit shown in Fig. 1*a*. The position of the period-1 fixed point is given by the intersection of the map with the bisectrix, where system state $A_{n+1} = A_n$. As the chaotic system traverses the attractor, the region near the fixed point is eventually visited, and the control algorithm is then activated. Control is achieved by perturbing a system constraint such that the fixed point is targeted on each return.

A shift of the map occurs on varying a system constraint, and this shift can be used to target any particular fixed point. Shown in Fig. 2*b* is a next-amplitude map constructed from the Györgyi-Field[12] model of the BZ reaction with concentrations and residence time similar to the experimental values for Fig. 2*a*. The inset shows a blowup of the map around the period-1 fixed point (right) and the shifted map (left) obtained at a slightly different value of the bifurcation parameter μ (the flow rate of the bromate and cerium reactant stream). For small perturbations, the shift in the linear region around the fixed point is directly proportional to the variation in μ. The map can therefore be shifted to target the fixed point by applying a

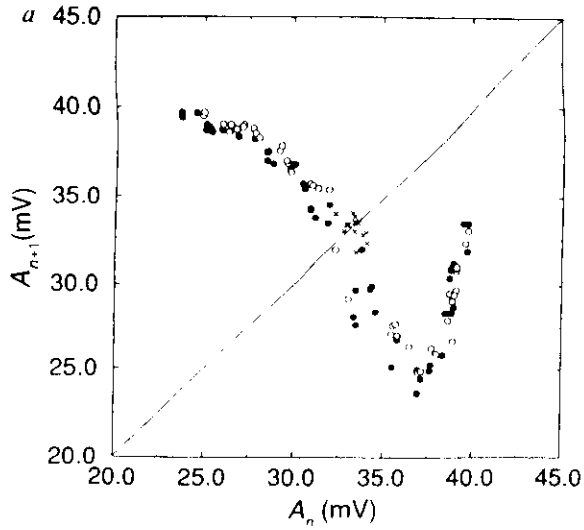

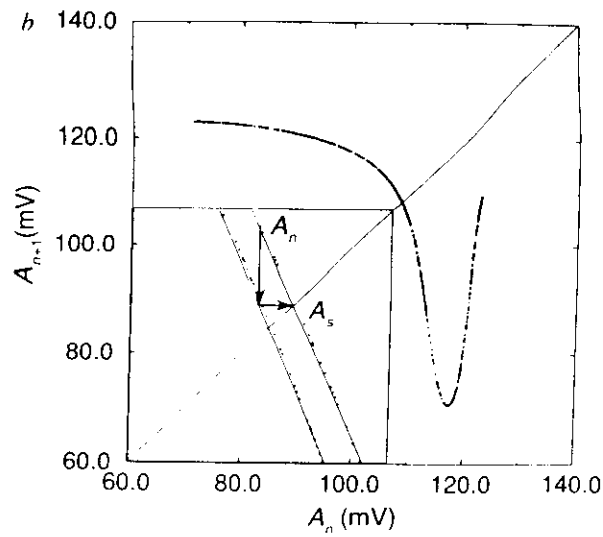

FIG. 2 *a*, Next-amplitude map before (●) and after (○) controlling period-1 and period-2, respectively, as shown in Figs 1 and 3*a*. Also shown are values (×) near fixed point during control corresponding to period-1 limit cycle trajectory in Fig. 1*a*. *b*, Next-amplitude map calculated from three-variable Györgyi–Field model of the BZ reaction with rate constants and residence time (2.17×10^3 s) the same as in ref. 12, and concentrations as in Fig. 1 except [malonic acid] = 0.24 M. Inset shows a 40-fold enlargement of map around fixed point (right) and shifted map (left) resulting from a 0.2% change in the flow rate of the bromate and cerium reactant stream. The system at state A_n is directed to A_s on the next return by varying μ according to equation (1) to shift map[7,8].

perturbation to the bifurcation parameter according to the difference between the system state A_n and the fixed point A_s

$$\Delta\mu = (A_n - A_s)/g \qquad (1)$$

where g is a constant. The current amplitude A_n is measured and with the value of A_s obtained from the map, the value of $\Delta\mu$ necessary for the fixed point to be targeted is calculated. The value of the proportionality constant g can be determined by measuring the horizontal distance between two maps constructed at slightly different values of μ (refs 7, 8), as shown in Fig. 2*b*. Various period-k limit cycles can be similarly stabilized by using the corresponding values of A_s and g (obtained from the appropriate maps of A_{n+k} against A_n) to determine $\Delta\mu$ in equation (1). The control algorithm may be implemented in several variations; for example, the perturbation determined every kth return may be applied for the entire period or for only a fraction of the period. In the stabilization of period-1 and period-2 shown in Fig. 1, the perturbation was applied for 15 s on each return.

Experimental fluctuations in the measured bromide potential result in significant scatter in the next-amplitude map, as shown in Fig. 2*a*. To reduce experimental noise, next-amplitude maps were used in the control algorithm rather than next-return maps; similar results were obtained with slightly more noise using

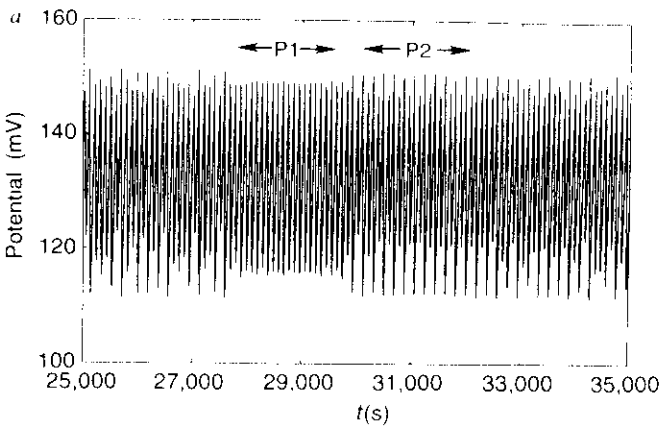

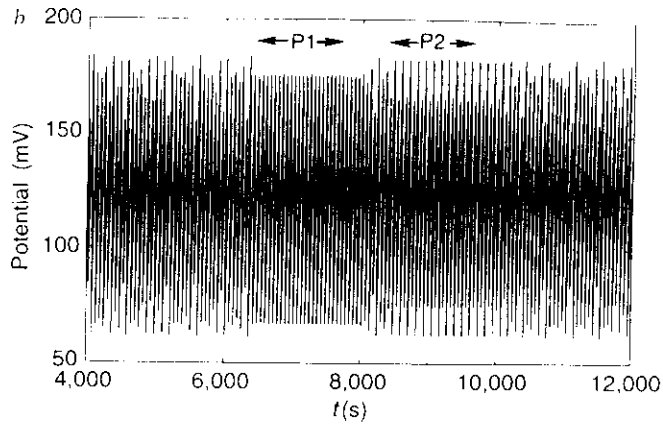

FIG. 3 *a*, Potential of bromide electrode as a function of time in BZ reaction with conditions given in Fig. 1. The control algorithm was switched on to stabilize period-1 at $t = 27{,}800$ s and switched off at $t = 29{,}500$ s, with the parameters corresponding to Fig. 1*a*. The parameters were changed at $t = 30{,}000$ s to stabilize period-2, with values corresponding to Fig. 1*b*, until $t = 32{,}100$ s when control was switched off. The control range was set at ±3.0 mV for both period-1 and period-2. *b*, Oscillations in bromide potential calculated from Györgyi–Field[12] model showing chaos, stabilized period-1 and period-2, and the reappearance of chaos. Potential calculated from the Nernst equation and bromide concentration assuming an Ag/AgCl reference electrode potential of 197 mV. Period-1 limit cycle stabilized by using $A_s = 108.25$ mV and $g = -9.0 \times 10^4$ and period-2 limit cycle stabilized by using $A_s = 90.235$ mV and $g = 7.0 \times 10^4$ in equation (1). Controlling algorithm was applied on each return for 25 s and the control range was set at ±5.0 mV. In both calculation and experiment, the flow rate of the bromate and cerium reactant stream was varied during control; a residence-time decrease of 1.0% therefore gives rise to an increase in these concentrations of 0.5% and a decrease in the malonic acid concentration of 1.0%. The typical residence-time variation during control was ~1.0% in experiment and ~10^{-5}% in calculation.

next-return maps. Although the experimental uncertainty seems to be comparable to that in previously reported maps for chaos in the BZ reaction[9,10], the scatter prevented the direct measurement of the proportionality constant g. The value of g was therefore estimated from the shift of A_s with variation of μ in the bifurcation diagram, and the final value was determined by adjustments around the initial estimate. Once the values for the fixed points and corresponding proportionality constants had been determined, the system could be switched between period-1 and period-2 behaviour and chaos by appropriately changing the values. Figure 3*a* shows the effect of the control algorithm, with the stabilization of the period-1 limit cycle followed by the period-2 limit cycle and the reappearance of chaotic behaviour when control was switched off. Transient aperiodic oscillations appear between period-1 and period-2 as the system leaves the period-1 orbit to arrive eventually at the control range of the period-2 orbit. When control was switched off, the chaotic behaviour was much the same as before the application of the feedback algorithm (Fig. 2*a*). Calculated behaviour using the Györgyi–Field[12] model is shown in Fig. 3*b*, with the stabilization of period-1 followed by period-2 and then a return to chaotic behaviour.

The stabilization of periodic orbits in chaotic systems by imposed feedback was first proposed by Ott, Grebogi and Yorke[1], and implications for biological self-regulation as well as practical uses such as convenient waveform generation have been pointed out[1–6]. The quenching techniques of Sørensen and Hynne[13–15] for targeting the unstable stationary state following a supercritical Hopf bifurcation are closely related to the OGY method. These authors have also successfully targeted the period-1 orbit in the BZ system following the initial period-doubling bifurcation, resulting in the transient appearance of these oscillations[15]. The map-based algorithm is more convenient than the OGY method for some experimental settings. (The OGY method has successfully been applied to stabilize period-1 in our BZ experiment, with results similar to those shown in Fig. 1*a*.) The map-based algorithm is especially useful in controlling high-frequency chaos, such as in laser[2] and diode[3] systems. In these applications, as well as in our present experiments, it is advantageous to apply the controlling perturbation for only a fraction of the oscillatory period. The system is attracted by the stable manifold of the unstable limit cycle during the perturbation-free fraction, thereby reducing the targeting error by ensuring that it resides effectively on the unstable manifold on its next return.

An important feature of both the OGY method and the map-based algorithm is that no knowledge of the underlying dynamics of a system (that is, the governing differential equations) is necessary for stabilizing any particular periodic orbit. This feature can be exploited to characterize experimentally the bifurcation behaviour of a chaotic (or periodic) system by tracking the unstable orbits as a bifurcation parameter is varied. The technique is similar to the computational algorithm AUTO[16] for exploring the bifurcation behaviour of model systems.[17] The tracking algorithm based on stabilizing periodic orbits, however, does not depend on model descriptions. We have made preliminary investigations of the BZ reaction using this technique with promising results; period-1 can easily be tracked after the first period-doubling bifurcation. □

Received 15 October; accepted 11 December 1992.

1. Ott, E., Grebogi, C. & Yorke, J. A. *Phys. Rev. Lett.* **64,** 1196–1199 (1990).
2. Roy, R., Murphy, T. W., Maier, T. D., Gills, Z. & Hunt, E. R. *Phys. Rev. Lett.* **68,** 1259–1262 (1992).
3. Hunt, E. R. *Phys. Rev. Lett.* **67,** 1953–1955 (1991).
4. Singer, J., Wang, Y.-Z. & Bau, H. H. *Phys. Rev. Lett.* **66,** 1123–1125 (1991).
5. Ditto, W. L., Rauseo, S. N. & Spano, M. L. *Phys. Rev. Lett.* **65,** 3211–3214 (1990).
6. Garfinkel, A., Spano, M. L., Ditto, W. L. & Weiss, J. N. *Science* **257,** 1230–1235 (1992).
7. Peng, B., Petrov, V. & Showalter, K. *J. phys. Chem.* **95,** 4957–4959 (1991).
8. Petrov, V., Peng, B. & Showalter, K. *J. chem. Phys.* **96,** 7506–7513 (1992).
9. Simoyi, R. H., Wolf, A. & Swinney, H. L. *Phys. Rev. Lett.* **49,** 245–248 (1982).
10. Coffmann, K. G., McCormick, W. D., Noszticzius, Z., Simoyi, R. H. & Swinney, H. L. *J. chem. Phys.* **86,** 119–129 (1987).
11. Noszticzius, Z., McCormick, W. D. & Swinney, H. L. *J. phys. Chem.* **91,** 5129–5134 (1987).
12. Györgyi, L. & Field, R. J. *Nature* **355,** 808–810 (1992).
13. Hynne, F. & Sørensen, P. G. *J. phys. Chem.* **91,** 6573–6575 (1987).
14. Sørensen, P. G. & Hynne, F. *J. phys. Chem.* **93,** 5467–5474 (1989).
15. Sørensen, P. G., Hynne, F. & Nielsen, K. *Reaction Kinet. Catal. Lett.* **42,** 309–315 (1990).
16. Doedel, E. *AUTO: Software for Continuation and Bifurcation Problems in Ordinary Differential Equations* (Applied Mathematics, California Institute of Technology, Pasadena, 1986).
17. Petrov, V., Scott, S. K. & Showalter, K. *J. chem. Phys.* **97,** 6191–6198 (1992).

ACKNOWLEDGEMENTS. We thank the NSF and the Hungarian Academy of Sciences for financial support, and the donors of The Petroleum Research Fund, administered by the ACS, for partial support of this research. We also thank S. K. Scott, Z. Noszticzius and R. H. Simoyi for discussions.

Tracking Unstable Periodic Orbits in the Belousov-Zhabotinsky Reaction

Valery Petrov, Michael J. Crowley, and Kenneth Showalter
Department of Chemistry, West Virginia University, Morgantown, West Virginia 26506-6045
(Received 20 December 1993)

An adaptive control algorithm for tracking unstable periodic orbits is presented. Automatic tracking is made possible by incorporating a stability-analysis subroutine into a map-based control scheme. The method is used to track unstable orbits in the Belousov-Zhabotinsky reaction.

PACS numbers: 82.40.Bj, 05.45.+b

Dynamical systems are typically characterized by systematic measurements of their asymptotic behavior as a function of a system parameter. The resulting constraint-response diagram provides insights into the system's bifurcation structure, i.e., the bifurcations that underlie the changes in qualitative dynamical behavior [1]. Successively varying other system parameters generates additional bifurcation diagrams, allowing the construction of phase diagrams of the behavior. Such measurements provide information about the *stable states* of a system. If an accurate model exists, a more detailed picture of the dynamics—including information about the *unstable states*—can be developed through the use of continuation methods [2].

A different approach for characterizing dynamical systems has become possible with newly developed techniques for stabilizing unstable periodic orbits in experimental systems, such as the Ott-Grebogi-Yorke (OGY) method [3,4] and related map-based schemes [5–7]. These control algorithms permit the stabilization of unstable states without relying on model descriptions. By tracking the unstable states and combining the measurements with measurements of the stable states, features of the bifurcation structure of a system can be determined before any modeling studies are carried out.

The first experiments on tracking unstable states were carried out using electronic and laser systems. Carroll *et al.* [8] reported tracking unstable periodic orbits in a chaotic Duffing circuit, and Gills *et al.* [9] reported tracking unstable stationary states in a chaotic multimode laser in which the range of stable lasing was significantly extended.

We present a new tracking algorithm, which determines the stability properties as well as the location of the unstable states. Automatic tracking is made possible by incorporating a stability-analysis subroutine into a map-based control scheme [5,6]. The procedure is tested in an experimental setting by tracking unstable periodic orbits in the Belousov-Zhabotinsky (BZ) reaction as a laboratory control parameter is varied. The experimental methods of previous control experiments, where periodic orbits were targeted and stabilized within the chaotic regime of the BZ reaction [10], serve as the basis for the tracking experiments reported here.

Tracking procedures offer new possibilities for control and characterization of dynamical systems. As in previous control methods [3–7], only tiny perturbations are necessary to stabilize a particular unstable state; hence, the states are representative of the original autonomous system. Tracking allows the stabilization of unstable states outside the chaotic regime, as a particular state can be followed through a complete bifurcation sequence —from the point where it becomes unstable to the point where it regains stability. In addition, as an unstable periodic orbit is tracked the Floquet multiplier (in the unstable direction) can be automatically determined by the stability-analysis subroutine described below.

The map-based control method is appropriate for stabilizing periodic orbits in low-dimensional, highly dissipative chaotic systems [5,6]. Rather than targeting the stable manifold of the fixed point in the Poincaré section as in the OGY algorithm [3,4], the method is based on targeting the fixed point directly in the 1D return map. For systems described by effectively 1D maps, the behavior in the local vicinity of a fixed point obeys linear dynamics according to the map

$$X_{n+1}=\lambda(X_n-X_F)+X_F\,, \tag{1}$$

where X_n is the value of the measured observable on the nth iteration, X_F is the fixed point, and λ is its Floquet multiplier. We assume there is an experimentally accessible parameter, p, which alters the dynamics in such a way that the fixed point moves in the direction of the unstable manifold when a small perturbation, δp, is applied. Following the application of such a perturbation, the system evolves according to the position of the shifted fixed point,

$$X_F(p+\delta p)=X_F(p)+\frac{\partial X_F}{\partial p}\delta p\,. \tag{2}$$

A particular unstable fixed point, X_F, is stabilized by determining the perturbation δp such that the next return, $X_{n+1}(p+\delta p)$, is equal to $X_F(p)$. The appropriate δp is simply proportional to the deviation of the system from X_F,

$$\delta p=K_0[X_n-X_F(p)]\,, \tag{3}$$

where the proportionality factor,

$$K_0=\frac{\lambda}{(\lambda-1)\,\partial X_F/\partial p}\,, \tag{4}$$

0031-9007/94/72(18)/2955(4)$06.00

is determined in advance from the horizontal shift of the return map resulting from the perturbation δp [5]. Perfect control would occur—if there were no measurement or targeting errors—with all X near X_F mapping to X_F, and the system in the local region of X_F would be described by a new map of zero slope [6].

Control is also possible for other values of the proportionality constant, K_S. For any value of K_S applied during control, the system evolves within the linear region of X_F according to

$$X_{n+1}=S(X_n-X_F)+X_F, \tag{5}$$

where the local slope S of the new map is related to K_S by

$$S=\lambda+\frac{\partial X_F}{\partial p}K_S(1-\lambda). \tag{6}$$

Thus, the fixed point is stabilized for any K_S that produces a slope S with magnitude less than unity, or, conversely, the multiplier S of the fixed point under control can be set to any value by the appropriate choice of K_S. This relationship allows the values of S, K_S, and λ to be determined while the unstable fixed point remains under control.

It is first necessary to initialize the tracking procedure, i.e., locate and stabilize a desired unstable orbit at some value of the bifurcation parameter q. (We distinguish between the control parameter p and bifurcation parameter q because they need not be the same.) The starting point can be located either in the vicinity of a bifurcation that destabilizes the periodic orbit, or in chaos, where the evolution of the system ensures that the local vicinity of the fixed point will be visited. In both cases, the location of the fixed point and value of the Floquet multiplier can be readily determined.

Tracking X_F through changes in the bifurcation parameter requires adaptive control, where the values of X_F and K_0 must be redetermined without the system leaving the local vicinity of X_F (where the control algorithm is effective). The control algorithm is continuously applied throughout the change in q in order to maintain control. Provided the change from q to $q'=q+\delta q$ is sufficiently small, the new X_F and λ are close to the previous values and linear behavior around the fixed point can be assumed. The value $K_0(q)$ and $X_F(q)$ used in the previous step, however, will be incorrect for convergence to the new $X_F(q')$. Consider the effect of using $K_0(q)$ and $X_F(q)$ in Eq. (3) for the system at q'. With these values, the system will converge to a point that is distinct from both the old $X_F(q)$ and the new $X_F(q')$. It can be shown that if the convergence is to the value $X^*(q')$, the value of $X_F(q')$ is given by

$$X_F(q')=\frac{X^*(q')-\lambda(q)X_F(q)}{1-\lambda(q)}, \tag{7}$$

where the values of $X_F(q)$ and $\lambda(q)$ are known from the previous step.

With the new fixed point known, the next step is to determine the appropriate value of the proportionality constant for the control algorithm, $K_0(q')$, and the new multiplier, $\lambda(q')$. One could determine the value of λ by switching off control and simply allowing the system to diverge; in experimental settings, however, this approach often fails because the system leaves the linear region of the fixed point too quickly, especially for highly unstable orbits. A systematic method for determining the new K_0 and λ utilizes the relationship given by Eq. (6). The proportionality constant K_S is first set to a value, K_1, that will produce a slightly unstable fixed point, e.g., with $|S|\approx 1.5$. The divergence from X_F is mild, allowing enough returns to the section for an accurate determination of the slope S_1. Before the system has diverged beyond the linear control range, K_S is changed to a new value, K_2, which corresponds to a mildly stable fixed point, e.g., with $|S|\approx 0.6$. The system will slowly converge back to X_F and the slope, S_2, is determined. The experimental measurements during the divergence/convergence scheme are then used with Eqs. (4) and (6) to yield

$$K_0=\frac{S_2K_1-S_1K_2}{S_2-S_1} \tag{8}$$

and

$$\lambda=\frac{S_2K_1-S_1K_2}{K_1-K_2}. \tag{9}$$

These steps, redetermining X_F and finding the corresponding values K_0 and λ from the stability analysis, can be reiterated in each step of the tracking until satisfactory convergence is achieved.

We now demonstrate the tracking algorithm with the Belousov-Zhabotinsky reaction in a continuous-flow, stirred tank reactor (CSTR). This system displays a variety of dynamical responses, including period-doubling cascades to chaos [11] and complex mixtures of mixed-mode oscillations and chaos [12,13]. The procedure will first be illustrated with the Györgyi-Field [14] model of the BZ reaction, with the parameters similar to those used in the experimental system. A typical bifurcation diagram of this model is shown in Fig. 1(a), where a period-doubling sequence from period-1 oscillations to chaos is followed by the reverse sequence to simple period 1. The period-1 orbit loses stability at the first period-doubling bifurcation; the locus of the unstable orbit, however, is readily determined by the tracking procedure. The open circles show the location of the stabilized orbit at each incremental increase in the bifurcation parameter q (the reciprocal residence time). The corresponding locus, shown by the solid line, was determined by the path-following algorithm AUTO [2]. The Floquet multiplier for the period-1 orbit, calculated from Eq. (9), is shown as a function of q by the open circles in Fig. 1(b). The values calculated from AUTO are shown by the solid line.

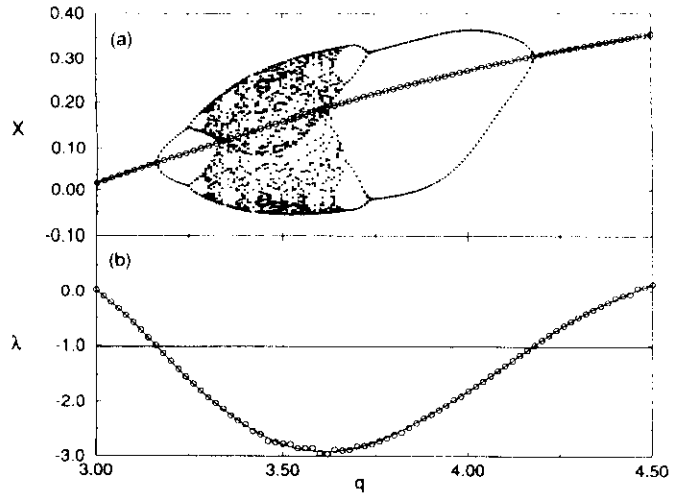

FIG. 1. Period-doubling sequence calculated from the three-variable Györgyi-Field [14] model of the Belousov-Zhabotinsky reaction. (a) Bifurcation diagram showing maximum in oscillations (●) of variable $X=\log_{10}([\mathrm{Ce(IV)}]\xi)$ as a function of the bifurcation parameter $q=1/10^{-4}\tau$, where ξ is a scaling constant and τ is the residence time. The open circles show the locus of the unstable period-1 orbit. (b) Values of period-1 Floquet multiplier as a function of q. The parameters used in the calculation are the same as in Ref. [14] except [malonic acid] $=0.26M$.

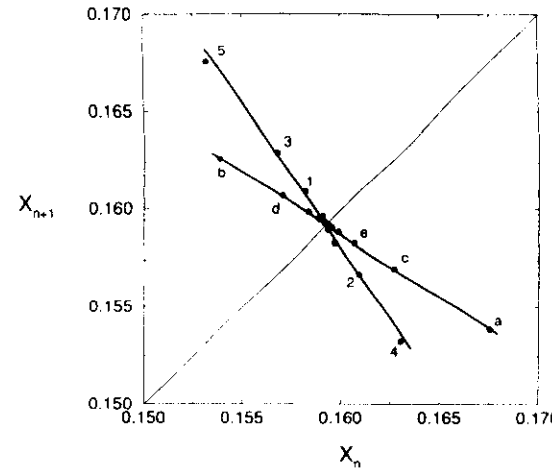

FIG. 2. Return map showing linear dynamics under control for two different values of K in the vicinity of the period-1 fixed point. The proportionality constant was first set to $K_1=8.369\times10^{-4}$ and then to $K_2=1.460\times10^{-3}$. The corresponding values of S_1 and S_2 in Eqs. (8) and (9) yield the values $K_0=1.915\times10^{-3}$ and $\lambda=-2.766$ for the tracking step at $q=3.5$ in Fig. 1.

Each step of the tracking consisted of determining the new fixed point according to Eq. (7) followed by the stability analysis according to Eqs. (8) and (9). An example of the stability analysis for one step of the tracking in Fig. 1 is shown in Fig. 2. The value of K is first set to K_1 to generate a slope $S_1\approx-1.5$, and the system diverges away from the fixed point (values $1,2,3,\ldots$). After sampling 5 points, the value of K is changed to K_2 to give a slope $S_2\approx-0.6$. The system converges back to the fixed point, generating another 5 points (values $a,b,c,\ldots$). Least-squares fits of each set of points allow the accurate determination of the slopes, $S_1=-1.557$ and $S_2=-0.6571$, which are then used in Eqs. (8) and (9) to calculate values of K_0 and λ corresponding to the value of the bifurcation parameter q. The updated K_0 and λ are used in the next step of the tracking in determining the new value of X_F.

An application of the tracking algorithm to the experimental system is shown in Fig. 3. The BZ reaction was carried out in a continuous-flow, stirred tank reactor (volume=60.0 ml, stirring rate=2700 rpm) maintained at 28.0 ± 0.1 °C. Two computer-regulated syringe pumps were used, with malonic acid solution delivered by one and cerium and bromate solutions (acidified with sulfuric acid) delivered by the other. The period-1 orbit was tracked from $q=0.452$ through the period-doubling, chaos, and period-halving sequences to $q=0.422$. The tracking was automatically carried out by a laboratory computer—collecting the data, executing the algorithm, and controlling the pumps. The period-doubling sequence to chaos and the reverse sequence are similar to the calculated sequences in Fig. 1; however, some qualitative differences are apparent. These are mainly due to monitoring a different system variable and using a slightly different bifurcation parameter in the experiments. The potential of a bromide selective electrode, giving the effective bromide ion concentration, was used to monitor the system. The bifurcation parameter q was the flow

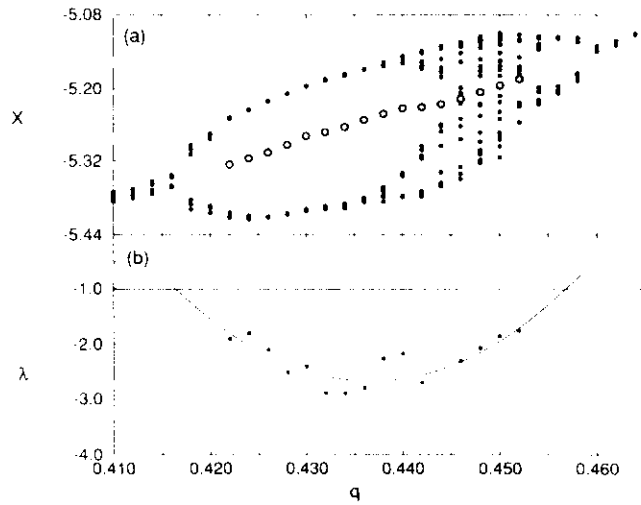

FIG. 3. Stable states (●) and tracked unstable period-1 orbit (○) of the BZ reaction as a function of bifurcation parameter q. The variable $X=\log_{10}[\mathrm{Br}^-]$ on crossing a Poincaré section defined by $\dot{X}=-5.66$ in the X_t, $X_{t+\tau}$ phase plane ($\tau=12$ s). Feedstream concentrations (before mixing) and flow rates: [malonic acid] $=0.222M$ at 0.444 mL/min; $[\mathrm{Ce_2(SO_4)_3}]=4.50\times10^{-4}M$, $[\mathrm{NaBrO_3}]=0.102M$, and $[\mathrm{H_2SO_4}]=0.300M$ varied at q mL/min.

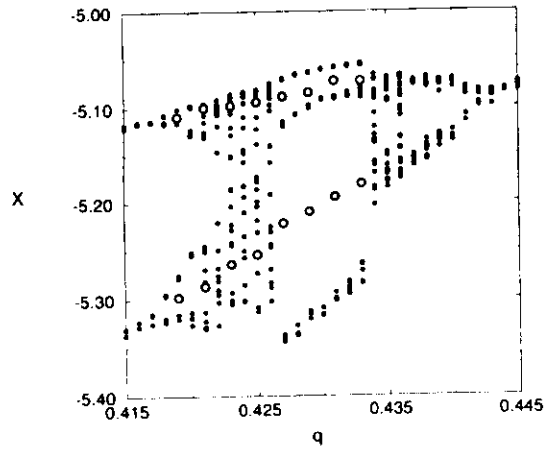

FIG. 4. Stable states (●) and tracked unstable period-2 orbit (○) in the BZ reaction. The monitored variable X and the bifurcation parameter q are the same as in Fig. 3 except the constant flow rate of the malonic acid solution was 0.440 mL/min.

rate of the Ce(III), bromate, and sulfuric acid feed streams (with the malonic acid flow rate held constant) [10]. The reactor residence time served as the perturbation parameter p.

Perturbations were applied during the first 25 s of each $\sim$100 s cycle to stabilize and track the period-1 orbit, shown in Fig. 3(a) by the open circles. The experimentally determined values for the period-1 Floquet multiplier as a function of q are shown in Fig. 3(b). Although there is significant scatter in the values of λ due to experimental fluctuations (from flow rate variations, etc.), the qualitative features of the dependence on q are similar to the modeling calculations shown in Fig. 1(b).

Figure 4 shows an example of tracking period 2 through a period-doubling cascade that gives rise to 2:1 mixed-mode oscillations (two large amplitude and one small amplitude oscillations per cycle [12,13]). Period-2 oscillations were stabilized after the period-doubling bifurcation at $q=0.419$ and tracked through chaos and the mixed-mode oscillations to $q=0.433$. The stabilization algorithm was robust and most effective when the perturbation was applied 80 s after crossing the Poincaré section, with a duration of 40 s, or about $\frac{1}{5}$ of the period.

The simplicity of map-based control methods offers significant advantages for the implementation of efficient tracking schemes. Linear map dynamics can also be used to stabilize and track stationary states. The temporal evolution of a two-variable system in the local vicinity of a focus stationary state is described by

$$X(t)=X_F+C\exp(\alpha t)\sin(\omega t+\varphi)\,, \tag{10}$$

where α is the real part and ω is the imaginary part of the eigenvalue. The exponential growth of $X(t)$ is modulated by sinusoidal oscillations, where the minima and maxima in X are equally spaced in time by $\Delta t=\pi/\omega$. The appearance of the extrema in the linear region of X is subject to the recursion law

$$X_{i+1}-X_F=\lambda(X_i-X_F)\,, \tag{11}$$

where X_{i+1} and X_i are the successive values and $\lambda=-\exp(\alpha\pi/\omega)$. The linear dynamics of the system near the stationary state can therefore be represented by a 1D map and the tracking algorithm can be easily applied. We report elsewhere [15] on stabilizing steady flame fronts through the chaotic regime of laminar combustion.

We thank the National Science Foundation (Grant No. CHE-9222616) for supporting this research. Acknowledgement is made to the donors of The Petroleum Research Fund, administered by the American Chemical Society, for partial support of this research.

[1] J. Guckenheimer and P. Holmes, *Nonlinear Oscillations, Dynamical Systems, and Bifurcations of Vector Fields* (Springer-Verlag, New York, 1983).

[2] E. J. Doedel, Congress Num. **30**, 265 (1981); E. J. Doedel and J. P. Kernevez, *AUTO: Software for Continuation and Bifurcation Problems in Ordinary Differential Equations* (Applied Mathematics, California Institute of Technology, Pasadena, 1986).

[3] E. Ott, C. Grebogi, and J. A. Yorke, Phys. Rev. Lett. **64**, 1196 (1990).

[4] T. Shinbrot, C. Grebogi, E. Ott, and J. A. Yorke, Nature (London) **363**, 411 (1993).

[5] B. Peng, V. Petrov, and K. Showalter, J. Phys. Chem. **95**, 4957 (1991).

[6] V. Petrov, B. Peng, and K. Showalter, J. Chem. Phys. **96**, 7506 (1992).

[7] R. W. Rollins, P. Parmananda, and P. Sherard, Phys. Rev. E **47**, R780 (1993).

[8] T. Carroll, I. Triandaf, I. B. Schwartz, and L. Pecora, Phys. Rev. A **46**, 6189 (1992).

[9] Z. Gills, C. Iwata, R. Roy, I. B. Schwartz, and I. Triandaf, Phys. Rev. Lett. **69**, 3169 (1992).

[10] V. Petrov, V. Gáspár, J. Masere, and K. Showalter, Nature (London) **361**, 240 (1993).

[11] R. H. Simoyi, A. Wolf, and H. L. Swinney, Phys. Rev. Lett. **49**, 245 (1982).

[12] R. A. Schmitz, K. R. Graziani, and J. L. Hudson, J. Chem. Phys. **67**, 3040 (1977).

[13] V. Petrov, S. K. Scott, and K. Showalter, J. Chem. Phys. **97**, 6191 (1992).

[14] L. Györgyi and R. J. Field, Nature (London) **355**, 808 (1992).

[15] V. Petrov, M. Crowley, and K. Showalter, J. Chem. Phys. (to be published).

Controlling spatiotemporal dynamics of flame fronts

Valery Petrov and Michael F. Crowley
Department of Chemistry, West Virginia University, Morgantown, West Virginia 26506-6045

Kenneth Showalter
Department of Chemistry, West Virginia University, Morgantown, West Virginia 26506-6045 and Service de Chimie Physique, Université Libre de Bruxelles, Campus Plaine, 1050 Bruxelles, Belgium

(Received 22 June 1994; accepted 1 July 1994)

In certain mixtures of fuel and oxidizer, propagating flame fronts may exhibit both stable and unstable cellular structures. Such flames represent spatially extended chemical systems, with coupling from diffusion of heat and reactants. A new algorithm is proposed that allows the stabilization and tracking of a steady, two-cell front through a bifurcation sequence that eventually leads to chaotic behavior. Periodic modes of the front can also be stabilized and tracked. The system is stabilized by monitoring one experimentally accessible variable and perturbing one boundary condition. No knowledge of the detailed dynamics of the system (i.e., the underlying governing equations) is required to implement the tracking method. The algorithm automatically provides information about the locations of the unstable steady states and periodic orbits and the magnitudes of the associated eigenvalues and Floquet multipliers.

I. INTRODUCTION

When a mixture of fuel and oxidizer is ignited, a wave of exothermic chemical reaction propagates through the mixture, producing heat and converting initial reactants into products. The planar front of a premixed flame, propagating through an initially motionless and homogeneous reaction mixture, may become unstable under certain conditions.[1-3] Two different types of instabilities arise: the hydrodynamic flame instability and the thermo-diffusive flame instability.[4] Hydrodynamic instabilities are caused by changes in density due to thermal expansion of the burned gas and are always present in large-scale flames. Thermo-diffusive instabilities arise from small-scale perturbations and depend on the presence of a reactant component with a sufficiently high molecular diffusivity.

We present an algorithm that can be used to stabilize steady flame fronts, suppressing the natural oscillatory behavior. It can also be used to stabilize periodic oscillations of the front that would otherwise be unstable. The algorithm utilizes a map-based tracking scheme that allows adaptive control of the system under slowly varying conditions.[5] To demonstrate the method we focus on the thermo-diffusive instability, neglecting the effects of thermal expansion by assuming the density of the gaseous mixture is everywhere constant.

In the thermo-diffusive instability, the flame front becomes nonplanar at a critical value of a system parameter such as the Lewis number. On further changing the parameter, the cellular front loses its stability to display spatiotemporal oscillations. The emergence of a period-doubling cascade in the two-cell front—and the control of such fronts—is the focus of this investigation. We study the control of two-dimensional premixed flames with a standard partial differential equation (PDE) model and a one-variable reduction of this model given by the Kuramoto–Sivashinsky equation. A description of the dynamical behavior of each system by a one-dimensional map allows the application of the tracking algorithm.

Several recent studies have reported control and tracking of unstable steady states in dynamical systems with many degrees of freedom. Gills *et al.*[6] reported tracking steady states in a chaotic multimode laser, thereby extending the range of stable lasing beyond that of the autonomous system. Unstable steady states and periodic orbits were tracked in a similar laser system by Glorieux and co-workers.[7] Hjelmfelt and Ross[8] stabilized and tracked unstable stationary states in a spatially extended chemical system with a linear feedback method that relies on a model description. We recently used a model-independent method to track unstable periodic orbits in the Belousov–Zhabotinsky (BZ) reaction in both the chaotic and complex-periodic parameter ranges.[5] The adaptive tracking algorithm is an extension of a map-based control method[9,10] that was previously used to control chaos in the BZ reaction.[11] The map-based scheme is a reduction of the Ott–Grebogi–Yorke (OGY) algorithm.[12,13]

The tracking algorithm is modified in this study to stabilize steady states and periodic orbits in spatiotemporal flame systems. In Sec. II, we describe the model systems and discuss some features of the calculations. We show how the behavior of a system near a focus-type steady state can be described by a one-dimensional map in Sec. III. Stabilizing and tracking unstable steady states and periodic orbits in the Kuramoto–Sivashinsky system and in the full PDE system are described in Secs. IV and V. We conclude in Sec. VI by describing potential applications of the method.

II. MODEL SYSTEMS

A. Reaction–diffusion model

Premixed flames with thermo-diffusive instabilities can be described by a system of two partial differential equations, one for temperature and the other for the concentration of a stoichiometrically deficient reactant:

 0021-9606/94/101(8)/6606/9/$6.00

$$\rho c_p \frac{\partial T}{\partial t} = \kappa \nabla^2 T + qW, \tag{1}$$

$$\frac{\partial C}{\partial t} = D_c \nabla^2 C - W. \tag{2}$$

Here, T is the temperature of the gaseous mixture, C is the concentration of the stoichiometrically deficient component, ρ is the density, c_p is the specific heat, κ is the thermal conductivity of the mixture, $\nabla^2 = \partial^2/\partial X^2 + \partial^2/\partial Y^2$ is the 2-D Laplacian operator, q is the heat release of the reaction, and D_c is the diffusion coefficient for the reactant C. The temperature dependence of the rate of chemical reaction W is given by an Arrhenius equation,

$$W = KC \exp(-E/RT), \tag{3}$$

where E is the activation energy, R is the universal gas constant, and the constant K includes the frequency factor and the concentration of the reactant in stoichiometric excess. The reaction zone is taken to be infinite in extent in the X coordinate ($-\infty < X < +\infty$) but of finite width L in the Y coordinate ($0 \leq Y \leq L$). We assume zero-flux boundary conditions at $Y = 0$ and L.

For convenience, we transform (1) and (2) into the dimensionless equations

$$\frac{\partial \theta}{\partial \tau} = \nabla^2 \theta + (1-\epsilon)\omega, \tag{4}$$

$$\frac{\partial s}{\partial \tau} = (1/\mathcal{L})\nabla^2 s - \omega, \tag{5}$$

where $\theta = T/T_b$ is the dimensionless temperature scaled by the final temperature T_b behind the front ($T_b = T_0 + qC_0/c_p\rho$, with T_0 the ambient temperature) and $\epsilon = T_0/T_b$; $s = C/C_0$ is the dimensionless concentration scaled by the concentration of reactant C_0 ahead of the front; $\tau = Kt$, $x = (K\rho c_p/\kappa)^{1/2} X$ and $y = (K\rho c_p/\kappa)^{1/2} Y$ are dimensionless time and spatial coordinates; $\omega = s \exp(-N/\theta)$ is the dimensionless reaction rate with $N = E/RT_b$; and $\mathcal{L} = \kappa/\rho c_p D_c$ is the Lewis number. The boundary conditions appropriate for the propagating front are

$$\begin{aligned} &s = 1, \quad \theta = \epsilon \quad \text{as} \quad x \to +\infty; \\ &s = 0, \quad \theta = 1 \quad \text{as} \quad x \to -\infty, \end{aligned} \tag{6}$$

where the front is moving in the positive x direction. The zero-flux boundary conditions in the y coordinate are

$$\frac{\partial s}{\partial y} = \frac{\partial \theta}{\partial y} = 0 \quad \text{at} \quad y = 0 \quad \text{and} \quad L. \tag{7}$$

It is convenient to introduce a traveling coordinate system in the x direction with a speed of the flame front v. This transformation adds a new term, $v\partial/\partial x$, to Eqs. (4) and (5):

$$\frac{\partial \theta}{\partial \tau} = \nabla^2 \theta + v\frac{\partial \theta}{\partial x} + (1-\epsilon)\omega, \tag{8}$$

$$\frac{\partial s}{\partial \tau} = (1/\mathcal{L})\nabla^2 s + v\frac{\partial s}{\partial x} - \omega. \tag{9}$$

The 1-D solution of Eqs. (8) and (9), calculated using finite differences for the $\partial/\partial x$ and $\nabla^2 = \partial^2/\partial x^2$ operators, is shown in Fig. 1. The limits of the grid in the x direction were set to cutoff values in order to carry out the integration. The boundary conditions become

$$\begin{aligned} &s = 1, \quad \theta = \epsilon \quad \text{at} \quad x = x^+; \\ &s = 0, \quad \theta = 1 \quad \text{at} \quad x = x^-, \end{aligned} \tag{10}$$

where the front is positioned near $x = 0$, and x^+ and x^- are the positive and negative cutoff coordinates. The steepness of the rate profile $\omega(x)$, which is due to the highly nonlinear Arrhenius temperature dependence, imposes a limit on the maximum value of the grid cell size. Both the grid cell size and the cutoff coordinates were varied to determine appropriate values for the study, where the front behavior is independent of the particular values chosen.

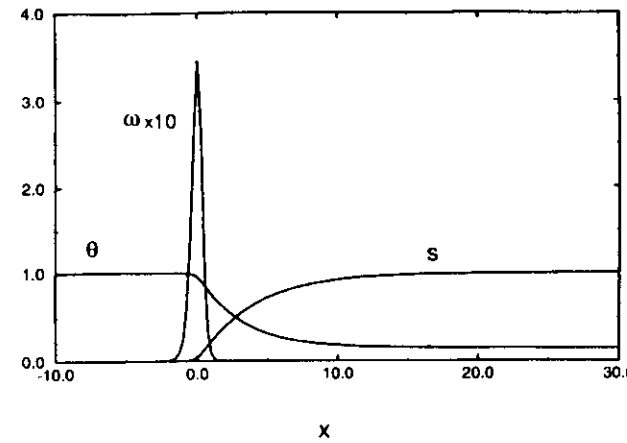

FIG. 1. Profiles of concentration s, temperature θ, and reaction rate ω in the 1-D propagating flame front. To visualize the profiles, the rate ω was rescaled by a factor of 10 and the dimensionless time and space coordinates were rescaled by setting the reaction rate $\omega = 10^{10}\, s \exp(-20/\theta)$ [which rescales time by a factor of 10^{10} and space by a factor of $(10^{10})^{1/2}$]. The asymptotic velocity of the front is 0.322; $\mathcal{L} = 0.8$, $\epsilon = 0.15$, $N = 20$.

The 2-D solution was calculated using an operator splitting method,[14] a two-step technique with implicit integration of reaction and diffusion terms in the x direction and explicit integration of diffusion terms in the y direction. Four iterations were typically required in each step of the integration for convergence, where the solution was effectively unchanged with further iterations. The operator splitting method was found to be three times faster than a standard implicit algorithm, which required the solution of large sparse matrices.

The 1-D wave profile shown in Fig. 1 is also a valid solution to the 2-D system, subject to the boundary conditions (6) and (7). Thus, steady planar fronts propagating in the x direction would be anticipated for the 2-D system. For certain experimental conditions, however, such planar flames become unstable, producing cellular structures that are either stationary or undergo periodic or chaotic motions.[3] These instabilities usually occur in mixtures containing relatively light reactants that are stoichiometrically deficient, e.g., lean hydrogen–oxygen flames. Instabilities may also occur in rich hydrocarbon flames if light, mobile chain carriers such as H-atoms are produced. The system described by Eqs. (8) and

(9) exhibits instabilities similar to those observed in real flames over a range of parameter values. However, because the numerical integration of the PDE model is computationally intensive, calculations were also carried out using the reduced model described below.

B. The Kuramoto–Sivashinsky equation

The 2-D system described by Eqs. (8) and (9) can be reduced to a single equation by assuming that reaction takes place in an infinitely narrow zone. A stability analysis of the PDEs shows that the (infinitely narrow) front becomes unstable when the diffusion of the fuel dominates over the heat conductance.[15] The condition for instability in terms of the Lewis number is given by

$$\mathcal{L}<1-2/N(1-\epsilon). \tag{11}$$

The reduction of Eqs. (8) and (9) to a single equation was developed by Sivashinsky[16] and Kuramoto.[17] The Kuramoto–Sivashinsky equation gives the temporal evolution of the front as a function of its spatial derivatives,

$$\frac{\partial\Psi}{\partial t}=\left(\frac{\partial\Psi}{\partial y}\right)^2-\frac{\partial^2\Psi}{\partial y^2}-\frac{\partial^4\Psi}{\partial y^4}, \tag{12}$$

with the dependent variable $\Psi(y,t)$ representing the contour of the front. The evolution equation, as it is written here, already satisfies the condition for the onset of instability. The only bifurcation parameter is the width of the reaction zone in the y direction.

An unusually rich sequence of bifurcations is exhibited by Eq. (12) as the width of the reaction zone is increased.[18] With no-flux boundary conditions, single- and multiple-cell structures are exhibited, each displaying spatiotemporal behavior ranging from steady to chaotic. We focus on the two-cell structure observed over the range $16.5\leq L\leq 18.5$ of the reaction zone width. Profiles of the front for three different values of L are shown in Fig. 2. The relative position of the local minimum in the profile serves as a convenient observable and its time trace is also plotted for each value of L. Figure 2(a) shows the steady front for $L=16.5$ with a symmetrical two-cell structure. This front shows no temporal variation. At $L=16.8$, the steady two-cell front loses stability through a Hopf bifurcation and begins to oscillate. A snapshot of the oscillatory front and the time trace of the local minimum are shown in Fig. 2(b) for $L=17.5$. Simple oscillations are exhibited at this reaction width. As the width is increased, a series of period doubling bifurcations leads to chaotic behavior, which appears at $L=18.1$. The front profile and the chaotic time series of the local minimum are shown in Fig. 2(c) for $L=18.3$. At $L=18.33$, the strange attractor is destroyed and randomly moving traveling waves in the profile are exhibited. The control method described in the next section allows suppression of the front oscillations over the entire range of L where the two-cell structure is observed.

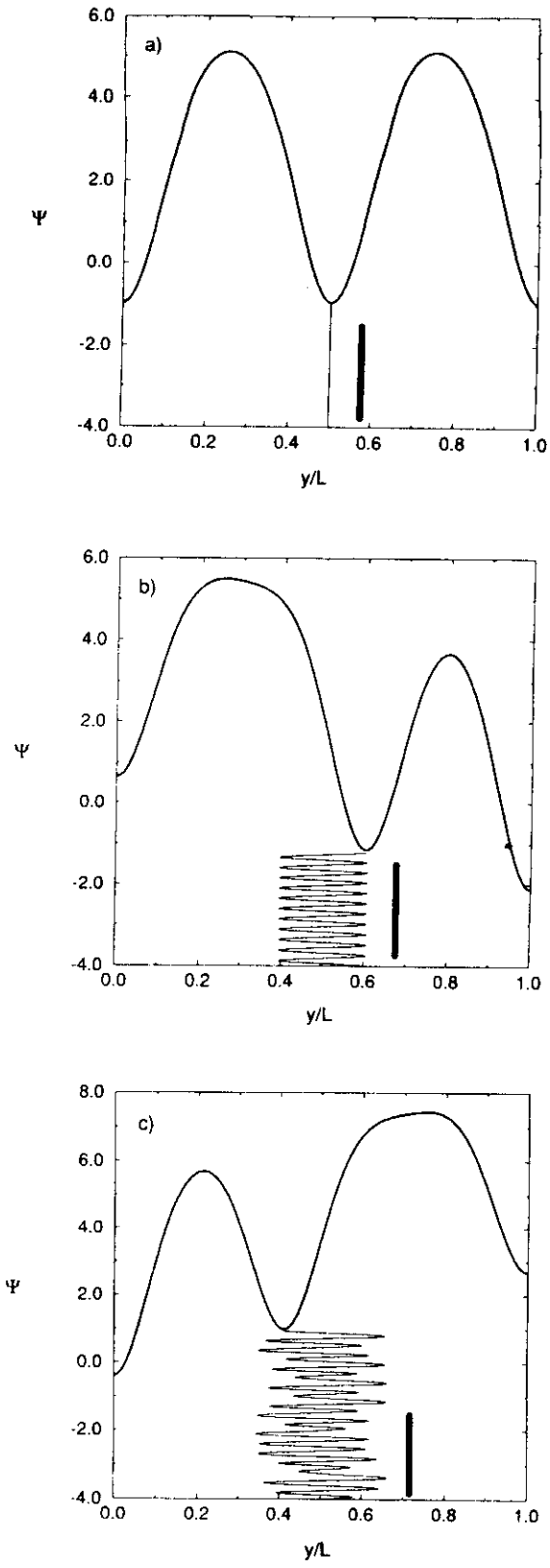

FIG. 2. Solution of the Kuramoto–Sivashinsky equation with no-flux boundary conditions showing steady (a), periodic (b), and chaotic (c) two-cell fronts for $L=16.5$, 17.5, and 18.3. The relative position of the local minimum in the profile is used to monitor the temporal evolution of the front. The time series in each figure shows the spatiotemporal motion of the minimum, with the vertical bar representing 100.0 dimensionless time units.

III. STABILIZATION AND TRACKING ALGORITHM

A. Stabilization of the steady state

The stabilization algorithm takes advantage of the linear evolution of a system in the proximity of a steady state. (The

stabilization of periodic orbits is discussed below in Sec. IV.) For an unstable focus, oscillations initially grow in a plane defined by the unstable manifold. In the local vicinity of the steady state, the system can therefore be treated as two-dimensional since trajectories are attracted to and remain in this plane. (We assume that all other manifolds of the steady state are stable.) We assign the variables ξ_1 and ξ_2 to the plane and describe the state of the system by the vector $\bar{\xi}$, with the focus steady state at $\bar{\xi}_F$:

$$\bar{\xi}=\begin{pmatrix}\xi_1\\ \xi_2\end{pmatrix}, \quad \bar{\xi}_F=\begin{pmatrix}0\\ 0\end{pmatrix}. \tag{13}$$

The evolution near the steady state is governed by the system of linear equations

$$\frac{\partial\bar{\xi}}{\partial t}=\mathbf{A}\bar{\xi}, \tag{14}$$

where $\mathbf{A}$ is a 2×2 matrix with a pair of complex-conjugate eigenvalues, $\alpha\pm i\omega$, giving solutions of the form

$$\bar{\xi}(t)=e^{\alpha t}[\bar{b}_1\sin(\omega t)+\bar{b}_2\cos(\omega t)]. \tag{15}$$

The experimentally observable variable, $Y(t)$, is some projection of $\bar{\xi}$. The measured motion of the system will therefore have the form

$$Y(t)=e^{\alpha t}C_1\sin(\omega t+\theta)+Y_F, \tag{16}$$

for some C_1 and θ, with the observed focus at Y_F. We define $y(t)=Y(t)-Y_F$ and $\theta=0$, giving

$$y(t)=e^{\alpha t}C_1\sin(\omega t). \tag{17}$$

For $\alpha>0$, the system will spiral away from the focus with the exponential growth of $y(t)$ modulated by sinusoidal oscillations. It is natural to monitor the growing oscillations by measuring the maximum or minimum of $y(t)$. From the time derivative of (17),

$$\frac{\partial y(t)}{\partial t}=e^{\alpha t}C_2\sin(\omega t+\theta_1), \tag{18}$$

we see that the extrema of $y(t)$ are equally spaced in time by $\Delta t=\pi/\omega$. The appearance of the maxima and minima is therefore subject to the recursion relation

$$y_{i+1}=\eta y_i, \tag{19}$$

where y_i and y_{i+1} are the successive values and $\eta=-\exp(\alpha\pi/\omega)$.

The trajectory of a two-variable, linear system is shown in Fig. 3, where the horizontal axis represents the measured variable $y(t)$. Note that the extrema of $y(t)$ occur when the trajectory crosses axis M in the ξ plane. We assume that some system parameter p is used for control and that variation of this parameter causes a shift of the steady state $\bar{\xi}_F$ along line P in the ξ plane.

The steady state is stabilized by temporarily shifting its position in phase space such that the resulting trajectory (around the shifted steady state) passes through the position of the unperturbed steady state. When the system reaches this point along the trajectory, the perturbation is removed. In the targeting procedure used here, the perturbation is applied when the trajectory intersects P and is removed a half period later. The steady state is shifted to a point, indicated in Fig. 3 by a square, around which the perturbed system evolves to target the unperturbed steady state.

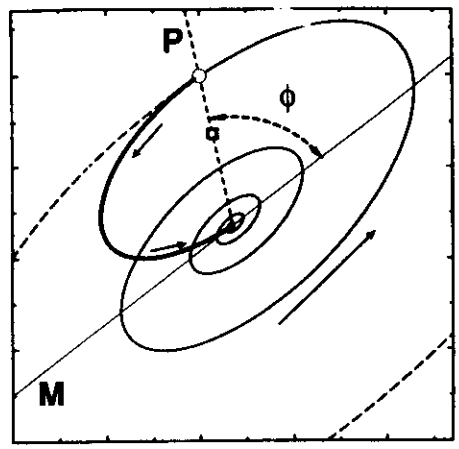

FIG. 3. The trajectory of a linear two-variable system near the stationary state. ϕ is the phase difference between the appearance of the maximum in $y(t)$ (at line M) and the direction of the steady state shift (along line P). The bold curve shows the trajectory that targets the steady state when the perturbation is applied.

As shown in Fig. 3, the perturbation must be applied at a phase ϕ following the appearance of the maximum in the measured variable $y(t)$. To synchronize the perturbation with the detection of the extremum, another variable, $z(t)$, is introduced:

$$z(t)=y(t)\left[\cos(\phi)+\frac{\alpha}{\omega}\sin(\phi)\right]-\frac{\partial y(t)}{\partial t}\frac{1}{\omega}\sin(\phi). \tag{20}$$

It follows from (17) and (20) that

$$z(t)=e^{\alpha t}C_1\sin(\omega t-\phi). \tag{21}$$

Therefore, $z(t)$ has the necessary phase shift with respect to $y(t)$. The value of ϕ can be determined by perturbing the steady state when the system is at $\bar{\xi}_F$. The trajectory will spiral out from the shifted steady state, reaching its extrema in $y(t)$ at times $(n\pi-\phi)/\omega$ after the perturbation.

Using the experimentally determined value of ϕ with Eq. (20), perturbations are applied and removed at the extrema of the new variable $z(t)$, which occur at the same phase of oscillation for all shifts of the steady state along P. The appearance of the extrema of $z(t)$ is also governed by Eq. (18) and the recursion relation (19). The effect of the perturbation Δp is given by[5]

$$z_{i+1}=\eta z_i+(1-\eta)\frac{\partial z_F}{\partial p}\Delta p. \tag{22}$$

When the perturbation is proportional to z_i,

$$\Delta p=Kz_i, \tag{23}$$

the steady state is targeted if

$$K=K_0=\frac{\eta}{(\eta-1)(\partial z_F/\partial p)}. \tag{24}$$

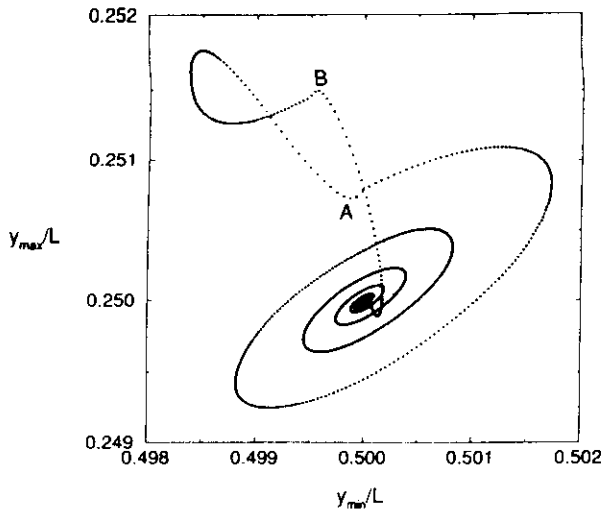

FIG. 4. Phase portrait showing a trajectory calculated from Eq. (12) at $L=17.5$ during a targeting perturbation. The horizontal axis represents the position of the local minimum in the profile relative to the width of the reaction zone. The vertical axis represents the relative position of one of the neighboring local maxima in the profile. A perturbation imposed at point A and removed at point B shifts the steady state off the unstable manifold of the stationary state. The stationary state is accurately targeted, however, because the perturbation-free period allows the system to relax along the stable manifold.

In multidimensional systems such as the Kuramoto–Sivashinsky equation, the stable manifolds may play an important role in the control algorithm. Figure 4 shows a typical trajectory arising from the application of the algorithm to Eq. (12). The system initially spirals out from the unstable focus. The perturbation was applied at point A and removed at point B. The resulting trajectory shows that although the steady state is shifted out of the plane of the unstable manifold, the focus is targeted after the perturbation is removed at point B. For accurate targeting, the system must have sufficient time to relax to the plane of the unstable focus after the perturbation is removed; otherwise, the next perturbation will be erroneously determined according to the system state at some position between point B and the steady state. The algorithm is therefore implemented with a perturbation-free period to allow the system to relax. The perturbation is applied for half the period according to Eq. (23) when the extremum in $z(t)$ is observed. It is removed for the next half period, letting the system relax along the stable manifold. The procedure is then repeated. In applying this technique to Eq. (12), the perturbations become very small (effectively approaching zero) as the system converges to the steady state. The targeting procedure therefore changes only the stability of the steady state and not its position. It should be noted that essentially the same delay technique was first used by Hunt[19] to stabilize high-periodicity orbits in a driven diode system. It has since been used in a number of studies, including controlling chaos in a laser[20] and in the Belousov–Zhabotinsky reaction.[11] Other means of targeting that do not rely on a perturbation-free period have been proposed, including a recursive proportional feedback method by Rollins, Parmananda, and Sherard[21] and a multiparameter scheme by Petrov, Peng, and Showalter.[10]

B. Stability analysis and tracking

A stability analysis subroutine is used to interrogate the steady state. The stability of the steady state under control can be changed by varying the proportionality constant K, and the response of the system to a sequence of variations yields the stability of the autonomous steady state.[5] For an arbitrary K, Eqs. (22) and (23) can be rewritten as

$$z_{i+1}=Sz_i. \tag{25}$$

The slope S, which depends linearly on the proportionality constant K, defines the stability of the system under control:

$$S=\lambda+\frac{\partial z_F^*}{\partial p}K(1-\lambda), \tag{26}$$

where $\lambda=\eta^2=\exp(2\pi\alpha/\omega)$ and

$$\frac{\partial z_F^*}{\partial p}=\frac{\partial z_F}{\partial p}\frac{\eta}{1+\eta}. \tag{27}$$

With the incorporation of a delay period to allow the system to relax between perturbations, z_F^* is the effective shift of the fixed point over the full period of oscillation for a perturbation applied over half the period. The behavior of the system under control can therefore be described in terms of the z_{i+1} vs z_i map. The ability to change the slope S of the map by an appropriate choice of K is an integral feature of the tracking algorithm.[5]

In each step of the tracking, the proportionality constant K is set to a value, K_1, that will produce a slightly unstable steady state. As the system diverges away from the steady state, points are collected for an accurate determination of the slope S_1. Before the system has evolved beyond the linear control range, K is changed to a new value, K_2, which corresponds to a mildly stable steady state. As the system converges to the steady state, values are again collected for an accurate determination of the corresponding slope S_2. The proportionality constants and corresponding slopes are then used to calculate K_0, the proportionality constant that produces a map of zero slope under control, and λ, the slope of the map of the autonomous system:[5]

$$K_0=\frac{S_2K_1-S_1K_2}{S_2-S_1} \tag{28}$$

and

$$\lambda=\frac{S_2K_1-S_1K_2}{K_1-K_2}. \tag{29}$$

The steady state becomes super-stable when the proportionality constant K_0 is used in the control algorithm. With each increment of the bifurcation parameter, the steady state is stabilized by repeating the stability analysis.

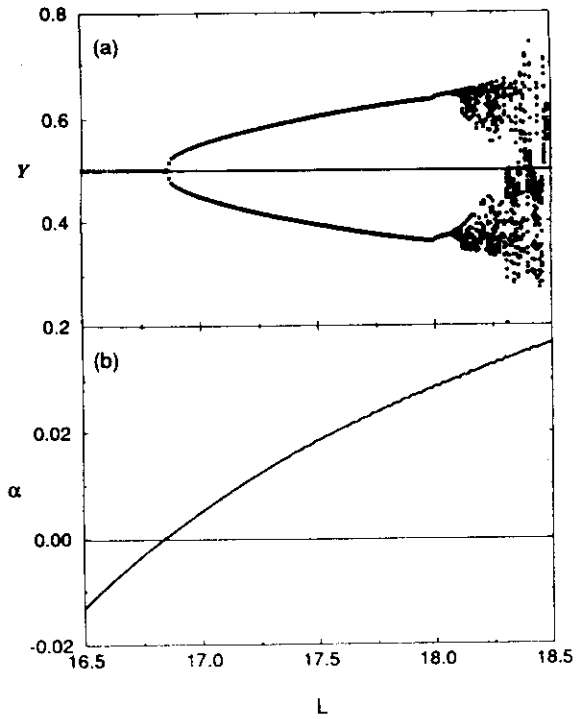

FIG. 5. (a) Bifurcation diagram of the autonomous system and the stabilized steady front calculated from the Kuramoto–Sivashinsky equation. Solid points give the relative maximum and minimum of oscillation of $Y=(y_{min}/L)$ as a function of the bifurcation parameter L. The position of the stabilized steady front is shown by the solid line. (b) Value of the real part of the complex conjugate eigenvalues as a function of L.

IV. TRACKING STEADY AND PERIODIC FRONTS IN THE KURAMOTO–SIVASHINSKY SYSTEM

The unstable states of the Kuramoto–Sivashinsky equation provide an interesting testing ground for the tracking algorithm. We first demonstrate the method by stabilizing the steady two-cell front through the period-doubling and chaotic ranges of the bifurcation parameter L. We then demonstrate the tracking of periodic orbits by stabilizing period-one oscillations through the same range. The position of the local minimum in the front profile was utilized as the "experimental" observable for the tracking procedure. It is a convenient choice because the steady solution is symmetrical for all L, with the minimum exactly at the center of the reaction zone.

The bifurcation diagram of the autonomous system is shown in Fig. 5(a). The solution is stable for $L<16.8$, with the position of the minimum in the front profile, $Y=y_{min}/L$, remaining at the center of the reaction zone [cf. Fig. 2(a)]. A Hopf bifurcation occurs at $L=16.85$, and the front begins to oscillate. The solid circles show the maximum and minimum of the oscillations [cf. Fig. 2(b)]. As the width is increased, a symmetry-breaking bifurcation occurs at $L=18.0$ and two mirror-image, period-one solutions appear, each of which exhibit oscillations centered above or below the middle of the reaction zone. The symmetry-breaking bifurcation is necessary for this symmetrical system to develop a series of period-doubling bifurcations leading to a chaotic attractor.[22] (For clarity, only one of the solutions is shown in the bifurcation diagram.) As the width is increased, the oscillations become more complex through the period-doubling cascade to eventually become chaotic at $L=18.1$ [cf. Fig. 2(c)]. At $L=18.33$, the oscillatory chaos disappears and more complex behavior is exhibited, where minima in the front profile randomly appear only to coalesce with other minima and the system boundaries.

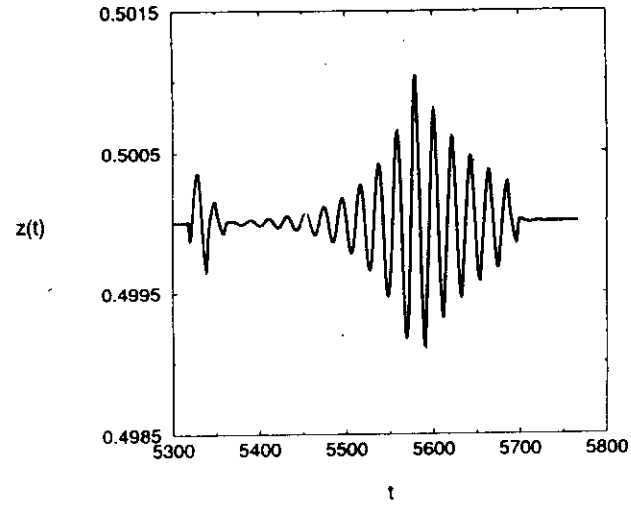

FIG. 6. Time series showing one step of the tracking procedure at $L=17.5$. A perturbation is first applied to determine ϕ. The following series of oscillations with increasing and decreasing amplitude is used to determine the stability of the steady state (see text).

The steady flame front is stabilized by varying the boundary conditions to simulate perturbations to the fuel supply. The no-flux boundary condition, $\partial\Psi/\partial y=0$ in Eq. (12), was varied according to z_i in Eq. (23) at one boundary. This control parameter corresponds to an experimental setting in which there are minute, asymmetric variations in the fuel supply. Since the system is symmetrical at the steady state, an asymmetric perturbation is necessary to affect the steady state position.

Figure 6 shows a time series during one step of the tracking algorithm as the width of the reaction zone was changed from $L=17.4$ to 17.5. A perturbation was first applied at $t=5318$ to calculate the phase ϕ of the projected oscillations. This is used in Eq. (20) to transform to the variable $z(t)$. The proportionality constant was then set to the value $K_1=-24.2$ at $t=5360$ to produce a slightly unstable state. The resulting oscillations gradually increase in amplitude, as shown in Fig. 6. At $t=5580$, the proportionality constant is changed to a new value, $K_2=178.9$, which corresponds to a mildly stable state. Figure 6 shows these oscillations gradually decreasing in amplitude. The local slopes S_1 and S_2 corresponding to K_1 and K_2 are determined from the z_{i+1} vs z_i return maps. Figure 7 shows the maps for the diverging and converging system. The values of K_1, K_2, S_1, and S_2 allow the determination of K_0 from Eq. (28). The steady state is then targeted using the updated K_0, shown in Fig. 6 at $t=5685$.

Due to the symmetry of the two-cell front (and the choice of the local minimum in the profile as the monitored

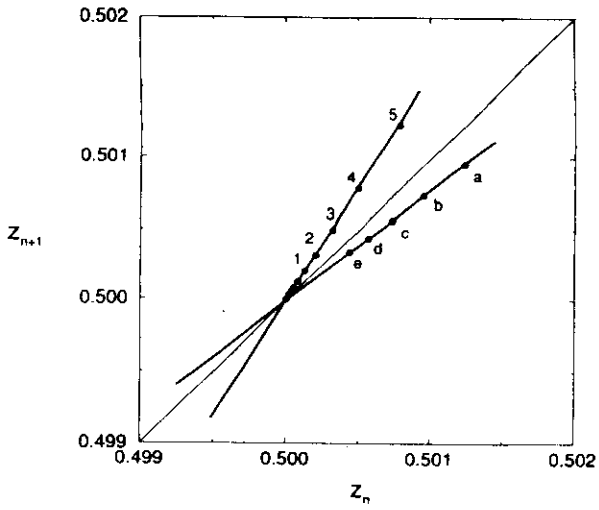

FIG. 7. Return maps for the tracking step in Fig. 6. Two different values of K cause the system to diverge away from the stationary state (1,2,3,...) and converge back to that state ($a,b,c,...$). The proportionality constant was first set to $K_1=-24.2$ and then to $K_2=178.9$ to generate the divergent and convergent behavior. The corresponding values of S_1 and S_2 in Eqs. (28) and (29) yield the values $K_0=373.7$ and $\lambda=1.48$.

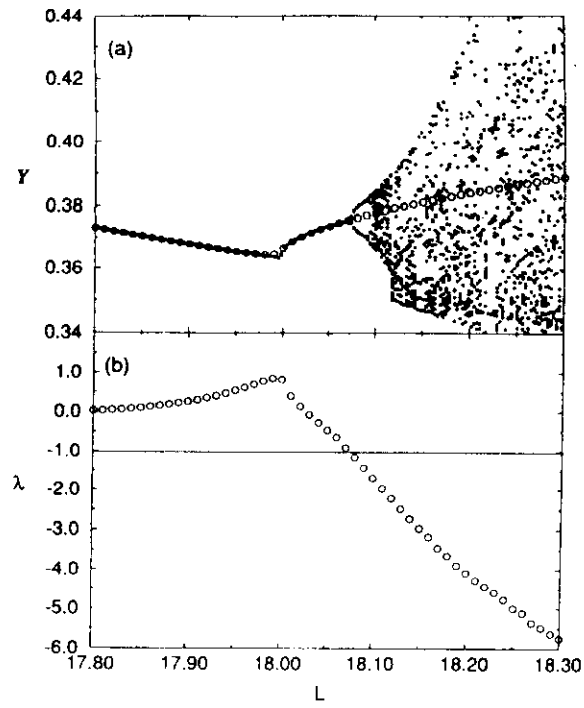

FIG. 8. Stabilization and tracking of period-1 oscillations. (a) Bifurcation diagram calculated from Eq. (12), where the solid points represent the oscillation minimum of the local minimum in the front profile, $Y=(y_{min}/L)_{min}$. The open circles show the locus of the tracked period-1 orbit. (b) Value of the period-1 Floquet multiplier as a function of L.

variable), the position of the steady state remains at $Y=y_{min}/L=0.5$. The steady state position therefore does not require reevaluation by the tracking procedure when the bifurcation parameter is changed. The solid line in Fig. 5(a) shows the stabilized front at $Y=0.5$ following the Hopf bifurcation at $L=16.85$. The steady-state stability of the autonomous system is also determined by the tracking algorithm. Figure 5(b) shows the real part of the complex conjugate eigenvalues of the focus plotted as a function of the reaction zone width. Both stable and unstable steady states can be examined, since the appropriate choice of K causes the system to either converge to or diverge from the steady state, thereby allowing the eigenvalues to be determined from Eq. (29).

The tracking algorithm can also be used to stabilize periodic oscillations of the front. For periodic orbits, the algorithm relies on the saddle character of the corresponding fixed points in the Poincaré section. As previously reported, periodic orbits with only one unstable manifold and highly attractive stable manifolds can be readily stabilized and tracked.[5] The method is analogous to that for stabilizing steady states except no phase correction is necessary. The oscillatory behavior of Eq. (12) is described according to a 1-D map by plotting the current minimum of oscillation with respect to the previous minimum. The period-1 orbit is then stabilized and tracked by targeting the fixed point in the map. As in earlier applications,[5,9-11] perturbations proportional to the deviation from the fixed point are applied. To allow time for the system to relax to the unstable manifold, the perturbations are applied for only half the oscillatory cycle. The tracking algorithm maintains the local stability of the periodic orbit by determining the proportionality constant K_0 and the Floquet multiplier λ for each new value of the bifurcation parameter L. The amplitude of the period-1 orbit changes as the value of L is increased, and a corresponding shift of the fixed point occurs in the map. The position of the fixed point must therefore be redetermined (according to the method described in Ref. 5) for each new value of L.

Figure 8(a) shows an enlargement of Fig. 5 near the first period-doubling bifurcation at $L=18.07$. The locus of the period-1 orbit determined by the tracking algorithm is shown by the open circles. Figure 8(b) shows the Floquet multiplier λ of the period-1 orbit as a function of L. The tracking algorithm determines the Floquet multiplier of the stable as well as the unstable orbits, since, like the stability of the steady state, the stability of the orbit can be varied by varying the value of K. A symmetry breaking bifurcation, where $\lambda=1.0$, occurs at $L=18.0$, and the algorithm switches to one of the new stable solutions. At $L=18.07$, the period-doubling bifurcation takes place with $\lambda=-1.0$. The unstable period-1 orbit is then tracked through the period-doubling cascade and into the chaotic regime.

V. TRACKING STEADY FRONTS IN THE PDE SYSTEM

Equations (1) and (2) provide a more realistic description of premixed flames than the Kuramoto–Sivashinsky equation. To simulate 2-D flame fronts undergoing thermodiffusive instabilities, parameter values satisfying Eq. (11) were used in the numerical integration of Eqs. (8) and (9). The parameter values $\mathcal{L}=0.8$, $\epsilon=0.15$, and $N=20$ were chosen to reflect actual values in an experimental system.[15]

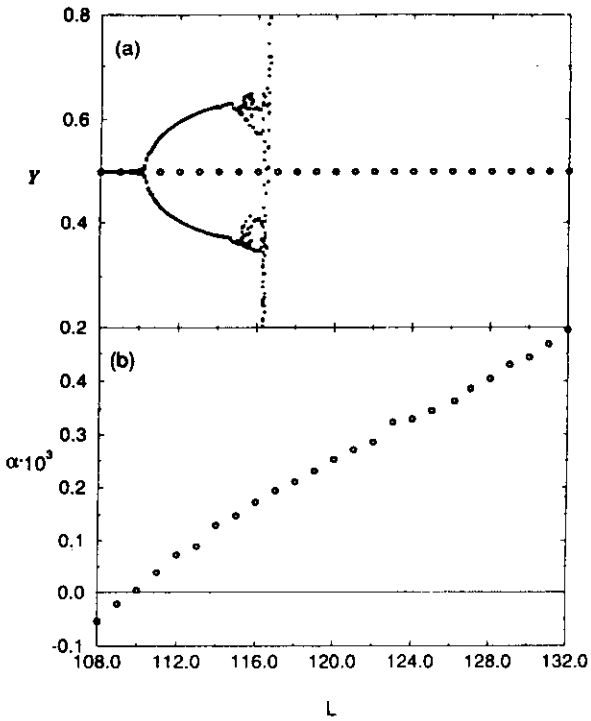

FIG. 9. Stabilization and tracking of the steady front calculated from Eqs. (8) and (9). (a) Bifurcation diagram of the front oscillations, where the solid points show the oscillation extrema of the local minimum in the front profile, $Y=(y_{min}/L)$. The stabilized stationary state is shown by the open circles. (b) The real part of the complex conjugate eigenvalues as a function of L. Conditions are the same as in Fig. 1.

The integration yields a two-cell front over a reaction zone width ranging from $L=106$ to 116.2. As with the Kuramoto–Sivashinsky system, the behavior was characterized by monitoring the local minimum of the front contour, $Y=y_{min}/L$. The bifurcation diagram of the autonomous system is shown in Fig. 9(a) by points representing the extrema in Y as a function of L. The behavior is qualitatively the same as that exhibited by the Kuramoto–Sivashinsky equation. The two-cell front loses stability through a Hopf bifurcation at $L=110.2$, which is followed by a symmetry breaking bifurcation at $L=114.6$. At $L=114.9$, a period-doubling cascade is initiated that gives rise to a strange attractor at $L=115.2$. This attractor coexists with another, mirror-image attractor that arises from the symmetry-breaking bifurcation. At $L=116.2$, both of these attractors are destroyed and the oscillatory behavior is replaced by an attractor with randomly appearing and disappearing minima in the front profile. The dynamical behavior governed by the new attractor is clearly more complex than the chaos arising from the period-doubling cascade.

The application of the tracking algorithm to stabilize the steady two-cell front is shown in Fig. 9. The minimum in the front contour at $Y=0.5$ is shown in Fig. 9(a) by the open circles. The steady front was stabilized from where it loses stability at the Hopf bifurcation to a value of L far beyond where the low-dimensional chaos gives way to the complex nonoscillatory behavior. The real part of the complex conjugate eigenvalues for the focus steady state is shown by the circles in Fig. 9(b); the line at $\alpha=0.0$ separates the regions of stable and unstable behavior. A control parameter analogous to that used for the Kuramoto–Sivashinsky equation was chosen to stabilize the steady front. The fuel flux at one of the boundaries was varied in proportion to z_i in Eq. (23) by varying the no-flux boundary condition around zero at one boundary grid point upstream from the front. The algorithm was initiated at $L=108.0$, where the steady state is still stable, and continuously applied to $L=132.0$.

Because the perturbations applied by the tracking algorithm become very small after the steady state is targeted, the position of the steady state is unaffected even though its stability is altered. The presence of noise and experimental errors, however, may affect both the position and stability of the steady state. During control, these fluctuations are multiplied by a factor of $\exp(\alpha T_p)$, where T_p is the period of oscillation, and can cause the algorithm to fail when αT_p is large.[10] The stabilization of the two-cell front eventually fails as L is increased, since, as shown in Fig. 9(b), the state becomes highly unstable at large L.

VI. CONCLUSION

Stabilization and tracking methods represent powerful tools for investigating the bifurcation structures of dynamical systems. Studies of dynamical systems typically rely on time series analysis, with the character of the bifurcations inferred from the qualitative changes in behavior as a system constraint is systematically varied. Information about the position and stability of unstable states has been accessible only from the application of continuation methods[23] to model descriptions. This information is necessarily dependent on the accuracy of the model. Tracking methods, on the other hand, provide information that is primary in nature and not dependent on a particular model interpretation. These methods therefore provide an expansion of the repertoire of techniques for the *experimental* characterization of dynamical systems. The development of model descriptions is thereby enhanced by the larger experimental data base for comparisons between experiment and theory.

Several different schemes have been proposed for tracking unstable states, most of which have stabilization routines based on reductions of the OGY method.[12,13] We have relied on the map-based stabilization algorithm,[9–11] since a linear stability analysis subroutine can be readily incorporated into the tracking procedure.[5] In the application presented here, modifications incorporating a phase shift allow the algorithm to be applied to focus-type stationary states. Methods based on targeting stable manifolds in phase space could also be adapted to this type of tracking scheme.

The tracking of steady and oscillatory flame fronts considered in this study points to an obvious application of such algorithms: the stabilization of desired dynamical behavior under extreme or varying conditions. Extending the regime of stable burning, for example, could serve to enhance the efficiency of combustion processes. In order to facilitate our study of stabilization and tracking, we have considered only the simplest model systems. The model independent nature

of the method, however, suggests that more complicated flame systems, such as those subject to hydrodynamic instabilities, might also be amenable to stabilization and tracking.

Although full knowledge of the system dynamics was available in this study, the control and tracking procedure utilized only a single "experimental" observable, the position of the local minimum in the front profile. The Kuramoto–Sivashinsky equation, as well as the complete reaction–diffusion system, served as test systems for the tracking algorithm, with unstable steady states and periodic orbits stabilized and tracked through period-doubling cascades, simple period-doubling chaos, and more complex spatiotemporal chaos. Since the algorithm stabilizes states that are representative of the autonomous system, it provides a model-independent, path-following method for the investigation of experimental dynamical behavior. The stabilization of steady and oscillatory flame fronts in premixed flames is only one potential application of the algorithm; other applications should be possible in biological and chemical spatiotemporal systems.

ACKNOWLEDGMENTS

K. S. is grateful to Professor Grégoire Nicolis for his hospitality at the Service de Chimie Physique, Université Libre de Bruxelles where this manuscript was prepared. We thank the National Science Foundation (Grant No. CHE-9222616), WV-EPSCoR (Grant No. OSR-9255224), and the National Research Center For Coal and Energy for supporting this research. Acknowledgment is made to the donors of The Petroleum Research Fund, administered by the American Chemical Society, for partial support of this research.

[1] G. H. Markstein, J. Aeronaut. Sci. **3**, 18 (1951).
[2] A. G. Merzhanov and B. I. Khaikin, Prog. Energy Combust. Sci. **14**, 1 (1988).
[3] J. F. Clarke, Prog. Energy Combust. Sci. **15**, 241 (1989).
[4] G. I. Sivashinsky, Annu. Rev. Fluid Mech. **15**, 179 (1983).
[5] V. Petrov, M. F. Crowley, and K. Showalter, Phys. Rev. Lett. **72**, 2955 (1994).
[6] Z. Gills, C. Iwata, R. Roy, I. B. Schwartz, and I. Triandaf, Phys. Rev. Lett. **69**, 3169 (1992).
[7] S. Bielawski, M. Bouazaoui, D. Derozeir, and P. Glorieux, Phys. Rev. A **47**, 3276 (1994).
[8] A. Hjelmfelt and J. Ross, J. Phys. Chem. **94**, 1176 (1994).
[9] B. Peng, V. Petrov, and K. Showalter, J. Phys. Chem. **95**, 4957 (1991).
[10] V. Petrov, B. Peng, and K. Showalter, J. Chem. Phys. **96**, 7506 (1992).
[11] V. Petrov, V. Gáspár, J. Masere, and K. Showalter, Nature **361**, 240 (1993).
[12] E. Ott, C. Grebogi, and J. A. Yorke, Phys. Rev. Lett. **64**, 1196 (1990).
[13] T. Shinbrot, C. Grebogi, E. Ott, and J. A. Yorke, Nature **363**, 411 (1993).
[14] W. H. Press, B. P. Flannery, S. A. Teukolsky, and W. T. Vetterling, *Numerical Recipes* (Cambridge U. P., New York, 1986), p. 660.
[15] G. I. Sivashinsky, Combust. Sci. Technol. **15**, 137 (1977).
[16] G. I. Sivashinsky, Acta. Astronaut. **4**, 1177 (1977).
[17] Y. Kuramoto, Prog. Theor. Phys. **63**, 1885 (1980).
[18] J. M. Hyman, B. Nicolaenko, and S. Zaleski, Physica D **23**, 265 (1986).
[19] E. R. Hunt, Phys. Rev. Lett. **67**, 1953 (1991).
[20] R. Roy, T. W. Murphy, T. D. Maier, Z. Gills, and E. R. Hunt, Phys. Rev. Lett. **68**, 1259 (1992).
[21] R. W. Rollins, P. Parmananda, and P. Sherard, Phys. Rev. E **47**, R780 (1993).
[22] K. Kaneko, Prog. Theor. Phys. **69**, 1427 (1983).
[23] E. J. Doedel, Congress Num. **30**, 265 (1981); E. J. Doedel and J. P. Kernevez, *AUTO: Software for Continuation and Bifurcation Problems in Ordinary Differential Equations* (Applied Mathematics, California Institute of Technology, Pasadena, 1986).

Stabilizing and characterizing unstable states in high-dimensional systems from time series

Valery Petrov,[1] Eugene Mihaliuk,[1] Stephen K. Scott,[2] and Kenneth Showalter[1,*]
[1]*Department of Chemistry, West Virginia University, Morgantown, West Virginia 26506-6045*
[2]*School of Chemistry, University of Leeds, Leeds LS2 9JT, United Kingdom*
(Received 13 December 1994)

An algorithm for stabilizing, characterizing, and tracking unstable steady states and periodic orbits in multidimensional dynamical systems is presented. The algorithm requires only one variable to be monitored and only one parameter to be perturbed for the stabilization of states with many unstable degrees of freedom and possibly an infinite number of stable degrees of freedom. The system is identified in terms of a linear recursive model with coefficients determined from successive readings of the variable subject to small random perturbations of the parameter. These coefficients determine the appropriate perturbations for control and also provide a direct route to the eigenvalues of the autonomous system. Spatially extended systems with an infinite number of degrees of freedom can be reduced to n effective dimensions that involve all the unstable manifolds and the weakly attracting stable manifolds. The remaining highly attracting manifolds are treated as one lumped eigenvector with an eigenvalue close to zero. The algorithm also allows the effective dimension of the state to be determined.

PACS number(s): 05.45.+b, 82.40.Py, 82.40.Bj

I. INTRODUCTION

Major strides have been made over the past few years in controlling chaos in low-dimensional systems [1]. Unstable periodic orbits have been stabilized in magnetoelastic strips [2], electronic circuits [3,4], laser systems [5,6], and chemical reactions [7–9], and recent reports of stabilizing periodic rhythms in heart tissue [10] and inducing periodic and chaotic behavior in hippocampal brain tissue [11] have stimulated widespread interest. It is clear that new developments in controlling dynamical systems offer opportunities for potentially important practical applications.

Several theoretical approaches have been advanced for stabilizing periodic orbits in chaotic systems. The feedback method proposed by Ott, Grebogi, and Yorke (OGY) [1,12] and the various modifications of this method have been the most popular. The OGY method is appealing because it is easily understood in terms of the system state in phase space. Stabilizing an unstable orbit simply involves perturbing the system such that the stable manifold of the orbit is targeted at each return. Thus, the positions of the system state and fixed point are known (in a suitable Poincaré section), and the effect of the perturbation is explicitly defined. Other control methods, including the continuous feedback algorithm of Pyragas [13,14], are described and compared to the OGY method by Alsing, Gavrielides, and Kovanis [15].

In systems that can be described by effectively one-dimensional (1D) maps, the OGY method can be reduced to an algorithm that directly targets the fixed point rather than the stable manifold [16,17]. The reduced algorithm is attractive for experimental applications because it requires minimal computational effort [3,5,7]. It can also be easily modified to permit tracking unstable steady and periodic states through bifurcation sequences [18,19]. Unstable periodic orbits [4,20] and steady states [21–23] have also been tracked with techniques that minimize fluctuations around the targeted fixed point.

It is known that the simple map-based approach may fail, even when a system is low dimensional and governed by a 1D map [17]. This arises when the fixed point is shifted away from the unstable manifold of the original attractor as the parameter is perturbed. In such cases, the perturbed system can no longer be described in terms of the shifted 1D map, which causes the method to fail. Rollins, Parmananda, and Sherard [24] have recently proposed a recursive algorithm that corrects for this effect. They added a linear recursive term to the map-based algorithm, following an earlier suggestion by Dressler and Nitsche [25] for modifying the OGY method when time-delay coordinates are used. This yields a one-variable, one-parameter method that allows stabilization in the otherwise pathological case when the fixed point is shifted away from the original unstable manifold [8].

Stabilizing and tracking states with more than one unstable direction remains an important challenge. Such states are common in spatially extended systems, and techniques beyond those developed for low-dimensional systems will be required for controlling spatiotemporal chaos. Simple techniques may be successful in certain spatiotemporal systems, such as when the behavior is highly spatially correlated [19]. Spatiotemporal chaos has also been controlled in a convectively unstable system, where the stabilized behavior is swept into the surrounding regions [26]. Proportional feedback has been used to stabilize periodic behavior in a coupled map lattice by multiple pinnings at locally stabilized sites, where the density of sites is increased until ordered behavior is exhibited [27]. Auerbach *et al.* [28] have proposed a

*Author to whom correspondence should be addressed.

generalization of the OGY approach, applicable to systems with one unstable and many stable degrees of freedom. Romerias *et al.* [29] have developed an approach for stabilizing states with multiple unstable directions and have applied this to a kicked double rotor model. It was necessary, however, to monitor all of the system variables for control.

In this paper, we present a general method for stabilizing and characterizing states with many unstable degrees of freedom and possibly an infinite number of stable degrees of freedom. This generalization provides an explicit connection between the OGY and related phase space approaches and the linear control routines of classical single-input single-output (SISO) systems [30]. The stabilization of high-dimensional unstable steady or periodic states requires only one system variable to be monitored and only one system parameter to be perturbed. The essential features of the approach are illustrated in Sec. II by considering a simple two-variable system, beginning with the case in which the system variables can be monitored directly and then generalizing this to a single experimental observable. A generalization of the approach to an n-dimensional system is described in Sec. III. The algorithm is applied in Sec. IV to stabilize and characterize an unstable four-cell flame front of the Kuramoto-Sivashinsky equation, which is found to have six unstable degrees of freedom. The method is also applied to stabilize and track a periodic orbit with two unstable directions. The advantages and limitations of the approach along with potential applications are described in Sec. V.

II. TWO-VARIABLE SYSTEM ILLUSTRATION

A geometric description of the general stabilization method can be developed by considering its application to a simple two-variable system. The system behavior around the unstable steady state is described by two linearized equations. Discrete dynamics is assumed, reflecting an experimental setting in which the system is sampled and perturbed at a fixed rate. Oscillatory behavior in the vicinity of an unstable periodic orbit can be reduced to linear discrete-time equations by using a suitable Poincaré section.

For illustration purposes, we imagine that ξ_1 and ξ_2, the coordinates along the system eigenvectors, are monitored at regular time intervals to give the set of data pairs $(\xi_{1,i},\xi_{2,i})$. If the ith point lies away from the fixed point $(\xi_{1,F},\xi_{2,F})$ and if the characteristic exponents describing the motion along the eigenvectors are λ_1 and λ_2, respectively, then the discrete-time equations of motion for the $i+1$ point are

$$\begin{aligned}\xi_{1,i+1}-\xi_{1,F}&=\lambda_1(\xi_{1,i}-\xi_{1,F}) ,\\ \xi_{2,i+1}-\xi_{2,F}&=\lambda_2(\xi_{2,i}-\xi_{2,F}) .\end{aligned} \tag{1}$$

For convenience, we assume that the fixed point lies at the origin: $(\xi_{1,F},\xi_{2,F})=(0,0)$. If, however, we also impose a small perturbation on some parameter p, the position of the fixed point is shifted along some line in phase space by an amount proportional to the perturbation. Denoting this perturbation as p_{i+1}, the evolution equations now become

$$\begin{aligned}\xi_{1,i+1}&=\lambda_1\xi_{1,i}+(1-\lambda_1)\alpha_1 p_{i+1} ,\\ \xi_{2,i+1}&=\lambda_2\xi_{2,i}+(1-\lambda_2)\alpha_2 p_{i+1} ,\end{aligned} \tag{2}$$

where the coefficients α_1 and α_2 are the projections of the shift vector $\partial\xi_F/\partial p$ determining the change in the fixed point position along the corresponding eigenvectors with change in the parameter p.

If a second perturbation p_{i+2} is made at the next step, the second iteration will be given by

$$\begin{aligned}\xi_{1,i+2}&=\lambda_1^2\xi_{1,i}+(1-\lambda_1)\alpha_1(\lambda_1 p_{i+1}+p_{i+2}) ,\\ \xi_{2,i+2}&=\lambda_2^2\xi_{2,i}+(1-\lambda_2)\alpha_2(\lambda_2 p_{i+1}+p_{i+2}) .\end{aligned} \tag{3}$$

Note that the eigenvalues are assumed to be independent of the parameter perturbation, at least to leading order. From Eq. (3) it follows that $\xi_{1,i+2}$ and $\xi_{2,i+2}$ can be set equal to zero by an appropriate choice of the perturbations p_{i+1} and p_{i+2}, which are found as a solution of the linear system provided $\lambda_1\neq\lambda_2$ and $\alpha_i\neq 0$. The requirement of the system eigenvalues to be nonequal and the parameter perturbation to displace the system along all of the unstable manifolds are the main conditions for achieving stabilization of multivariable systems using a single parameter.

Figure 1 shows an application with $\lambda_1=1.5$ and $\lambda_2=3$, where the system has evolved away from the unstable fixed point at the origin to the point marked 0. In the first perturbation, the fixed point is moved along the shift vector $\partial\xi_F/\partial p$ to $\xi_F^1=(\xi_{1,F},\xi_{2,F})^1$. The system state evolves relative to the shifted fixed point according to the multipliers to the point marked 1. In the second perturbation, the fixed point is moved again along the shift vec-

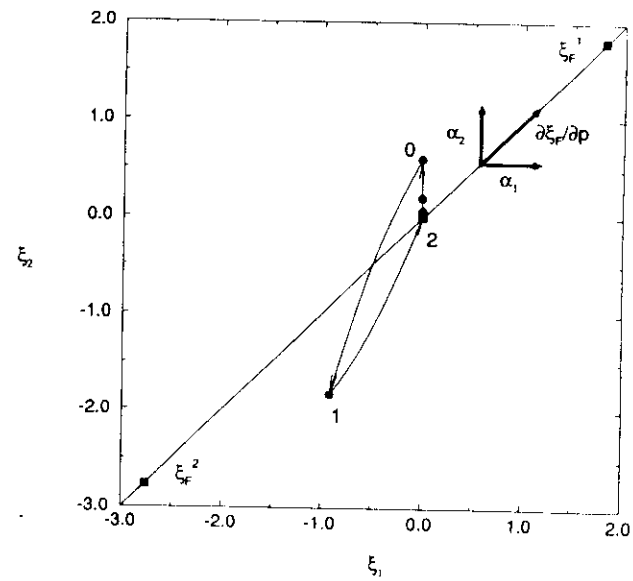

FIG. 1. Geometrical description of control method. Application to a two-variable system with a fixed point characterized by $\lambda_1=1.5$ and $\lambda_2=3$. Two successive perturbations cause the system to evolve from point 0 to point 2, corresponding to the fixed point of the unperturbed system.

tor to $\xi_F^2=(\xi_{1,F},\xi_{2,F})^2$. The system now evolves relative to this fixed point position to the point marked 2, which corresponds to the targeted fixed point of the unperturbed system.

This example provides a graphical description of the targeting procedure; however, it differs from the operational procedure in that the sequence of n controlling perturbations must be determined in advance. In real-time applications of the algorithm, the value of the controlling perturbation is updated at each step. For the two-variable example, the $i+1$ perturbation is

$$p_{i+1}=k_1\xi_{1,i}+k_2\xi_{2,i} , \tag{4}$$

where the coefficients k_1 and k_2 are chosen to ensure that the fixed point is targeted on the second iteration. There are several possibilities for finding the appropriate k_1 and k_2 when the system coordinates or all independent system variables are known. The approach originally suggested by OGY targets the stable manifold of a state with one unstable direction [12]. If the fixed point has two unstable manifolds, it can still be targeted using Eq. (4) with two successive perturbations [29]. In the absence of noise, control equations (3) and (4) each produce the same sequence of two perturbations for targeting the fixed point.

In experimental settings, we commonly do not have access to the actual system variables, nor can we monitor n independent observable variables. Time-delay embedding techniques can be used to reconstruct the system state around a periodic orbit [12] provided that a correction for the shift of the Poincaré section is carried out [25,28,29]. Here we present a general approach for reconstructing the system state from the readings of one observable variable in the presence of perturbations. The approach is applicable to system dynamics on a Poincaré section or around a steady state.

In general, we monitor some observable x that is a linear combination of the system variables. For our two-variable illustration, we have

$$x_i=t_1\xi_{1,i}+t_2\xi_{2,i} . \tag{5}$$

The choice of variable x is largely unrestricted; however, the expected unstable behavior must be observable by monitoring x.

We will show that the system state vectors ξ, scaled by projection coefficients t_i, can be reconstructed from successive readings of x and p. We rewrite Eqs. (2) for $i-1$ and then sum the first multiplied by $\lambda_2 t_1$ with the second multiplied by $\lambda_1 t_2$, and with Eq. (5) for $i-1$ obtain

$$\lambda_1\lambda_2 x_{i-1}+[\lambda_2(1-\lambda_1)\alpha_1 t_1+\lambda_1(1-\lambda_2)\alpha_2 t_2]p_i = \lambda_2 t_1\xi_{1,i}+\lambda_1 t_2\xi_{2,i} . \tag{6}$$

The system state $(t_1\xi_{i,1},t_2\xi_{i,2})$ can therefore be found as a solution of Eqs. (5) and (6) from the x_i, x_{i-1}, and p_i, provided that $\lambda_1\neq\lambda_2$. The control equation (4) can then be written as

$$p_{i+1}=q_2 x_i+q_1 x_{i-1}+r_1 p_i , \tag{7}$$

where coefficients q_1, q_2, and r_1 can be expressed through the system parameters. It follows from Eq. (6) that the term involving x_{i-1} disappears from the control equation in the case when one of the manifolds is strongly attracting (for which $\lambda_2\approx 0$). This corresponds to the recursive feedback algorithm of Rollins, Parmananda, and Sherard [24] for the control of highly dissipative systems. It also follows from Eq. (6) that when the perturbation does not significantly shift the fixed point off the unstable manifold ($\lambda_2\approx 0$ and $\alpha_2\approx 0$) the simple map-based algorithm [16,17] is recovered.

We show in Sec. III that n successive readings of the observable x and $n-1$ values of the previous perturbations are required to control an n-dimensional system. We also show how the coefficients q_1, q_2, and r_1 of the control equation can be found, along with other system unknowns, from the time series of the experimental observable.

System identification and control

The control algorithm requires that the dynamical system be continuously *interrogated* by imposing random perturbations on a suitable parameter p at regular sampling intervals. The time series obtained by recording some observable x then consists of a set of data pairs:

$$(x_1,p_1),(x_2,p_2),(x_3,p_3),\ldots,(x_i,p_i) . \tag{8}$$

For a system with two independent variables, we need to record at least seven data pairs (i.e., $3n+1$) to allow identification of the system. Control can then begin with the parameter perturbation p_8.

The time series can be fitted to a recursive SISO model [30] of the form

$$x_{i+1}=a_2 x_i+a_1 x_{i-1}+a_0+b_2 p_{i+1}+b_1 p_i . \tag{9}$$

This form is also known as an autoregressive with auxiliary input (ARX) equation [31]. The number of fitting coefficients a and b and their relation to the system parameters is discussed in Sec. III. For the two-dimensional system, $n=2$ and there are five unknowns: a_0–a_2, b_1, and b_2. Applying this approach to obtain the data pairs in (8) produces a set of five equations, which we can write explicitly as

$$\begin{aligned} x_3&=a_2 x_2+a_1 x_1+a_0+b_2 p_3+b_1 p_2 , \\ &\vdots \\ x_7&=a_2 x_6+a_1 x_5+a_0+b_2 p_7+b_1 p_6 , \end{aligned} \tag{10}$$

where the coefficient a_0 is related to the fixed point x_F by

$$a_0=(1-a_2-a_1)x_F . \tag{11}$$

We note that $a_0=0$ if $x_F=0$, which we assume in the following treatment. (Alternatively, the optimal values of the coefficients could be determined more precisely from a larger data set using singular value decomposition, but here we proceed from this minimum basis set.)

The eigenvalues λ_1 and λ_2 governing the "autonomous" system, i.e., the system in the absence of perturbations, can be determined from the a_i coefficients.

Motion along the ith eigenvector occurs with $x_n \propto \lambda_i^n$, and substituting the corresponding terms into (9) yields the characteristic equation for the system eigenvalues:

$$-\lambda^2+a_2\lambda+a_1=0 \ . \tag{12}$$

The eigenvalues of the "closed-loop" system under control can be obtained by deriving the recursive model in a form that does not depend on the perturbations. We obtain the perturbation-independent equation by combining Eqs. (7) and (9) to express p_{i+1}:

$$p_{i+1}=\frac{r_1x_{i+1}+(b_1q_2-r_1a_2)x_i+(b_1q_1-r_1a_1)x_{i-1}}{r_1b_2+b_1} \ . \tag{13}$$

Equation (13) for p_i and p_{i+1} can be substituted into Eq. (9), allowing x_{i+1} to be expressed as a linear combination of x_i, x_{i-1}, and x_{i-2}:

$$x_{i+1}=l_3x_i+l_2x_{i-1}+l_1x_{i-2} \ , \tag{14}$$

where

$$l_3=r_1+a_2+b_2q_2, \quad l_2=a_1-r_1a_2+b_1q_2+b_2q_1 \ , \quad l_1=b_1q_1-a_1r_1 \ . \tag{15}$$

The controlled system is described by Eq. (14) and is characterized by a total of three eigenvalues, λ_1,λ_2, and λ_3, which can be found as roots of the polynomial

$$-\lambda^3+l_3\lambda^2+l_2\lambda+l_1=0 \ . \tag{16}$$

We achieve stabilization using the pole placement technique, i.e., by requiring these eigenvalues to adopt the target values λ_1^*,λ_2^*, and λ_3^*. The roots of Eq. (16) will have the appropriate values of λ_i^* when

$$l_1=\lambda_1^*\lambda_2^*\lambda_3^*, \quad l_2=-(\lambda_1^*\lambda_2^*+\lambda_2^*\lambda_3^*+\lambda_3^*\lambda_1^*) \ , \quad l_3=\lambda_1^*+\lambda_2^*+\lambda_3^* \ . \tag{17}$$

There is some freedom in selecting the target values. In general, we require $|\lambda_i^*|<1$ so the system converges toward the fixed point: the smaller the magnitude of the target eigenvalues, the faster the convergence will be. When all of the eigenvalues of the system under control are chosen to be zero (so-called "deadbeat" control) the system should converge to the steady state after n iterations. This, however, may involve the imposition of larger perturbations at the early stages of control. One approach is to leave the stable eigenvalues unchanged. This control results in targeting the corresponding stable manifolds rather than the fixed point and reduces the magnitude of the control perturbations. It is important to note that setting the eigenvalues close to unity is dangerous, since even small errors in the system identification can then make the system unstable. Also, if the system is high dimensional, errors in the system parameters that are inevitably carried over from the identification stage may become large. Selecting the optimal control law in the presence of system parameter errors is the subject of the H_∞ control approach [32].

The various coefficients a_0–a_2, b_1,b_2, and l_1–l_3 are now used to calculate the required perturbation to be imposed at the next time step:

$$p_8=q_2x_7+q_1x_6+q_0+r_1p_7 \ . \tag{18}$$

Here q_1, q_2, and r_1 are given by the solutions of Eqs. (15) and (17) and q_0 is assumed to be zero (which is equivalent to $x_F=0$). This perturbation is applied at the seventh sampling time. The process is then repeated, with the appropriate perturbation p_9 being calculated from x_8, x_7, and p_8.

III. GENERALIZATION TO AN n-VARIABLE SYSTEM

The control algorithm can be generalized to apply to a system of dimensionality n. The coefficients a_0–a_n and b_1–b_n are determined by fitting the recursive SISO model to at least $3n+1$ data pairs collected from the interrogated system (i.e., the system subjected to random perturbations at each sampling time) and the target values selected for the eigenvalues of the controlled system.

If a sequence of n perturbations p_2 to p_{n+1} is applied to an n-dimensional system, the following equations can be written for n consecutive iterations of the state vector ξ (i.e., the coordinates along the system eigenvectors):

$$\begin{aligned}
&\xi_1=\xi_1 \ , \\
&\xi_2=\hat{\lambda}\xi_1+(\hat{I}-\hat{\lambda})p_2\alpha \ , \\
&\xi_3=\hat{\lambda}^2\xi_1+(\hat{I}-\hat{\lambda})(p_2\hat{\lambda}+p_3)\alpha \ , \\
&\vdots \\
&\xi_{n+1}=\hat{\lambda}^n\xi_1+(\hat{I}-\hat{\lambda})(p_2\hat{\lambda}^{n-1}+\cdots+p_n\hat{\lambda}+p_{n+1})\alpha \ ,
\end{aligned} \tag{19}$$

where

$$\hat{\lambda}=\begin{bmatrix}\lambda_1 & 0 & 0\\ 0 & \ddots & 0\\ 0 & 0 & \lambda_n\end{bmatrix}, \quad \hat{I}=\begin{bmatrix}1 & 0 & 0\\ 0 & \ddots & 0\\ 0 & 0 & 1\end{bmatrix}, \quad \alpha=\frac{\partial\xi_F}{\partial p} \ . \tag{20}$$

In the general case, the observable variable x is a linear combination of ξ_i,

$$x=\mathbf{t}\cdot\xi \ . \tag{21}$$

We can therefore rewrite the last equation of (19) as

$$x_{n+1}=(\lambda^n\hat{t}\xi_1)+(\mathbf{p}_{n+1}L(\hat{I}-\hat{\lambda})\hat{t}\alpha) \ , \tag{22}$$

where

$$L=\begin{bmatrix}\lambda_1^{n-1} & \cdots & \lambda_n^{n-1}\\ \vdots & & \vdots\\ \lambda_1 & \cdots & \lambda_n\\ 1 & \cdots & 1\end{bmatrix}, \quad \lambda^n=\begin{bmatrix}\lambda_1^n\\ \vdots\\ \lambda_n^n\end{bmatrix},$$

$$\hat{t}=\begin{bmatrix}t_1 & 0 & 0\\ 0 & \ddots & 0\\ 0 & 0 & t_n\end{bmatrix}, \quad \mathbf{p}_{n+1}=\begin{bmatrix}p_2\\ \vdots\\ p_{n+1}\end{bmatrix} \ . \tag{23}$$

We can further rearrange Eq. (22) to express x_{n+1} as a function of $\mathbf{x}_n=(x_1,\ldots,x_n)$ and $\mathbf{p}_{n+1}=(p_2,\ldots,p_{n+1})$:

$$x_{n+1}=(\mathbf{a}\cdot\mathbf{x}_n)+[\alpha\hat{l}(\underline{I}-\hat{\lambda})L^T A\mathbf{p}_{n+1}]\,, \tag{24}$$

where

$$\mathbf{a}=\begin{bmatrix}1 & \lambda_1 & \cdots & \lambda_1^{n-1}\\ \vdots & \vdots & & \vdots\\ 1 & \lambda_n & \cdots & \lambda_n^{n-1}\end{bmatrix}^{-1}\lambda^n\,,$$
$$A=\begin{bmatrix}1 & 0 & \cdots & 0\\ -a_n & 1 & & \vdots\\ \vdots & & \ddots & 0\\ -a_2 & \cdots & -a_n & 1\end{bmatrix}. \tag{25}$$

Equation (24) can be rewritten as

$$x_{i+1}=a_n x_i+a_{n-1}x_{i-1}+\cdots+a_1 x_{i-n+1}+a_0+b_n p_i+\cdots+b_1 p_{i-n+1}\,. \tag{26}$$

Equations (24)–(26) provide the connection between the coefficients a_i, b_i, and the phase space description of the system, as used in the OGY control algorithm. Specifically, the eigenvalues of the system are the roots of the polynomial

$$-\lambda^n+a_n\lambda^{n-1}+\cdots+a_2\lambda+a_1=0\,, \tag{27}$$

and the b_i coefficients are linear combinations of the projections of the shift vector. Equation (24) is related to the Laplace transformation from the state space realization to the transfer function widely used in classical control theory [30].

The $2n+1$ unknown coefficients of Eq. (26) can be calculated from the time series of a single observable variable. If n is the dimensionality of the system, then $3n+1$ successive readings of the variable and $3n+1$ corresponding perturbations are required for the solution. Since n previous perturbations and observations are required to predict the future of the system according to Eq. (26), the control law should involve the same number of variables.

The control perturbation for the $i+1$ step is calculated from the equation

$$p_{i+1}=q_n x_i+q_{n-1}x_{i-1}+\cdots+q_1 x_{i-n+1}+q_0+r_{n-1}p_i+\cdots+r_1 p_{i-n+1}\,, \tag{28}$$

using the pole placement technique for recursive models [30]. The coefficients q_1-q_n and r_1-r_{n-1} are the solution of the linear system

$$\begin{bmatrix}a_n & -1 & 0 & \cdots & 0 & b_n & 0 & 0 & \cdots & 0\\ a_{n-1} & a_n & -1 & \cdots & 0 & b_{n-1} & b_n & 0 & \cdots & 0\\ \cdot & \cdot & \cdot & \cdots & -1 & \cdot & \cdot & \cdot & \cdots & 0\\ a_1 & a_2 & \cdot & \cdots & a_n & b_1 & b_2 & \cdot & \cdots & b_n\\ 0 & a_1 & \cdot & \cdots & a_{n-1} & 0 & b_1 & \cdot & \cdots & b_{n-1}\\ 0 & 0 & \cdot & \cdots & \cdot & 0 & 0 & \cdot & \cdots & \cdot\\ 0 & 0 & 0 & \cdots & a_1 & 0 & 0 & 0 & \cdots & b_1\end{bmatrix}\begin{bmatrix}1\\ -r_{n-1}\\ \cdot\\ -r_1\\ q_n\\ \cdot\\ \cdot\\ q_1\end{bmatrix}=\begin{bmatrix}l_{2n-1}\\ \cdot\\ \cdot\\ \cdot\\ \cdot\\ \cdot\\ \cdot\\ l_1\end{bmatrix}, \tag{29}$$

where the l_i are the $2n-1$ coefficients that correspond to the target eigenvalues of the controlled system:

$$-\lambda^{*2n-1}+l_{2n-1}\lambda^{*2n-2}+\cdots+l_2\lambda^*+l_1=0\,. \tag{30}$$

We note that the overall dimensionality of the controlled system is increased by $(n-1)$.

In general, the dimensionality of the system will not be known in advance. Nor can the effective number of degrees of freedom always be deduced from the evolution of the autonomous system in the linear region of the unstable fixed point. The parameter perturbations used for control may shift the system onto stable manifolds not evident in the unperturbed case and reveal additional dimensions. On the other hand, the effective dimensionality can be determined by interrogating the system with the method outlined above. For spatiotemporal systems, most of the infinite number of modes will decay rapidly compared to the sampling period. We follow the suggestion by Auerbach *et al.* [28] of lumping all the highly attracting manifolds together as one. The effective dimensionality is therefore equal to the number of unstable and slowly attracting stable manifolds plus one. The method of determining n will be illustrated with reference to a particular example in the next section.

IV. STABILIZING HIGH-DIMENSIONAL STATES OF THE KURAMOTO-SIVASHINSKY EQUATION

The Kuramoto-Sivashinsky (KS) equation is one of the simplest nonlinear partial differential equations for modeling spatiotemporal chaos. It has been found to mimic the dynamical behavior of many different physical systems, but is most often used to model the spatiotemporal evolution of 2D flame fronts [33]. The governing equation for the contour of the front has the form

$$\frac{\partial\psi}{\partial t}-\left[\frac{\partial\psi}{\partial z}\right]^2+\frac{\partial^2\psi}{\partial z^2}+\frac{\partial^4\psi}{\partial z^4}=0\,. \tag{31}$$

We use the KS equation as an example of a multidimensional system that can be stabilized with the control algorithm. With a reaction zone width of $L=35.0$, a symmetrical four-cell solution is found to be unstable and

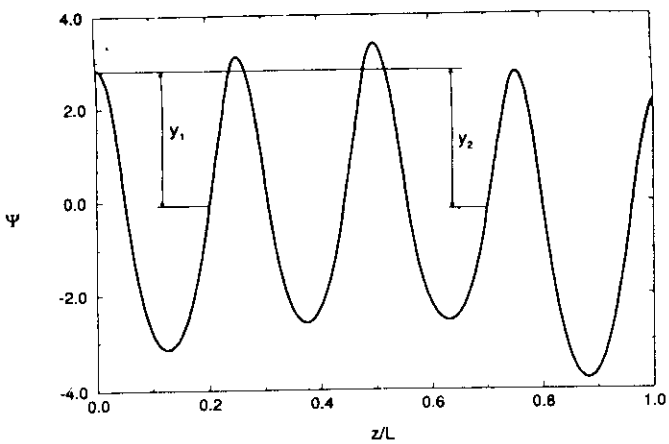

FIG. 2. Four-cell solution of the KS equation for the system width $L=35.0$. The symmetrical solution is unstable at this value of L, and this profile shows a snapshot in the early evolution away from the symmetrical state. The observables $y_1=\Psi(0)-\Psi(0.2)$ and $y_2=\Psi(0)-\Psi(0.7)$ are used to monitor the spatiotemporal evolution of the profile.

the system diverges away from this state to exhibit spatiotemporal chaos. Figure 2 shows the front as it moves away from the symmetrical state and the two quantities, y_1 and y_2, that serve as the "experimental" observables to monitor the spatiotemporal evolution of the profile. A two-dimensional projection of the phase portrait constructed from these observables is shown in Fig. 3, where the system is evolving away from the unstable state. Although the evolution of the system is followed very close to the unstable state, it is clear that the behavior is high dimensional. Generally, the time series of only one observable variable provides enough information for control. Figure 4 shows the corresponding time series generated from the observable y_1, which is used as the monitored variable in the control algorithm. The points in

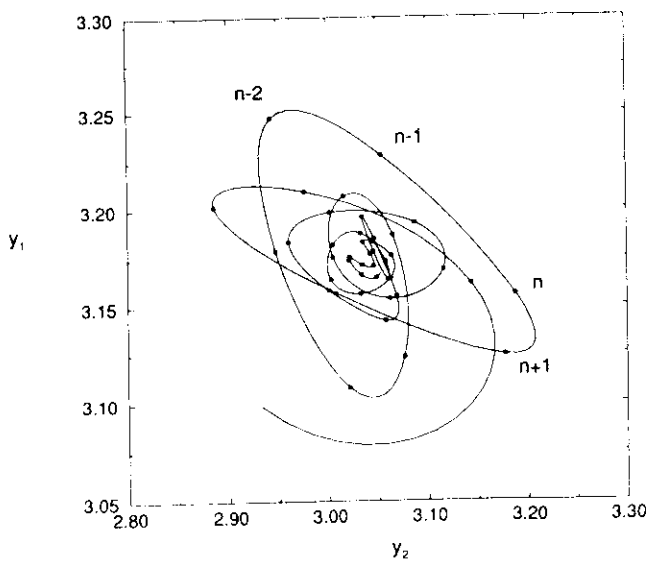

FIG. 3. Phase portrait showing evolution of system away from symmetrical four-cell solution. Two-dimensional projection is constructed from the observables y_1 and y_2.

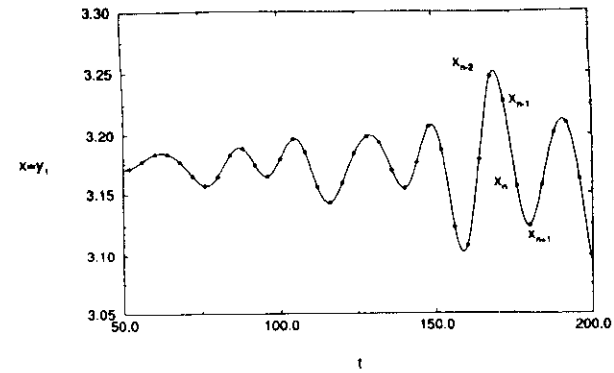

FIG. 4. Time series showing observable y_1 used in identification and control as the system evolves away from the symmetrical four-cell solution.

Figs. 3 and 4 show the sampling times of the monitored variable.

A. Determination of dimensionality

The evolution of the four-cell front away from the unstable symmetric solution—where a random perturbation is applied to a selected parameter at each sampling interval—is shown in the *identification* part of Fig. 5. The parameter chosen for perturbation is the gradient $\partial\psi/\partial z$ at $z=0$. The unperturbed boundary condition, corresponding to the autonomous system in Figs. 3 and 4, is $\partial\psi/\partial z=0$ at this point. In general we utilize "mirror" boundary conditions, where the first and third derivatives in Eq. (31) are required to be zero at the boundaries.

The data pairs (x_i,p_i) from the perturbed system (up to $t=250.0$ in Fig. 5) are used to determine the dimension and the corresponding eigenvalues of the autonomous system. Error estimates for different choices of n are obtained by summing the error between the measurements and the optimized n-dimensional fit to Eq. (26) over the entire data set. Figure 6 shows the variation of this error

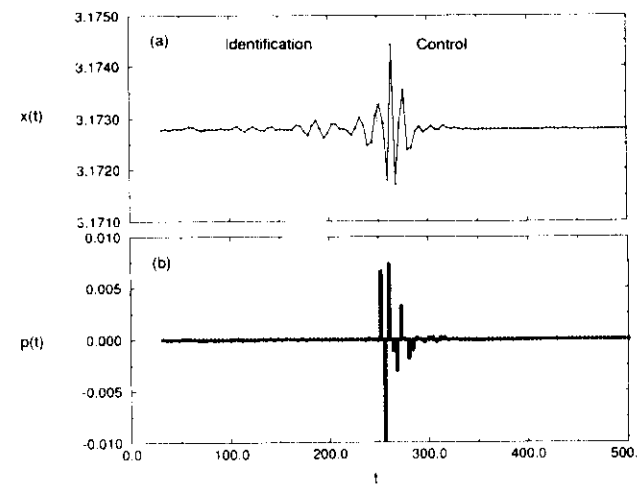

FIG. 5. Identification and control of the unstable symmetrical four-cell solution of the Kuramoto-Sivashinsky equation. (a) Value of observable x_i during identification and control phases, and (b) value of the controlling parameter p_{i+1}.

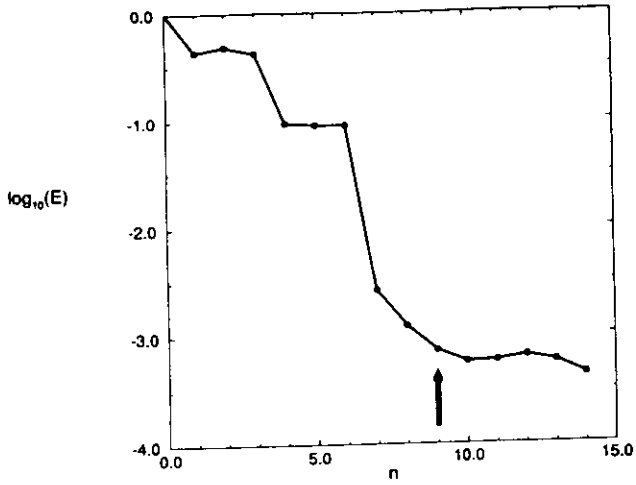

FIG. 6. Dependence of the fitting error of Eq. (26) on n, showing the plateau from $n=9$. An effective dimensionality of $n=9$ is used for stabilization of the symmetrical four-cell front shown in Fig. 2. Error E is calculated with respect to the standard deviation of the predicted amplitude error relative to the average amplitude of oscillation as shown in the *identification* stage of Fig. 5(a).

as a function of n. For $n \geq 9$, there is no significant reduction in the fitting error on increasing the effective dimension, so we choose $n=9$ for this system. It should be noted that the small error for convergence (typically 10^{-3} to 10^{-4}) suggests that it may be difficult to determine dimension from experimental data with this method due to the possibility of noise at higher magnitudes than the convergence criterion. The eigenvalues of the unstable four-cell solution are calculated as the roots of the equation

$$-\lambda^9+a_9\lambda^8+\cdots+a_2\lambda+a_1=0\ , \tag{32}$$

which are shown in Fig. 7. There are six unstable eigenvalues (modulus >1) and three stable eigenvalues, the latter corresponding to modes excited by the parameter perturbations. The eigenvalue of smallest magnitude represents the lumping of an infinite number of stable modes that decay quickly compared to the sampling interval.

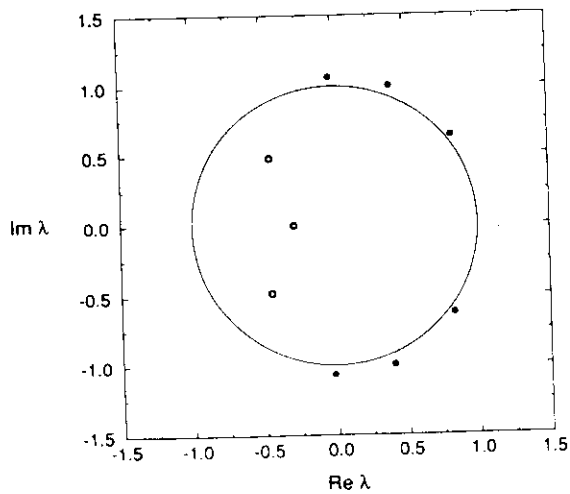

FIG. 7. Eigenvalues of the unstable four-cell solution calculated as roots of Eq. (32). Solid dots represent the unstable eigenvalues of the autonomous system. Open circles show the stable eigenvalues obtained by interrogating the system with random perturbations.

B. Stabilization of steady four-cell front

Once n and the coefficients a_i and b_i are determined, the algorithm is implemented in the control stage from $t=250.0$. All the eigenvalues of the closed-loop system were chosen to be zero by setting $l_i=0$ in Eq. (29). As indicated in Fig. 5, the state is effectively stabilized after the first cycle of nine perturbations. The control algorithm is applied continuously, with the values of the coefficients revised after each sampling and then used to calculate the next perturbation. In the present example, the magnitude of the control perturbations becomes very small after two cycles, or on the 19th iteration of the algorithm. We note that stabilization was also achieved with assumed system dimensionalities of $n=10$ and 11. The higher-order control laws are less desirable in experimental settings, however, due to their higher sensitivity to errors.

C. Stabilization of periodic two-cell front

The Kuramoto-Sivashinsky equation exhibits fronts with different numbers of cells on increasing the reaction zone width L. Each of these fronts loses its temporal stability through a bifurcation sequence that leads to chaotic behavior before the next front with more cells is established. We now examine the spatiotemporal behavior of a two-cell front in order to apply the control algorithm to a periodic orbit with more than one unstable direction. Specifically, we will stabilize and track a period-1 limit cycle through a secondary Hopf bifurcation, where the orbit is characterized by two unstable directions. The oscillatory front is monitored by recording the position of the minimum in the front profile. The minimum in the temporal oscillations is then used as the system observable. This choice eliminates the need to construct the $n-1$ dimensional Poincaré section in time-delay coordinates and is therefore convenient for monitoring high-dimensional periodic states of unknown dimensionality. Possible shifts of the attractor [25] do not cause difficulties because such effects are automatically incorporated into Eq. (24) from the identification procedure. The bifurcation diagram is shown in Fig. 8, where the minimum of oscillation is plotted as a function of the reaction zone width. (Further examples of spatiotemporal behavior in the two-cell KS front along with a detailed description of the monitoring technique can be found in Ref. [19].)

The two-cell solution exhibits period-1 oscillations at a reaction zone width of $L=20.7$, where we begin tracking. As the width is decreased, the period-1 orbit becomes unstable through a secondary Hopf bifurcation at $L=20.57$ with the appearance of quasiperiodic behavior. At $L=20.4$, the imaginary part of the eigenvalues responsible for the quasiperiodic behavior become zero and two

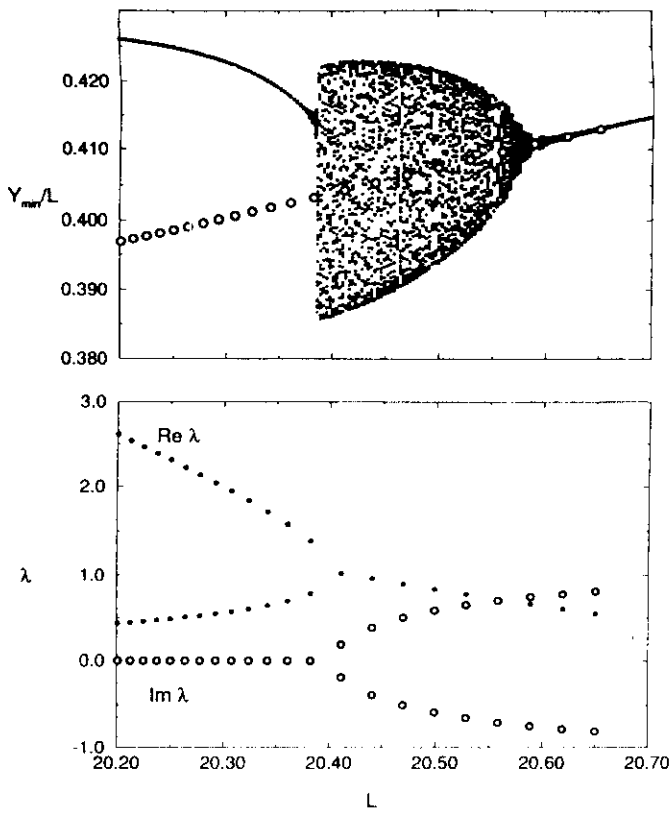

FIG. 8. Bifurcation diagram showing quasiperiodic behavior of the two-cell front of the KS equation. (a) Solid points show minimum of oscillations of front profile minimum. Open circles show the symmetrical oscillatory state tracked from right to left through the secondary Hopf bifurcation and quasiperiodic oscillations to the region where the unsymmetrical period-1 oscillation is stable. (b) The real (Re) and imaginary (Im) parts of the eigenvalues as a function of L shown by solid and open circles, respectively.

new period-1 solutions appear. As L is decreased further, the quasiperiodic behavior enters the basin of attraction of one of the stable period-1 solutions and nonsymmetric periodic oscillations are exhibited.

The symmetric period-1 solution was stabilized and tracked through the range of L shown in Fig. 8 (a) using the control algorithm with $n=2$. The controlling perturbation of the boundary condition was found to introduce a negligible displacement along the stable manifolds; therefore, it was necessary to explicitly consider only two unstable degrees of freedom for control. The algorithm was applied according to Eq. (28), with small random perturbations added to the control perturbations to interrogate the system. This technique allows the coefficients to be updated every time the bifurcation parameter is changed by repeating the identification procedure. The eigenvalues of the periodic state were calculated from the roots of Eq. (12) and are shown in Fig. 8 (b).

V. CONCLUSIONS

A general method for the control of unstable steady or periodic states of dynamical systems has been presented. The algorithm requires only a single observable quantity and acts through perturbations imposed on a single system parameter. For an n-dimensional system, n previous observations and $n-1$ previous perturbations are required for control. The states that are stabilized under this control correspond directly to the states of the autonomous system. The algorithm also provides a full characterization of the autonomous state in terms of its effective dimensionality and eigenvalues. The approach can be readily applied to experimental systems without any knowledge of the underlying mechanism or governing equations.

The effective reduction of high-dimensional dynamics to a single variable makes the method especially useful for stabilizing spatiotemporal systems by small perturbations localized in space. Local perturbations were sufficient for stabilizing stationary and periodic behavior in the Kuramoto-Sivashinsky equation. We note, however, that this approach may be less successful in spatiotemporal systems with a lower degree of spatial correlation. Local application of the algorithm in such systems will likely result in stabilization only within a correlation radius.

Selection of a particular unstable behavior is also possible using the control algorithm. Setting one of the closed-loop eigenvalues to be the same as the eigenvalue of a chosen unstable manifold will result in a control law that stabilizes all but the selected unstable manifold. This approach requires only very small perturbations and can be used to manipulate the dynamics of a high-dimensional system by observing only a single variable. The method may provide a more precise implementation of "anticontrol" recently demonstrated in experiments with hippocampal brain tissue [11].

When coupled with tracking techniques, the algorithm provides a model-independent, path-following method for the bifurcation analysis of experimental systems. The availability of the eigenvalues means that the character of bifurcations in experimental systems can be determined directly, rather than by inference from observations of qualitative changes in the time series. The algorithm can also be used to extend the parameter range of desired responses, such as stable burning in flame systems or steady output in high-dimensional lasers. It should also be noted that even though the method has been illustrated using a discrete-time approach, it can be reformulated in a continuous-time framework. Such a modification might allow the stabilization of very fast processes by using a control law that is precalculated and then implemented with an analog circuit.

ACKNOWLEDGMENTS

We thank the National Science Foundation (Grant No. CHE-9222616) and the Office of Naval Research (Grant No. N00014-95-1-0247) for supporting this research. Acknowledgment is made to the donors of The Petroleum Research Fund, administered by the American Chemical Society, for partial support of this research.

[1] T. Shinbrot, C. Grebogi, E. Ott, and J. A. Yorke, Nature **363**, 411 (1993).
[2] W. L. Ditto, S. N. Rauseo, and M. L. Spano, Phys. Rev. Lett. **65**, 3211 (1990).
[3] E. R. Hunt, Phys. Rev. Lett. **67**, 1953 (1991).
[4] T. Carroll, I. Triandaf, I. B. Schwartz, and L. Pecora, Phys. Rev. A **46**, 6189 (1992).
[5] R. Roy, T. W. Murphy, T. D. Maier, Z. Gills, and E. R. Hunt, Phys. Rev. Lett. **68**, 1259 (1992).
[6] S. Bielawski, D. Derozeir, and P. Glorieux, Phys. Rev. A **47**, R2492 (1993).
[7] V. Petrov, V. Gáspár, J. Masere, and K. Showalter, Nature **361**, 240 (1993).
[8] P. Parmananda, P. Sherard, R. W. Rollins, and H. D. Dewald, Phys. Rev. E **47**, R3003 (1993).
[9] F. W. Schneider, R. Blittersdorf, A. Förster, T. Hauck, D. Lebender, and J. Müller, J. Phys. Chem. **97**, 12 244 (1993).
[10] A. Garfinkel, M. L. Spano, W. L. Ditto, and J. N. Weiss, Science **257**, 1230 (1992).
[11] S. J. Schiff, K. Jerger, D. H. Duong, T. Chang, M. L. Spano, and W. L. Ditto, Nature **370**, 615 (1994).
[12] E. Ott, C. Grebogi, and J. A. Yorke, Phys. Rev. Lett. **64**, 1196 (1990).
[13] K. Pyragas, Phys. Lett. A **170**, 421 (1992).
[14] K. Pyragas and A. Tamasevicius, Phys. Lett. A **180**, 99 (1993).
[15] P. M. Alsing, A. Gavrielides, and V. Kovanis, Phys. Rev. E **50**, 1968 (1994).
[16] B. Peng, V. Petrov, and K. Showalter, J. Phys. Chem. **95**, 4957 (1991).
[17] V. Petrov, B. Peng, and K. Showalter, J. Chem. Phys. **96**, 7506 (1992).
[18] V. Petrov, M. F. Crowley, and K. Showalter, Phys. Rev. Lett. **72**, 2955 (1994).
[19] V. Petrov, M. F. Crowley, and K. Showalter, J. Chem. Phys. **101**, 6606 (1994).
[20] S. Bielawski, D. Derozeir, and P. Glorieux, Phys. Rev. E **49**, R971 (1994).
[21] Z. Gills, C. Iwata, R. Roy, I. B. Schwartz, and I. Triandaf, Phys. Rev. Lett. **69**, 3169 (1992).
[22] A. Hjelmfelt and J. Ross, J. Phys. Chem. **94**, 1176 (1994).
[23] S. Bielawski, M. Bouazaoui, D. Derozeir, and P. Glorieux, Phys. Rev. A **47**, 3276 (1993).
[24] R. W. Rollins, P. Parmananda, and P. Sherard, Phys. Rev. E **47**, R780 (1993).
[25] U. Dressler and G. Nitsche, Phys. Rev. Lett. **68**, 1 (1992).
[26] D. Auerbach, Phys. Rev. Lett. **72**, 1184 (1994).
[27] G. Hu and Z. Qu, Phys. Rev. Lett. **72**, 68 (1994).
[28] D. Auerbach, C. Grebogi, E. Ott, and J. A. Yorke, Phys. Rev. Lett. **69**, 3479 (1992).
[29] F. J. Romerias, C. Grebogi, E. Ott, and W. P. Dayawansa, Physica D **58**, 165 (1992).
[30] G. C. Goodwin and K. S. Sin, *Adaptive Filtering, Prediction, and Control* (Prentice-Hall, Englewood Cliffs, NJ, 1984).
[31] L. Ljung, *System Identification—Theory for the User* (Prentice-Hall, Englewood Cliffs, NJ, 1987).
[32] J. C. Dole, K. Glover, P. Khargonekar, and B. Francis, IEEE Trans. Automat. Contr. **34**, 1831 (1989).
[33] G. I. Sivashinsky, Annu. Rev. Fluid Mech. **15**, 179 (1983).

Tracking Unstable Turing Patterns through Mixed-Mode Spatiotemporal Chaos

Valery Petrov,[1] Stephane Metens,[2] Pierre Borckmans,[2] Guy Dewel,[2] and Kenneth Showalter[1,2]

[1]*Department of Chemistry, West Virginia University, Morgantown, West Virginia 26506-6045*

[2]*Service de Chimie Physicque, Université Libre de Bruxelles, Campus Plaine, 1050 Bruxelles, Belgium*

(Received 19 May 1995)

A method is presented for stabilizing and tracking unstable Turing patterns in reaction-diffusion systems. The Gray-Scott model is used to simulate a chemical system exhibiting spatiotemporal chaos arising from the interaction between Turing and Hopf bifurcations. The local behavior of the unstable pattern is first approximated with a single-input, single-output linear model constructed from a time series. A recursive control algorithm is then used to stabilize and track the unstable pattern by monitoring a single point in space and making small adjustments to a global parameter.

PACS numbers: 82.40.Bj, 05.45.+b

Stabilization techniques based on the Ott-Grebogi-Yorke (OGY) [1] method have been highly successful for controlling low-dimensional systems [2]. Controlling spatiotemporal systems remains a challenge, however, because the unstable states in such systems are typically high dimensional, involving multiple stable and unstable modes. Some spatiotemporal systems can be controlled with simple methods, such as propagating fronts with highly correlated spatial modes [3], convectively unstable systems [4], or systems that are stabilized at multiple sites [5]. Periodic behavior in myocardium tissue [6] and hippocampal brain tissue [7] has been stabilized by deducing the stable and unstable manifold positions from time delay maps and applying appropriate perturbations. Simple control approaches typically fail, however, when the unstable state has more than one unstable direction. Auerbach *et al.* [8] and Romerias *et al.* [9] have generalized the OGY method for stabilizing systems with many stable and unstable manifolds.

We recently proposed a control method that combines the OGY approach with the classical control routines of single-input, single-output (SISO) systems [10]. The method was applied to stabilize unstable periodic orbits and steady states of the Kuramoto-Sivashinsky equation. In this Letter we demonstrate how the method can be applied to stabilize and track unstable Turing patterns through mixed-mode spatiotemporal chaos.

A recent study by De Wit, Dewel, and Borckmans [11] has shown how spatiotemporal chaos arises in reaction-diffusion systems near a Turing-Hopf codimension-2 bifurcation point. The interaction between the Turing and Hopf modes in the vicinity of such a point may result in *mixed-mode* spatiotemporal oscillations. We use the Gray-Scott cubic autocatalysis model [12] to simulate a 1D reaction-diffusion system exhibiting mixed-mode spatiotemporal chaos.

The governing equations of the reaction-diffusion Gray-Scott model [13] have the form

$$\frac{\partial \alpha}{\partial t} = \delta \nabla^2 \alpha + \frac{(1-\alpha)}{T_{\rm res}} - \alpha\beta^2,$$
$$\frac{\partial \beta}{\partial t} = \nabla^2 \beta + \frac{(\beta_0 - \beta)}{T_{\rm res}} + \alpha\beta^2 - k_2\beta, \qquad (1)$$

where $\nabla^2 = \partial^2/\partial x^2$ in the 1D case, and $\delta = D_\alpha/D_\beta$ is the ratio of the reactant and autocatalyst diffusion coefficients. The diffusion terms are calculated using finite differences, and no-flux boundary conditions are imposed at $x = 0$ and $x = 300$. We concentrate on the behavior of this system for the specific parameter values $\beta_0 = \frac{1}{15}$, $\kappa_2 = \frac{1}{40}$, and $\delta = 4.6$.

The bifurcation diagram corresponding to varying the remaining parameter $T_{\rm res}$ is shown in Fig. 1. The steady-state locus yields a "mushroom" pattern with two ranges of multiple steady states, one at low $T_{\rm res}$ and one at high $T_{\rm res}$. In addition, there is a Hopf bifurcation point along the uppermost branch of the mushroom. As the residence time is increased the homogeneous steady state loses stability at this point and a stable limit cycle emerges, with homogeneous oscillations displayed throughout the medium. As $T_{\rm res}$ is further increased, a Turing-Hopf mixed mode appears through a subharmonic instability. This new solution loses its stability and gives rise to complex spatiotemporal behavior.

Over the range $214.8 < T_{\rm res} < 242$, a Turing pattern with a typical stationary periodic concentration profile is observed. The maximum in $\alpha(x)$ of the spatial oscillations as a function of $T_{\rm res}$ is shown by the dotted line in Fig. 1. At high $T_{\rm res}$ the system settles back onto the limit cycle of the homogeneous oscillations. At low $T_{\rm res}$, the Turing branch becomes unstable as it enters the complex spatiotemporal region.

We now present a general method for controlling multidimensional systems using scalar time series (see Ref. [10] for a detailed description), which we will use for stabilizing the unstable Turing pattern through the range of complex behavior. Multidimensional systems are typically monitored by the observation of a single experi-

0031-9007/95/75(15)/2895(4)$06.00

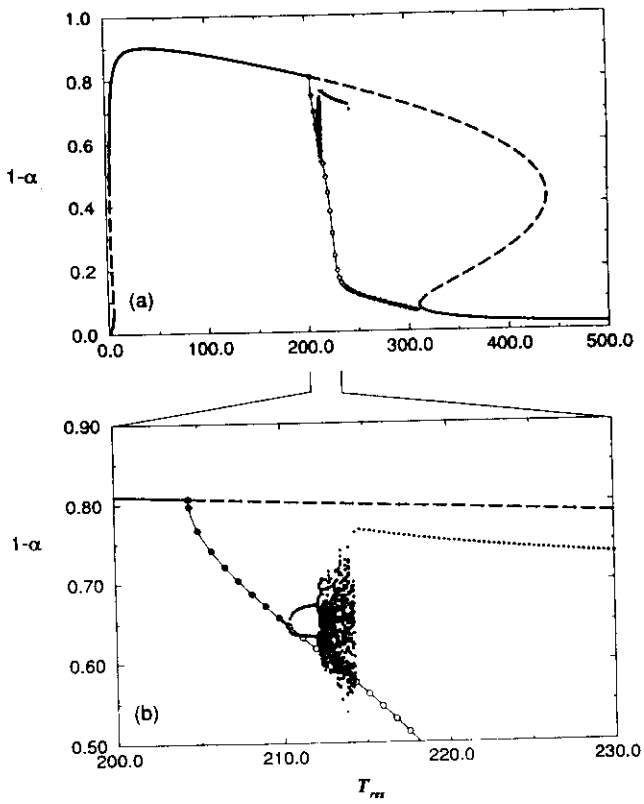

FIG. 1. (a) Homogeneous stable (solid line) and unstable (dashed line) steady state of the Gray-Scott model as a function of T_{res}. The circles show the locus of the stable (●) and unstable (○) uniform period-1 orbit. (b) Blowup of (a) near the region of complex spatiotemporal oscillations. The dots represent the minimum in $1 - \alpha$ along the spatial profile of the Turing pattern for $T_{res} > 214.8$ and show the minimum in $1 - \alpha$ oscillations at $x = 0$ for $T_{res} < 214.8$.

mentally accessible variable. Although the corresponding time series is a projection of the system dynamics in phase space, control can be achieved by using a set of time-delayed observations.

When an m-dimensional system is sampled with a time interval τ, the coordinate ξ_i along the ith eigenvector moves according to

$$\xi_i(t + \tau) - \xi_i^F = \lambda_i[\xi_i(t) - \xi_i^F], \quad i = 1, \ldots, m, \quad (2)$$

where $\vec{\xi}^F$ is the steady-state position and λ_i is the ith eigenvalue of the time-discretized system. We assume that there is an experimentally accessible parameter p which alters the dynamics in such a way that the fixed point moves when a small perturbation δp is applied. Following the application of such a perturbation, the system evolves according to the position of the shifted fixed point,

$$\vec{\xi}^F(p + \delta p) = \vec{\xi}^F(p) + \frac{\partial \vec{\xi}^F}{\partial p}\delta p. \quad (3)$$

For simplicity, we assume that $\vec{\xi}^F(p) = 0$. We also assume that the perturbation δp is kept constant from t to $t + \tau$ and is equal to $u(t + \tau)$. Equations (2) and (3) can then be combined to give the equations of motion in the presence of the perturbations:

$$\xi_i(t + \tau) = \lambda_i \xi_i(t) + (1 - \lambda_i)\frac{\partial \xi_i^F}{\partial p} u(t + \tau), \quad i = 1, \ldots, m. \quad (4)$$

If we introduce a time-shift operator $\hat{\mathbf{q}}$, such that $\hat{\mathbf{q}}^j(y(t)) = y(t + j\tau)$, we can rewrite Eq. (4) as

$$\xi_i(t) = \frac{\hat{\mathbf{q}}(1 - \lambda_i)}{\hat{\mathbf{q}} - \lambda_i}\frac{\partial \xi_i^F}{\partial p} u(t), \quad i = 1, \ldots, m. \quad (5)$$

In an experimental setting, we typically monitor some observable $y(t)$ that is a linear combination of the system variables:

$$y(t) = \sum_{i=1}^{m} c_i \xi_i(t). \quad (6)$$

We assume that $c_i \neq 0$ for all unstable eigenvectors, i.e., the unstable behavior *is observable* using $y(t)$. To combine Eqs. (5) and (6), we introduce the coefficients that are proportional to the shift of the steady state:

$$\gamma_i = c_i(1 - \lambda_i)\frac{\partial \xi_i^F}{\partial p}. \quad (7)$$

The relation between perturbation $u(t)$ and observable $y(t)$ can then be written as

$$y(t) = \sum_{i=1}^{m} \frac{\gamma_i \hat{\mathbf{q}}}{\hat{\mathbf{q}} - \lambda_i} u(t). \quad (8)$$

Equation (8) is a transfer function between the system input $u(t)$ and output $y(t)$. It models the response of the m-dimensional system to a perturbation. The common denominator form of this equation is

$$y(t) = \frac{b_1 \hat{\mathbf{q}}^m + b_2 \hat{\mathbf{q}}^{m-1} + \cdots + b_m \hat{\mathbf{q}}^1}{\hat{\mathbf{q}}^m + a_1 \hat{\mathbf{q}}^{m-1} + \cdots + a_m \hat{\mathbf{q}}^0} u(t). \quad (9)$$

The denominator of the transfer function is a polynomial whose roots are eigenvalues of the linearized system. Following Ref. [14], we denote the denominator of Eq. (9) as $\hat{\mathbf{A}}(q)$ and the numerator as $\hat{\mathbf{B}}(q)$. Equation (9) can now be rewritten in a compact form:

$$\hat{\mathbf{A}}(q)y(t) = \hat{\mathbf{B}}(q)u(t). \quad (10)$$

To find the coefficients from an experimental time series we express Eq. (10) as

$$y(n) = \sum_{i=1}^{m} -a_i y(n - i) + b_i u(n + 1 - i), \quad (11)$$

where $y(j) = y(t + j\tau)$ and $u(j) = u(t + j\tau)$. The coefficients a_i and b_i of Eq. (11) are calculated directly from the sampled time series of $u(t)$ and $y(t)$ as a solution of the linear system [10]. Rearranging Eq. (9) into the partial-fraction form of Eq. (8) gives the coefficients γ_i. Each γ_i tells how far the steady state is displaced along the ith eigenvector following the perturbation and, in many cases, allows an estimation of the effective system dimension. Specifically, if the system dimension is overestimated, then for some i, $|\gamma_i| \ll \min(|\gamma_j|_{j \neq i})$, the ith eigendirection can be discarded.

To stabilize a linear system modeled with Eq. (10), controlling perturbations are calculated as a linear function of n delayed readings and $n - 1$ previous perturbations:

$$\hat{\mathbf{L}}(q)u(t) = \hat{\mathbf{P}}(q)y(t), \quad (12)$$

where $\hat{\mathbf{L}}(q)$ and $\hat{\mathbf{P}}(q)$ are the mth order polynomials of successive powers of the time-shift operator [15]. The control law coefficients l_i and p_i determine the behavior of the closed-loop system according to Eqs. (10) and (12):

$$[\hat{\mathbf{A}}(q) \cdot \hat{\mathbf{L}}(q) - \hat{\mathbf{B}}(q)\hat{\mathbf{P}}(q)]y(t) = \hat{\mathbf{A}}^*(q)y(t) = 0, \quad (13)$$

where the center dot indicates multiplication of the polynomials. According to Eq. (13), $2m - 1$ eigenvalues of the closed-loop system can be set to any value with an appropriate choice of the coefficients l_i and p_i (the pole-placement technique) [10,15]. We require all eigenvalues of $\hat{\mathbf{A}}^*(q)$ to be stable (modulus < 1) so the system converges toward the fixed point.

We now demonstrate the stabilization of unstable Turing patterns with the 1D reaction-diffusion Gray-Scott model. The linearized recursive model of the dynamical system is obtained by imposing *random* perturbations onto the global parameter T_{res} at regular sampling intervals $\tau = 50.0$. Values of α at the system boundary $x = 0$ along with the applied perturbations produce a set of data pairs $(y(i), u(i))$. This set is fitted to Eq. (11) and the recursive coefficients a_i, b_i are calculated using the method of singular value decomposition. The coefficients l_i, p_i that determine the controlling perturbations are found as a solution of the linear system defined by Eq. (13).

Tracking an unstable state requires adaptive control, where the values of a_i and b_i are redetermined each step with the system in the vicinity of the state. Once the tracking is initiated, small random perturbations are added to the continuously applied controlling perturbations to interrogate the system. This technique allows the control coefficients to be updated every time the bifurcation parameter is changed.

To initialize the tracking procedure it is necessary to determine a solution for some value of the bifurcation parameter, find the effective dimensionality of the system in the linear region of that solution, and calculate the control coefficients. A suitable starting point can be found in the vicinity of a bifurcation that destabilizes the system. A stable Turing pattern with nine half-wavelengths is exhibited by Eq. (1) for $T_{\text{res}} = 217.0$. The appropriate value of m was determined during the initialization. It was found for $m = 4$ that γ_4 corresponds to $\lambda_4 \approx 0$, and it is 2 orders of magnitude smaller than the remaining γ_i. Therefore, the fourth (highly attractive) mode gives a negligible contribution to the time series readings and can be discarded. An effective system dimension of three was used to stabilize the Turing pattern.

One step of the tracking routine is illustrated in Fig. 2. The identification of the linearized dynamics is carried out during the first 50 iterations. Once the system identification is completed (at $i = 50$), the bifurcation parameter T_{res} is changed to a new value. Provided the change in T_{res} is sufficiently small, the old control parameters l_i and p_i are close to the new values and the system is stabilized. As shown in Fig. 2, the system converges to the new steady state following the change in T_{res} (at $i = 51$). The identification routine is then repeated after the convergence reaches a preset limit.

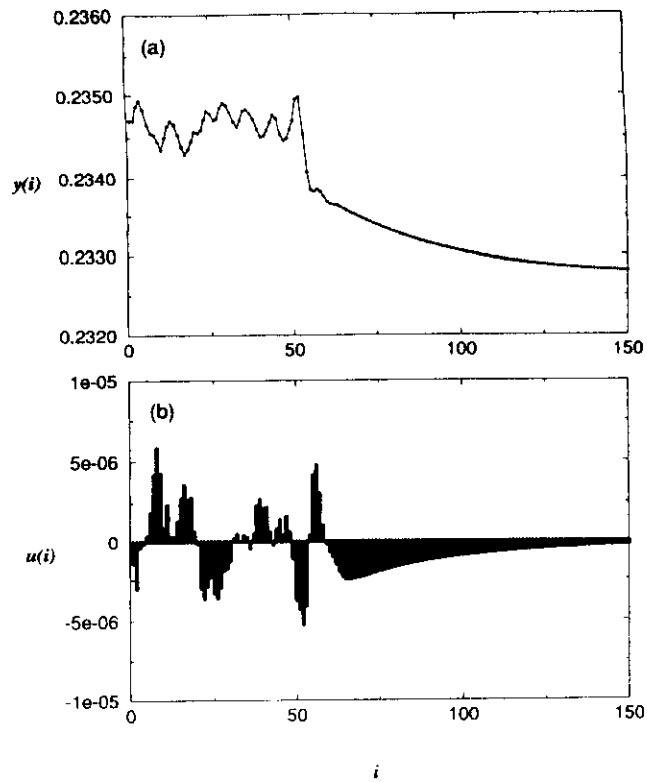

FIG. 2. Identification and tracking of unstable Turing pattern at $T_{\text{res}} = 214.5$. (a) Value of $y(i) = \alpha$ collected at $x = 0$; (b) the corresponding adjustments of $u(i) = T_{\text{res}}$.

The position of the stabilized Turing pattern was recorded for each step of the bifurcation parameter and is shown in Fig. 3(a). The three eigenvalues (Floquet multipliers) of the unstable Turing pattern are calculated as the roots of the denominator of Eq. (10). The absolute values of these roots are shown in Fig. 3(b). The two complex eigenvalues correspond to the uniform oscillatory mode that becomes unstable at $T_{\text{res}} = 214.8$ as T_{res} is decreased. The third (real) eigenvalue approaches unity as the residence time approaches the Turing bifurcation at $T_{\text{res}} = 210.7$. When T_{res} is below this value, the tracking algorithm switches to the stabilization of the uniform unstable steady state, as shown in Fig. 3(a).

The application of the tracking algorithm results in a qualitative change in behavior at the expense of very small perturbations to the system. The unstable Turing pattern is maintained throughout the region where the autonomous Gray-Scott system exhibits spatiotemporal chaos. Space-time plots of the autonomous and controlled systems at $T_{\text{res}} = 214.5$ are compared in Fig. 4.

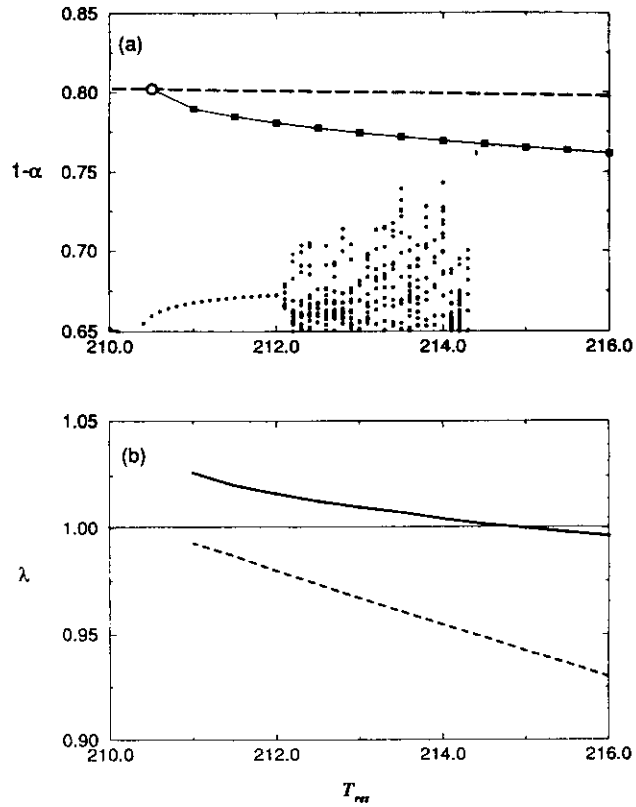

FIG. 3. Bifurcation diagram showing (a) the autonomous system response (●) and the tracked unstable Turing pattern (■). Open circle (○) shows stabilized homogeneous steady state. Unstable steady state (dashed line) is also shown. (b) Modulus of complex conjugate eigenvalues (solid line) and real eigenvalue (dashed line) corresponding to slowest decaying mode as a function of T_{res}.

A spatially distributed system has an infinite number of degrees of freedom; however, only two modes of the Turing pattern become unstable to produce the mixed-mode chaos. The third, stable mode appears as a response to the homogeneous perturbations. We note that the method can be readily applied to control higher dimensional states, and a four-cell front of the Kuramoto-Sivashinsky equation with three stable and six unstable modes has been stabilized [10].

When coupled with the tracking technique, the stabilization algorithm provices a model-independent continuation method for bifurcation analysis of experimental systems. We anticipate that the approach can be extended to control spatially distributed chemical and biological processes in two- and three-dimensional media by monitoring and perturbing the system at multiple locations separated by the characteristic correlation length.

K. S. is grateful to Professor Grégoire Nicolis for his hospitality at the Service de Chimie Physique, Université Libre de Bruxelles. We thank Anne De Wit for helpful discussions. K. S. thanks the National Science Foundation (Grant No. CHE-9222616), the Office of Naval Research (Grant No. N00014-95-1-0247), and the Petroleum Research Fund (Grant No. 29565-AC6) for supporting this research. P. B. and G. D. received support from the FNRS (Belgium).

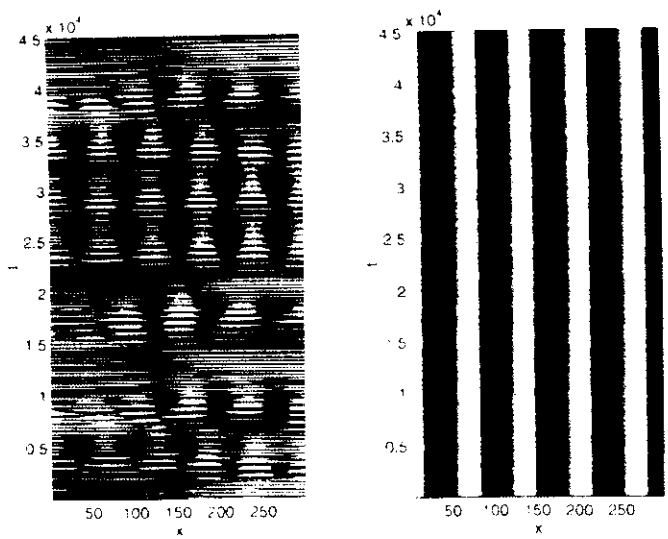

FIG. 4. Space-time plot of autonomous (left) and controlled (right) Gray-Scott system at $T_{res} = 214.5$.

[1] E. Ott, C. Grebogi, and J. A. Yorke, Phys. Rev. Lett. **64**, 1196 (1990).

[2] For reviews see T. Shinbrot, C. Grebogi, E. Ott, and J. A. Yorke, Nature (London) **363**, 411 (1993); W. L. Ditto and L. Pecora, Sci. Am., Aug. 1993, p. 78; E. Ott and M. Spano, Phys. Today **48**, No. 5, 34 (1995); K. Showalter, Chem. Br. **31**, 202 (1995).

[3] V. Petrov, M. F. Crowley, and K. Showalter, J. Chem. Phys. **101**, 6606 (1994).

[4] D. Auerbach, Phys. Rev. Lett. **72**, 1184 (1994); G. A. Johnson, M. Locher, and E. R. Hunt, Phys. Rev. E **51**, R1625 (1995).

[5] J. A. Sepulchre and A. Babloyantz, Phys. Rev. E **48**, 945 (1993).

[6] A. Garfinkel, M. L. Spano, W. L. Ditto, and J. N. Weiss, Science **257**, 1230 (1992).

[7] S. J. Schiff, K. Jerger, D. H. Duong, T. Chang, M. L. Spano, and W. L. Ditto, Nature (London) **370**, 615 (1994).

[8] D. Auerbach, C. Grebogi, E. Ott, and J. A. Yorke, Phys. Rev. Lett. **69**, 3479 (1992).

[9] F. J. Romerias, C. Grebogi, E. Ott, and W. P. Dayawansa, Physica (Amsterdam) **58D**, 165 (1992).

[10] V. Petrov, E. Mihaliuk, S. K. Scott, and K. Showalter, Phys. Rev. E **51**, 3988 (1995).

[11] A. De Wit, G. Dewel, and P. Borckmans, Phys. Rev. E **48**, R4191 (1993).

[12] P. Gray and S. K. Scott, Chem. Eng. Sci. **39**, 1087 (1984).

[13] W. N. Reynolds, J. E. Pearson, and S. Ponce-Dawson, Phys. Rev. Lett. **72**, 2797 (1994); V. Petrov, S. K. Scott, and K. Showalter, Philos. Trans. R. Soc. London A **443**, 631 (1994).

[14] L. Ljung, *System Identification—Theory for the User* (Prentice-Hall, Englewood Cliffs, NJ, 1984).

[15] G. C. Goodwin and K. S. Sin, *Adaptive Filtering, Prediction, and Control* (Prentice-Hall, Englewood Cliffs, NJ, 1984).

Nonlinear Control of Dynamical Systems from Time Series

Valery Petrov and Kenneth Showalter*
Department of Chemistry, West Virginia University, Morgantown, West Virginia 26506-6045
(Received 20 September 1995)

Feedback control of multidimensional, nonlinear single-input single-output systems is formulated in terms of an invariant hypersurface in the delayed state space of a system observable and a control parameter. The surface is created directly from the response of the system to random perturbations, providing a model-independent nonlinear control algorithm. The algorithm can be used to stabilize unstable states or to drive a system to any particular objective state in a minimum number of steps. [S0031-9007(96)00095-6]

PACS numbers: 05.45.+b, 82.40.Bj

The OGY (Ott-Grebogi-Yorke) [1] method for stabilizing unstable periodic orbits initiated a flurry of theoretical developments and experimental applications of feedback control to nonlinear dynamical systems [2–11]. Recent advances in control of high-dimensional systems offer new possibilities for manipulating complex temporal and spatiotemporal behavior [12–14]. All of these methods, however, are based on linearized models and the feedback control is therefore restricted to small perturbations in the linear regime. Here we present a new, integrated approach for nonlinear feedback control, where the response of the system to random perturbations is used directly to construct the control law as a multidimensional surface in the time-delayed space.

We demonstrate the approach with the Gray-Scott model for cubic autocatalysis in a flow reactor [15]. The governing dimensionless equations have the form

$$\begin{aligned} \partial\alpha/\partial t &= (1 - \alpha)/T_{\mathrm{res}} - \alpha\beta^2, \\ \partial\beta/\partial t &= (\beta_0 - \beta)/T_{\mathrm{res}} + \alpha\beta^2 - \kappa_2\beta. \end{aligned} \tag{1}$$

With $\beta_0 = \frac{1}{15}$, $\kappa_2 = 0$, the model is one-dimensional and displays one unstable and two stable stationary states over the range of reciprocal residence time $1/T_{\mathrm{res}} = 0.23$–$0.35$. Transitions from one stable state to the other can be induced by applying appropriate perturbations to $1/T_{\mathrm{res}}$. Perturbations can also move the system to the unstable stationary state, but it will relax back to one of the stable states unless some form of feedback stabilization is applied.

We now describe how to control transitions between the stable and unstable states using a nonlinear control surface constructed from time series. For a one-dimensional system, the control surface is constructed by observing the transitions from an initial state $x_I(t)$ to a final state $x_F(t + \tau)$ that result from the application of perturbation p during the sampling interval τ. The collected triplets of values (x_I, x_F, p) lie on a surface in a three-dimensional space. This nonlinear surface,

$$p_{I\to F} = C(x_I, x_F), \tag{2}$$

defines the perturbation that moves the system from an initial state x_I to a desired final state x_F in one iteration. Even though the identification stage can produce only a finite number of points, linear interpolation between closest neighbors can be used to construct the remainder of the surface.

Figure 1 shows the control surface for (1) generated from a series of responses to sequential random perturbations. The solid (open) circle corresponds to a transition from a stable (unstable) state to the coexisting unstable (stable) state in the region of bistability. Figure 2 shows a time series with transitions between the stable and unstable states. A similar procedure can be used for targeting and stabilizing fixed points in 1D return maps.

The control of multidimensional systems is more challenging since the initial and final states of (2) are no longer defined by the readings before and after the sampling interval. To derive an analogue of the control surface for such systems we first consider a linear two-dimensional model and then generalize to include extra dimensions and nonlinear terms. The time discretized behavior of a linear two-variable system around a stationary state can be decomposed into the motion along the

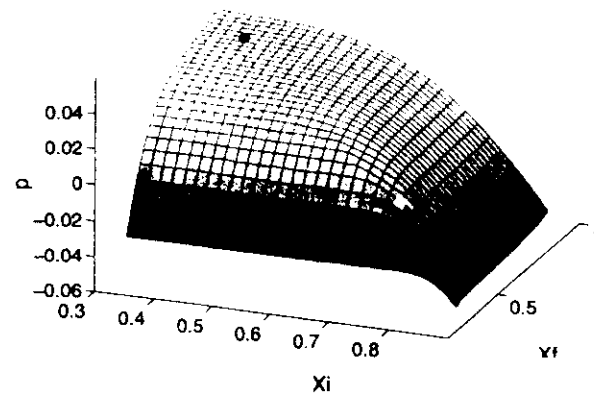

FIG. 1. Control surface for time-discretized ($\tau = 5.0$) one-dimensional bistable system (1) at $1/T_{\mathrm{res}} = 0.3$. The perturbation $p_i = 1/T_{\mathrm{res}} - 0.3$ and the observable $x_i = \alpha(t_i)$. Solid circle corresponds to transition from a stable state ($x_I = 0.41$) to the unstable state ($x_F = 0.76$); open circle shows perturbation required to move the system from the unstable to the stable state (in one iteration).

 0031-9007/96/76(18)/3312(4)$10.00

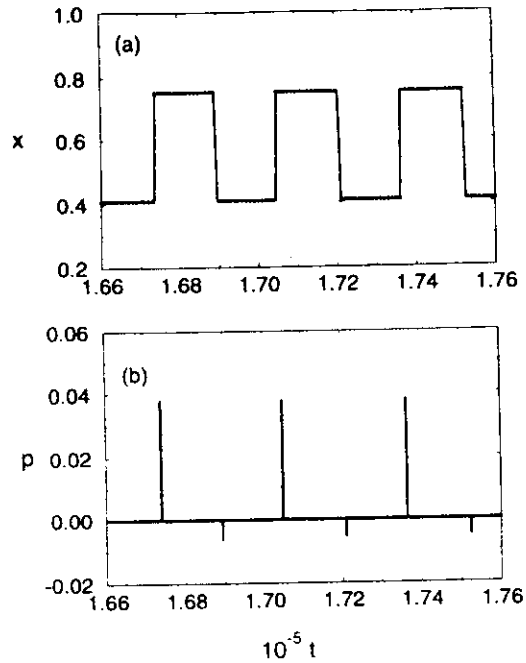

FIG. 2. (a) Time series of the one-dimensional bistable system (1) as it is moved from the stable state to the unstable state and back again; (b) applied perturbations.

eigenvectors ξ and η:

$$\begin{aligned} \xi_{i+1} &= \lambda_\xi \xi_i + (1 - \lambda_\xi)\alpha_\xi p_{i+1}, \\ \eta_{i+1} &= \lambda_\eta \eta_i + (1 - \lambda_\eta)\alpha_\eta p_{i+1}, \end{aligned} \tag{3}$$

where λ_ξ, λ_η are the eigenvalues along the corresponding eigenvectors, and $\alpha_\xi = \partial \xi_S/\partial p$ and $\alpha_\eta = \partial \eta_S/\partial p$ are the shifts of the stationary state arising from the applied perturbation. The perturbation is constant during the iteration, and when $p = 0$ the stationary state is at the origin.

We assume the availability of only one observable on which the system dynamics is projected with some coefficients t_ξ and t_η:

$$x_i = t_\xi \xi_i + t_\eta \eta_i. \tag{4}$$

If the system is initially at the state ξ_i, η_i, the next observations of x will then be defined by Eqs. (3) and (4), with x_{i+1} being a linear combination of ξ_i, η_i, and p_{i+1},

$$x_{i+1} = \lambda_\xi t_\xi \xi_i + \lambda_\eta t_\eta \eta_i + A p_{i+1}, \tag{5}$$

and x_{i+2}, which also includes p_{i+2},

$$x_{i+2} = \lambda_\xi^2 t_\xi \xi_i + \lambda_\eta^2 t_\eta \eta_i + B p_{i+1} + A p_{i+2}. \tag{6}$$

where

$$\begin{aligned} A &= (1 - \lambda_\xi)\alpha_\xi t_\xi + (1 - \lambda_\eta)\alpha_\eta t_\eta, \\ B &= (1 - \lambda_\xi)\lambda_\xi \alpha_\xi t_\xi + (1 - \lambda_\eta)\lambda_\eta \alpha_\eta t_\eta. \end{aligned} \tag{7}$$

It follows from (4) and (5) that the state of the system (i.e., the coordinates along the system manifolds) at iteration i or $i + 1$ can be reconstructed from two time-delayed readings of the observable and the perturbation applied to the system. Analogous arguments for an m-dimensional system define the state as a linear combination of m delayed observations and $m - 1$ perturbations:

$$\begin{aligned} &(\xi_i, \eta_i, \ldots) \\ &= L_D(x_i, x_{i-1}, \ldots, x_{i-m+1}; p_i, p_{i-1}, \ldots, p_{i-m+2}), \end{aligned} \tag{8}$$

where L_D is a linear function.

Once the system state is known, the control perturbations can be applied to direct the system to a desired objective state. We assume that only one control parameter is available to alter the system dynamics. From the second iteration of (3),

$$\begin{aligned} \xi_{i+2} &= \lambda_\xi^2 \xi_i + (1 - \lambda_\xi)\alpha_\xi(\lambda_\xi p_{i+1} + p_{i+2}), \\ \eta_{i+2} &= \lambda_\eta^2 \eta_i + (1 - \lambda_\eta)\alpha_\eta(\lambda_\eta p_{i+1} + p_{i+2}), \end{aligned} \tag{9}$$

we see that two perturbations, p_{i+1} and p_{i+2}, can move the system from any initial state (ξ_i, η_i) to any final state (ξ_{i+2}, η_{i+2}) provided that $\lambda_\xi \neq \lambda_\eta$, $\lambda_\xi, \lambda_\eta \neq 1$ and $\alpha_\xi, \alpha_\eta \neq 0$ [13]. The control perturbations are a linear combination of the initial and final states. Even though a sequence of two perturbations must be applied before the desired state is reached, it is necessary to determine only the first perturbation explicitly, since the second is calculated using the same expression at the next iteration with the updated readings. For the linear m-dimensional system, the control algorithm is written as

$$p_{i+1} = L_C((\xi_i, \eta_i, \ldots), (\xi_{i+m}, \eta_{i+m}, \ldots)), \tag{10}$$

where L_C is a linear function. Such a function will always exist provided that the system is controllable and observable, i.e., $\lambda_j \neq \lambda_k$ for $j \neq k$, $\lambda_j \neq 1$ and $\alpha_j, t_j \neq 0$ for all j.

The sequence of m readings x and $m - 1$ perturbations p can be utilized in (8) to realize the final state in (10). It will not be apparent to the observer, however, that the system has reached that state until the mth iteration. It is therefore convenient to define the objective state in a form independent of the control perturbations $p_{i+1}, \ldots, p_m$. With this in mind, we consider two separate control problems: stabilizing unstable states and attaining a prescribed constant output. In each, the objective state is realized in a minimum number of steps.

With no external perturbations, stationary state behavior is characterized by the absence of motion, i.e., $x_{i+1} - x_i = 0$ and $p_i = 0$ for $i = 1, \ldots, m$. The difference between readings for consecutive steps in the two-variable system can be written by subtracting (6), (5) and (5), (4):

$$\begin{aligned} x_{i+1} - x_i &= (\lambda_\xi - 1)t_\xi \xi_i + (\lambda_\eta - 1)t_\eta \eta_i + A p_{i+1}, \\ x_{i+2} - x_{i+1} &= \lambda_\xi(\lambda_\xi - 1)t_\xi \xi_i + \lambda_\eta(\lambda_\eta - 1)t_\eta \eta_i \\ &\quad + (B - A)p_{i+1} + A p_{i+2}. \end{aligned} \tag{11}$$

It follows that the system state can be determined as a solution of (11) from the two differences in readings and two perturbations. For an m-dimensional system, the state

can be determined from m consecutive differences and m applied perturbations:

$$(\xi_{i+m}, \eta_{i+m}, \ldots) = L_S[(x_{i+m-1} - x_{i+m}), \ldots, (x_{i+2m} - x_{i+2m-1}); p_{i+m+1}, \ldots, p_{i+2m}]. \quad (12)$$

Equation (12) has a convenient form for defining a stationary state or fixed point since no other information is required for the corresponding position in phase space.

Combining (8) and (12) with (10) yields a general expression for the stabilization of unstable states in an m-dimensional system:

$$p_{i+1} = S[x_i, x_{i-1}, \ldots, x_{i-m+1}; p_i, p_{i-1}, \ldots, p_{i-m+2}; (x_{i+m+1} - x_{i-m}), \ldots, (x_{i+2m} - x_{i+2m-1}); p_{i+m-1}, \ldots, p_{i+2m}], \quad (13)$$

where S is the system invariant function. In the linear region, S can be identified from the time series of the randomly perturbed system by solving the associated set of linear equations with $4m$ unknown coefficients. We assume that Eq. (13) can be expanded into the nonlinear region with the system state determined by the coordinates on the curvilinear stable and unstable manifolds replacing the corresponding eigenvectors. Nonlinear terms can be incorporated through multivariable Fourier series expansion or by creating a nonlinear surface in $4m$-dimensional space using linear interpolation between nearest neighbors. Neural networks that are suited for fitting nonlinear functions can also be used to learn the S function on the basis of available data sets. Once constructed, the S function is a control invariant for a particular system that can be used to target unstable states from anywhere in phase space provided the perturbations do not exceed limits imposed by the system dynamics and that the function remains single valued. The convergence of the data points to a single-valued function provides a criterion for system controllability in the nonlinear sense. In some cases, however, the application of the S function is ambiguous; for example, three different steady states are present for $p = 0$ in the bistable region. Additional restrictions, such as limiting the range of the bifurcation parameter to single-valued regions can be imposed, or, alternatively, one can use the G function described below to target a particular state.

The process of stabilization is carried out as follows: The m delayed readings and $m - 1$ delayed perturbations that define the current state are substituted into the first set of terms in the S function [upper line of (13)]. The desired behavior yields zeros for the second set of terms in S. With these substitutions, the S function returns the first control perturbation. The second control perturbation is returned on the next iteration, and so on. After completion of the m-perturbation cycle, the system will reside very close to the objective state.

Unstable periodic orbits or stationary states can be tracked as a bifurcation parameter is slowly varied [16–18]. It may be desirable, however, for the system to reach some prescribed objective state rapidly. Thus we now consider how the system can be moved in m perturbations from any point to a desired point where the observable has a constant value g. It is not necessary to know the exact value of the bifurcation parameter at this point if the final state in (10) is defined by $p_{i+1} - p_i = 0$ and $x_i = g$ for $i = 1, \ldots, m$ and g corresponds to a state existing in the bifurcation diagram. It is possible to reconstruct the state of the two-dimensional system, for example, from three consecutive observations of x and one difference in p using (4), (5), and (6). In general, m-dimensional systems require $m + 1$ readings of x and $m - 1$ perturbation differences for the reconstruction:

$$(\xi_{i+m}, \eta_{i+m}, \ldots) = L_G[x_{i+m}, \ldots, x_{i+2m}; (p_{i+m+2} - p_{i+m+1}), \ldots, (p_{i+2m} - p_{i+2m-1})]. \quad (14)$$

The appropriate control surface G for driving the system output to some objective value is then constructed by combining (8), (10), and (14):

$$p_{i+1} = G[x_i, x_{i-1}, \ldots, x_{i-m+1}; p_i, p_{i-1}, \ldots, p_{i-m+2}; x_{i+m}, \ldots, x_{i+2m}; (p_{i+m+2} - p_{i-m+1}), \ldots, (p_{i+2m} - p_{i+2m-1})]. \quad (15)$$

The G function can be identified from the system response in a fashion similar to the S function identification. The control perturbation is returned by the G function when the second set of terms [middle line of (15)] yields $x_{i+m}, \ldots, x_{i+2m} = g$ and the perturbation differences are set to zero. The effective system dimension m is usually not known in advance. Following methods developed for linear control [13], different values of m can be used for creating the control surface and the fitting error is then evaluated. The value of m that yields the minimum error is selected for control.

We now demonstrate stationary state stabilization and targeting objective states with the two-variable Gray-Scott model, where the parameter $\kappa_2 = \frac{1}{40}$. The model exhibits a Hopf bifurcation at $1/T_{\text{res}} = 0.0049$. Changes in $1/T_{\text{res}}$ from 0.0049 to 0.00508 and back again move the system from one value of the stationary state to another, as shown in Fig. 3. The oscillatory transients exhibited by the autonomous system arise from the slowing down in the vicinity of the Hopf bifurcation. The solid line shows the tracking obtained by use of the G function. The linear version of the algorithm works well in this region since the variations are small. As shown in Fig. 3, only two iterations are necessary to move the system between the two stationary state values.

The autonomous Gray-Scott system displays nonlinear relaxation oscillations with $1/T_{\text{res}} = 0.0037$. The seven-dimensional nonlinear S and G surfaces were obtained for these conditions by applying 1000 random perturbations to the system parameter $1/T_{\text{res}}$. Each surface was constructed using linear interpolation from 8 neighboring data

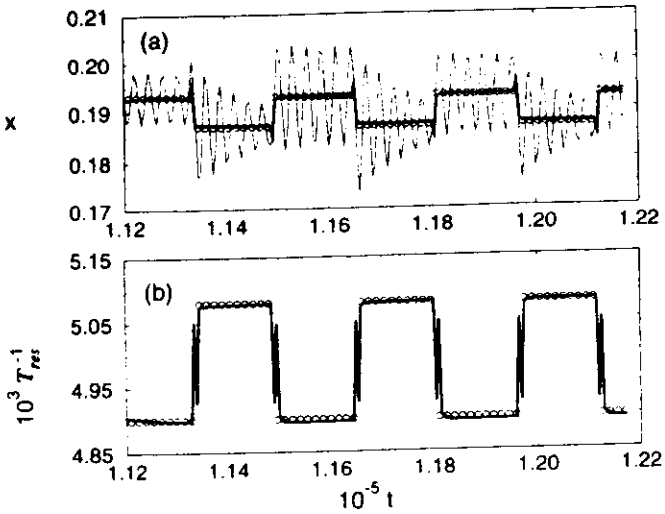

FIG. 3. (a) Response of autonomous (———) and controlled (▬▬) two-dimensional Gray-Scott model when changes in the control parameter move the system between two stationary state values (ooooooo), where $x = \alpha$ in Eq. (1); (b) corresponding variations of $p = 1/T_{res}$.

points in the phase space. The system converges to the stationary state upon activation of the control algorithm. The convergence rate is initially slow, however, due to the sparseness of the control surface and the restriction imposed by the system dynamics on the perturbation size. As the system converges, the new data are used to refine the shape of the S surface in the vicinity of the stationary state. The same procedure was used to create and refine the G function. Figure 4 shows an application of the S function to suppress the oscillations of the autonomous system and to stabilize the unstable stationary state. The S function was replaced by the G function at $t = 14\,500$ to alter the system output between the values of 0.2 and 0.3. Only two

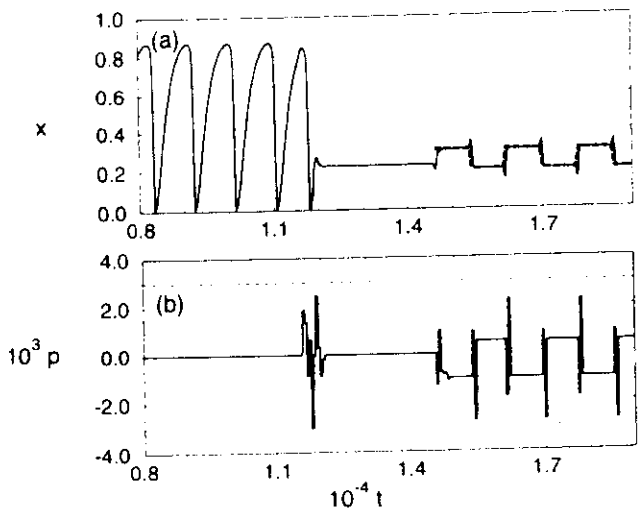

FIG. 4. (a) Stationary state stabilization and targeting objective states using seven-dimensional control surfaces S and G. Broken line shows the objective states. (b) Applied perturbations, where dashed lines show the maximum allowed perturbation.

iterations are required to move the system between these values of the unstable state.

The algorithms proposed here can readily be extended to include multiple observation and control channels by using a vector form of the S or G functions. Because the control laws are constructed directly from the time series, they are robust and convenient to implement in experimental settings. The number of unknown parameters for the control surface identification is generally higher than in the case of linear system identification and may therefore require larger data sets. The learning stage can be significantly decreased, however, by refining the control surface adaptively in the process of control. Because the control problem is formulated in terms of an invariant function, many well-developed techniques for prediction from nonlinear time series [19] can be used with the control algorithm.

We thank the National Science Foundation (Grant No. CHE-9531515), the Office of Naval Research (Grant No. N00014-95-1-0247), and the Petroleum Research Fund (Grant No. 29565-AC6) for supporting this research.

*To whom correspondence should be addressed.

[1] E. Ott, C. Grebogi, and J. A. Yorke, Phys. Rev. Lett. **64**, 1196 (1990).
[2] W. L. Ditto, S. N. Rauseo, and M. L. Spano, Phys. Rev. Lett. **65**, 3211 (1990).
[3] E. R. Hunt, Phys. Rev. Lett. **67**, 1953 (1991).
[4] T. Carroll, I. Triandaf, I. B. Schwartz, and L. Pecora, Phys. Rev. A **46**, 6189 (1992).
[5] R. Roy, T. W. Murphy, T. D. Maier, Z. Gills, and E. R. Hunt, Phys. Rev. Lett. **68**, 1259 (1992).
[6] S. Bielawski, D. Derozeir, and P. Glorieux, Phys. Rev. A **47**, R2492 (1993).
[7] V. Petrov, V. Gáspár, J. Masere, and K. Showalter, Nature (London) **361**, 240 (1993).
[8] P. Parmananda, P. Sherard, R. W. Rollins, and H. D. Dewald, Phys. Rev. E **47**, R3003 (1993).
[9] A. Garfinkel, M. L. Spano, W. L. Ditto, and J. N. Weiss, Science **257**, 1230 (1992).
[10] S. J. Schiff, K. Jerger, D. H. Duong, T. Chang, M. L. Spano, and W. L. Ditto, Nature (London) **370**, 615 (1994).
[11] T. Shinbrot, C. Grebogi, E. Ott, and J. A. Yorke, Nature (London) **363**, 411 (1993).
[12] P. So and E. Ott, Phys. Rev. E **51**, 2955 (1995).
[13] V. Petrov, E. Mihaliuk, S. K. Scott, and K. Showalter, Phys. Rev. E **51**, 3988 (1995).
[14] V. Petrov, S. Metens, P. Borckmans, G. Dewel, and K. Showalter, Phys. Rev. Lett. **75**, 2895 (1995).
[15] P. Gray and S. K. Scott, Chem. Eng. Sci. **39**, 1087 (1984).
[16] Z. Gills, C. Iwata, R. Roy, I. B. Schwartz, and I. Triandaf, Phys. Rev. Lett. **69**, 3169 (1992).
[17] V. Petrov, M. F. Crowley, and K. Showalter, Phys. Rev. Lett. **72**, 2955 (1994).
[18] V. In, W. L. Ditto, and M. L. Spano, Phys. Rev. E **51**, R2689 (1995).
[19] H. D. I. Abarbanel, R. Brown, J. J. Sidorowich, and L. S. Tsimring, Rev. Mod. Phys. **65**, 1331 (1993).

Reprint Series
10 February 1995, Volume 267, pp. 868–871

SCIENCE

Navigating Complex Labyrinths: Optimal Paths from Chemical Waves

Oliver Steinbock, Ágota Tóth, and Kenneth Showalter*

Navigating Complex Labyrinths: Optimal Paths from Chemical Waves

Oliver Steinbock, Ágota Tóth, Kenneth Showalter*

The properties of excitable media are exploited to find minimum-length paths in complex labyrinths. Optimal pathways are experimentally determined by the collection of time-lapse position information on chemical waves propagating through mazes prepared with the Belousov-Zhabotinsky reaction. The corresponding velocity fields provide maps of optimal paths from every point in an image grid to a particular target point. Collisions of waves that were temporarily separated by obstacles mark boundary lines between significantly different paths with the same absolute distance. The pathfinding algorithm is tested in very complex mazes with a simple reaction-diffusion model.

Propagating waves in spatially distributed, excitable media arise from the coupling of a positive feedback process with some form of transport, for example, autocatalytic chemical reaction with molecular diffusion (*1*). Such waves are observed in biological (*2*), chemical (*3*), and physicochemical (*4*) systems and typically exhibit constant velocities and annihilation in collisions with boundaries or other waves (*5*, *6*). In this report we describe how these features give rise to a highly efficient algorithm for the determination of optimal paths. Conventional pathfinding methods typically rely on iterative searches, in which all possible pathways between a point of interest and a target point are successively determined and the optimal path is then selected (*7*). In an excitable medium, a single propagating wave generates a map for the optimal path from every point of the system to a target point. This feature was first noted by Sepulchre *et al.* (*8*) in a computational study of wave propagation in an oscillatory medium containing impenetrable obstacles.

Experimental studies of wave propagation in complex labyrinths were carried out with the excitable Belousov-Zhabotinsky (BZ) reaction (*9*) by means of time-lapse digital imaging techniques. Planar labyrinths were made of vinyl-acrylic membranes saturated with BZ reaction mixture (*10*). We prepared impenetrable barriers by carefully cutting out rectangular regions of the membrane. This simple procedure allowed the realization of a variety of geometries and provided an effectively two-dimensional system without hydrodynamic disturbances. The composition of the BZ solution was prepared so that no spontaneous wave initiations occurred; however, waves could be reproducibly initiated by allowing a silver wire to contact the reagent-loaded membrane. The wave propagation was monitored by image analysis of monochromatic light (wavelength $\lambda = 500$ nm) reflected from the medium. The video signals were recorded and then digitized into image sequences (*11*), which were enhanced with standard imaging routines and analyzed.

Figure 1A shows a 50-frame composite image of a chemical wave propagating through a BZ-membrane labyrinth. The wave splits at each junction during its propagation and therefore reaches all points in the maze that are connected to the starting point (at the lower left corner). Wave segments that propagate into blind channels ultimately vanish on collision with the boundaries. Each snapshot shows waves at an equal distance from their positions in the previous snapshot, given by the product of the constant velocity (2.41 ± 0.18 mm/min) and the time between each two snapshots (50 s). To a good approximation, waves propagate according to Huygens's principle, where the front advances a fixed distance per unit of time in a direction normal to the front. The effects of curvature on the wave velocity (*12*), to be discussed below, are slight for mazes with sufficiently large length scales as considered here.

Image sequences with higher temporal resolution allow the generation of maps that give the path length from any location in the maze to a given target point, within the resolution of the composite image. Figure 1B shows a color-coded distance map based on higher resolution data, where the colors are keyed to the elapsed time from the wave initiation to the local maximum of excitation at each point. The minimum path length from any point in the maze to the target point S is given by the product of the elapsed time assigned to that point and the constant wave velocity. The optimal transit time and distance for every location in the labyrinth are determined by a single propagating wave, representing a highly efficient accumulation of information in a parallel manner.

The space-time information compiled in Fig. 1B provides the basis for a determination of detailed minimum-length paths. The optimal path from any arbitrary point to the target point is easily determined according to the velocity field, which is generated by specifying the direction of wave propagation at each point in the grid. The vector field derived from Fig. 1B is shown in Fig. 1C, along with several examples of optimal paths. One can compute the specific shortest path connections from the time-indexed points of the composite image by searching for the nearest point indexed $t - \tau$, where t is the elapsed time from the wave initiation to the current position and τ is the time increment between successive images.

Figure 1C shows that the path optimization includes local features such as diagonal trajectories in the corridors of the labyrinth. The labyrinth is therefore analyzed as a two-dimensional array of rectangular segments rather than as a mesh of one-dimensional strings. Path boundaries, created by colliding waves that previously had been separated by barriers, are also defined (see Fig. 1B). These boundaries demarcate significantly different pathways of equal distance to the target point S. The maze is consequently divided into local domains that correspond to families of pathways, where paths in one domain are matched by different paths of equal length in another domain.

Distinct basins of attraction arise from the synchronous initiation of several waves at different locations in a maze. In contrast to experiments with a single initiation, two different types of annihilation loci occur: path boundaries from waves originating at a single initiation point and collision boundaries from waves originating at different initiation points. The latter represent boundaries composed of points that are equidistant to two initiation sites; the intersection of three or more boundaries defines points equidistant to each of the corresponding initiation sites. Both types of boundaries are shown in Fig. 2, in which four waves were initiated almost synchronously at sites S1, S2, S3, and S4 near the corners of the maze.

The basin of attraction associated with each initiation site is shown by a single color in Fig. 2, where the intensity is indexed to the elapsed time from the wave initiation. Each color boundary represents a separatrix between two basins. In terms of a potential surface description, the minimum of each basin lies at the wave initiation point and the height at any point on the surrounding surface is proportional to the elapsed time assigned to that point. Each separatrix is defined by the locus of collision times and represents a "watershed" separating trajectories that lead to different target points.

Department of Chemistry, West Virginia University, Morgantown, WV 26506, USA.

*To whom correspondence should be addressed.

Examples of shortest distance paths are also shown in Fig. 2, computed by tracking nearest $t - \tau$ points as described above. Four initial points chosen near the intersection of the S1, S2, and S3 basins at $(x, y) = (14\ \text{mm}, 16\ \text{mm})$ lead to three different target points with two significantly different paths to S2. Three other paths are also shown, with initial points chosen to be near a path boundary and a basin separatrix.

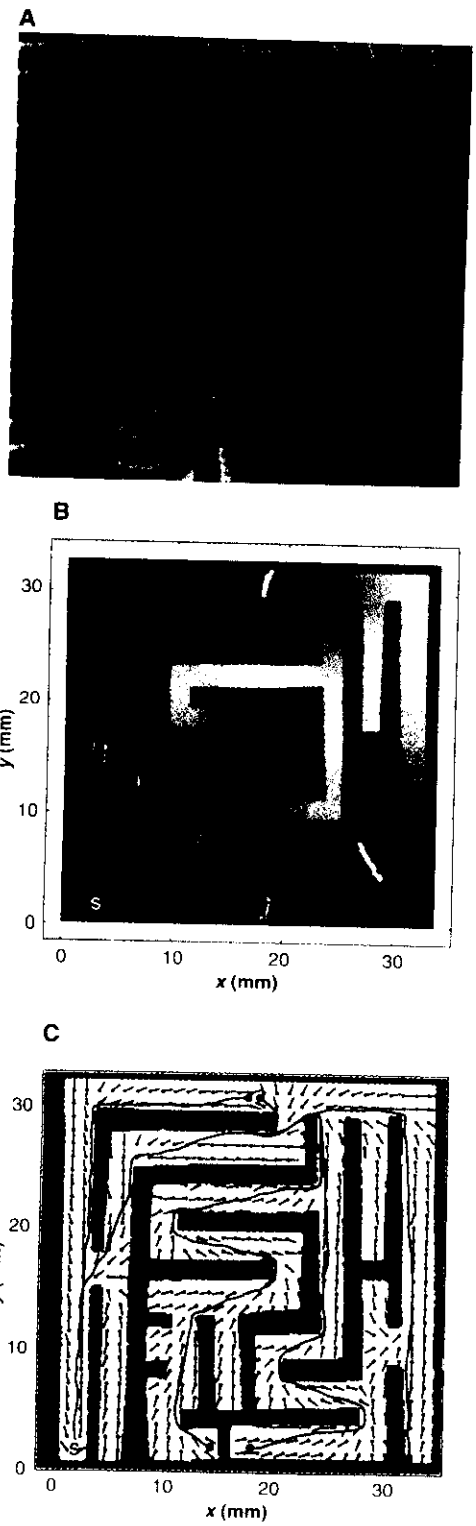

While propagating chemical waves provide vivid examples of path optimization in excitable media, computational simulations of such waves allow the approach to be demonstrated in very complex labyrinths. We use a generic model for excitable media, the two-variable Barkley model (*13*), which has the form

$$\frac{\partial u}{\partial t} = \nabla^2 u + f(u, v) \quad (1)$$

$$\frac{\partial v}{\partial t} = g(u, v) \quad (2)$$

where the variables u and v describe the spatiotemporal dynamics of a propagator species and a controller species, respectively (*14*).

Figure 3 shows the results of simulated wave propagation through a complex labyrinth that was developed in 1664 by G. A. Boeckler (*15*). As in the experiments, the color coding corresponds to transit times for the shortest length path from any point to the target point, the red door at the top boundary where the wave was initiated. The color map shows very different transit times for points in each of the four square areas and the central circular area. The map indicates times only for the optimal paths (in fact, there are multiple paths from any particular starting point to the target point). An example of an optimal path originating from the lower left square (colored blue) is shown by the white dashed line. This trajectory was computed from the time-indexed points according to the procedure described above. Visual inspection of the labyrinth reveals another, significantly different pathway, which exceeds the optimal path in length by only 7%. We also carried out an additional calculation to prove that the optimal, shortest length path is unaffected by switching the point of origin with the target point and vice versa. The optimal path obtained from this "reverse" calculation is the same as that shown in Fig. 3.

Throughout this report we have assumed constant-velocity waves propagating according to Huygens's principle. This assumption is the basis of the vector fields derived from the time-indexed grids and the $t - \tau$ algorithm for determining optimal paths. In fact, front curvature may significantly affect the velocity of wave propagation (*12*). The error introduced by neglecting curvature effects is small in the optimal

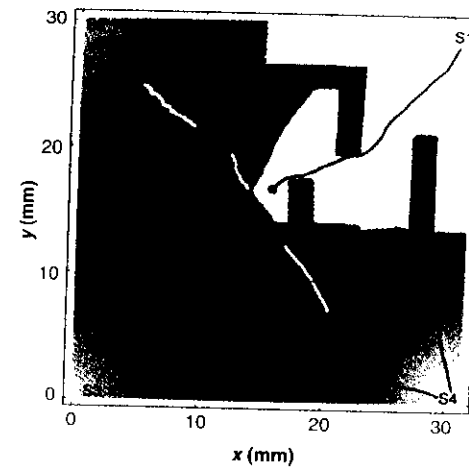

Fig. 2. Color map showing a BZ membrane labyrinth in which four waves were initiated almost synchronously (~5-s intervals) at S1, S2, S3, and S4. The area covered by each wave is distinguished by a different color, with the color intensity at any point proportional to the time elapsed since wave initiation. Obstacles are plotted in black, and the shortest paths between seven points and various target points are shown in red. The total duration of the experiment was ~450 s.

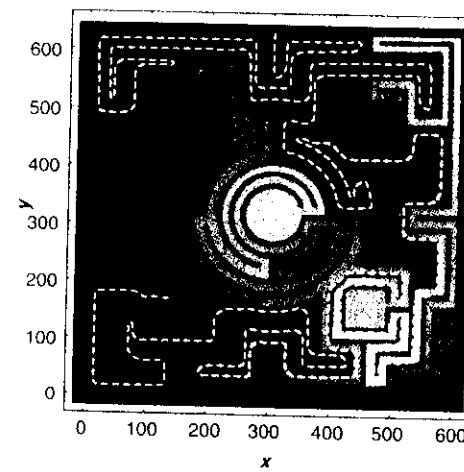

Fig. 3. Interrogation of a complex labyrinth by wave propagation in the Barkley model (*13, 14*). Colors indicate propagation times for a wave that was initiated at the entrance, shown in red at the top boundary of the maze. The color coding is the same as in Fig. 1 over a total elapsed (dimensionless) time of 1174.15. The dashed white line shows the shortest path from the lower left square region (blue) to the maze entrance (red).

Fig. 1. (**A**) Chemical wave propagating through a BZ membrane labyrinth. A sequence of 50 images obtained at 50-s intervals was superimposed to form the composite image. The wave was initiated in the lower left corner of the maze. The total area of the maze is 3.2 cm by 3.2 cm, with obstacles appearing as black rectangular segments. (**B**) Color map representing the time difference between wave initiation and local excitation for all points in the labyrinth. A sequence of 250 images obtained at 10-s intervals was used to form the time-indexed composite image (yielding a spacing of ~ 4 pixels between successive front positions). Red, green, yellow, and blue correspond to successively longer times over the total elapsed time of 2500 s. White lines show path boundaries. (**C**) Velocity field describing the local wave propagation direction. Small black dots represent the origins of vectors. The shortest paths between five points and the target point S are shown in red.

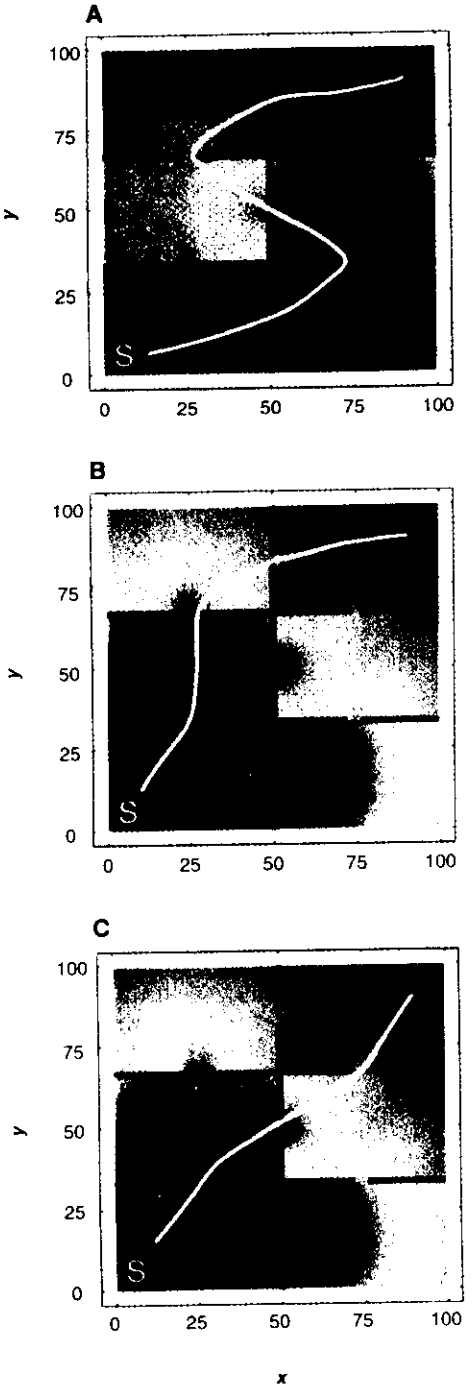

Fig. 4. Interrogation of "door size" in a labyrinth with narrow passages between barriers by wave propagation in the Barkley model (*13, 14*). Distance map and optimal trajectory (white) generated by medium with low excitability, $a = 0.50$, $r_c = 1.125$ (**A**); intermediate excitability, $a = 0.70$, $r_c = 0.825$ (**B**); high excitability, $a = 0.85$, $r_c = 0.675$ (**C**). The color coding is the same as in Fig. 1 over a total elapsed (dimensionless) time of 24.15 (A), 15.83 (B), and 14.60 (C). Door sizes [r = channel radius, (x, y) = maze coordinates]: $r = 1.35$, $(x, y) = (50, 16.5)$; $r = 1.05$, $(x, y) = (25, 33)$; $r = 1.35$, $(x, y) = (75, 33)$; $r = 1.35$, $(x, y) = (50, 50)$; $r = 1.35$, $(x, y) = (25, 66)$; $r = 0.75$, $(x, y) = (75, 66)$; $r = 1.35$, $(x, y) = (50, 83.5)$. The integration was carried out on a grid of 300 points by 300 points (grid spacing $\Delta x = 0.33$, time step $\Delta t = 0.0056$) with the parameters $b = 0.01$, $\epsilon = 0.02$, and a indicated above.

paths above; however, errors in the transit times may become significant in mazes with smaller length scales.

Curvature effects considered in a general context can be exploited to extend the pathfinding capabilities of excitable media. The dependence of wave velocity on curvature allows the determination of "door size" in complex labyrinths with narrow gaps between barriers. The velocity depends on front curvature according to an eikonal relation (*12*): $c = c_0 + D\kappa$, where c is the normal wave velocity, c_0 is the planar wave velocity, D is the diffusion coefficient of the autocatalyst, and κ is the curvature of the front. For convex waves ($\kappa < 0$), such as those exiting narrow channels, the propagation velocity is reduced by the enhanced dispersion of the autocatalyst. A critical nucleation size with a radius of curvature ($r = 1/|\kappa|$) given by $r_c = D/c_0$ is predicted when the normal velocity is reduced to zero. Thus, as c_0 is decreased, r_c increases and channels with radii below r_c do not allow waves to pass. Recent experiments with BZ waves propagating through microcapillary tubes have demonstrated this behavior (*16*).

Figure 4 shows a labyrinth in which waves calculated with the Barkley model were used to determine the relative channel widths between obstacles. Color maps generated from low-, medium-, and high-velocity waves are shown in Fig. 4, A through C, respectively. For the slowest wave (Fig. 4A), all but two channels have $r > r_c$. Because two of the "doors" are too small, the optimal trajectory from the starting point in the upper right corner to the target point S takes a circuitous route through the "allowed" openings. Above a critical velocity, the opening at $(x, y) = (25, 33)$ becomes available for wave propagation (because $r > r_c$) and a more direct path to the target point S is determined (Fig. 4B). For the fastest wave, the opening at $(x, y) = (75, 66)$ allows wave propagation and a nearly diagonal pathway is determined (Fig. 4C). Thus, optimal paths are determined even when some openings are too small, and the sizes of the openings can be found by variation of wave propagation velocity.

Propagating waves in excitable media provide an interesting, and potentially useful, alternative to traditional iterative-search methods for determining optimal paths. A relatively simple analysis provides optimal paths from every point in a grid to a target point. Thus, a robot in a large warehouse could readily use such a map at any point without needing to recompute its trajectory at each new location to deliver a parcel to loading dock S. The method can easily accommodate changing labyrinths as well, provided that the time scale for the changes is longer than the time required for recomputing the vector field. In addition, the method automatically discerns which doors are wide enough for the parcel, providing an optimal trajectory that ignores any doors that are too small.

While the computational implementation of the reaction-diffusion algorithm provides intriguing possibilities for practical applications, the experimental results point to possible mechanisms for optimization in biological systems. Neural pathways, for example, are known to be extremely complex, yet highly efficient (*17*). Could path optimization in networks of neurons rely on the properties of excitable media, as suggested in the optimal path determinations presented here? This intriguing possibility provides, in itself, ample reason to develop an understanding of optimization capabilities of excitable media. We believe that the experimental approach could also be transferred to microscopic reaction-diffusion systems, such as the oxidation of carbon monoxide on platinum (*4*). Waves interacting with complex boundaries created by photolithography have been recently studied with the use of this system (*18*), suggesting that path optimization could be readily implemented on a microscopic scale.

REFERENCES AND NOTES

1. A. T. Winfree, *The Geometry of Biological Time* (Springer, Berlin, 1980); J. Ross, S. C. Müller, C. Vidal, *Science* **240**, 460 (1988).
2. J. M. Davidenko, A. M. Pertsov, R. Salomonsz, W. Baxter, J. Jalife, *Nature* **355**, 349 (1992); A. Gorelova and J. Bures, *J. Neurobiol.* **14**, 353 (1983); J. Lechleiter, S. Girard, E. Peralta, D. Clapham, *Science* **252**, 123 (1991).
3. R. J. Field and M. Burger, Eds., *Oscillations and Traveling Waves in Chemical Systems* (Wiley, New York, 1985); A. T. Winfree, *Science* **175**, 634 (1972).
4. H. H. Rotermund, S. Jakubith, A. von Oertzen, G. Ertl, *Phys. Rev. Lett.* **66**, 3083 (1991).
5. A. S. Mikhailov, *Foundation of Synergetics I: Distributed Active Systems* (Springer, Berlin, 1990).
6. Reflection of waves colliding with no-flux boundaries and with other waves has been recently reported in a model reaction-diffusion system [W. N. Reynolds, J. E. Pearson, S. Ponce-Dawson, *Phys. Rev. Lett.* **72**, 2797 (1994); V. Petrov, S. K. Scott, K. Showalter, *Philos. Trans. R. Soc. London Ser. A* **443**, 631 (1994)].
7. P. A. Steenbrink, *Optimization of Transport Networks* (Wiley, London, 1974); R. Gould, *Graph Theory* (Benjamin-Cummings, Menlo Park, CA, 1988); J. Malkevitch and W. Meyer, *Graphs, Models, and Finite Mathematics* (Prentice-Hall, Englewood Cliffs, NJ, 1974).
8. J. A. Sepulchre, A. Babloyantz, L. Steels, in *Proceedings of the International Conference on Artificial Neural Networks*, T. Kohonen, K. Makisara, O. Simula, J. Kangas, Eds. (Elsevier, Amsterdam, 1991), pp. 1265–1268.
9. A. N. Zaikin and A. M. Zhabotinsky, *Nature* **225**, 535 (1970).
10. Cut membranes (Gelman Metricel, thickness, 140 μm; pore size, 0.45 μm) were soaked with BZ solution and covered with silicone oil in a thermostated petri dish maintained at 25.0° ± 0.2°C. Initial reagent concentrations were as follows: $[NaBrO_3] = 0.2$ M, $[H_2SO_4] = 0.4$ M, [malonic acid] = 0.17 M, [NaBr] = 0.1 M, [ferroin] = 1.0 mM.
11. S. C. Müller, Th. Plesser, B. Hess, *Physica D* **24**, 71 (1987).
12. J. J. Tyson and J. P. Keener, *ibid.* **32**, 327 (1988); V.

S. Zykov, *Biophysics* **25**, 906 (1980).
13. D. Barkley, *Physica D* **49**, 61 (1991).
14. The functions f and g are defined as $f(u, v) = (1/\epsilon)u(1 - u)[u - (v + b)/a]$ and $g(u, v) = u - v$. The parameter values $a = 0.9$, $b = 0.05$, and $\epsilon = 0.02$ were chosen to model an excitable system. The equations were integrated on a grid of 480 points by 480 points (grid spacing $\Delta x = 1.3$, time step $\Delta t = 0.085$) with the Laplacian operator ∇^2 approximated by a standard nine-point formula. (The same optimal path was found in a higher resolution calculation with grid spacing $\Delta x = 0.65$ and time step $\Delta t = 0.011$.) We were able to realize different complex labyrinths by digitizing corresponding line drawings and modeling the borders and obstacles as regions with constant, steady-state values of u and v. These boundary conditions correspond to "sink" boundaries and reflect the experimental system, where all edges of the membrane were in contact with silicone oil.
15. W. H. Matthews, *Mazes and Labyrinths* (Longmans, London, 1922).
16. Á. Tóth, V. Gáspár, K. Showalter, *J. Phys. Chem.* **98**, 522 (1994).
17. E. R. Kandel, J. H. Schwartz, T. M. Jessell, *Principles of Neural Science* (Elsevier, New York, ed. 3, 1991).
18. M. D. Graham *et al.*, *Science* **264**, 80 (1994).
19. This research was supported by the National Science Foundation (grant CHE-9222616). We acknowledge the donors of the Petroleum Research Fund, administered by the American Chemical Society, for partial support of this research.

26 August 1994; accepted 10 November 1994

Reprint Series
29 September 1995, Volume 269, pp. 1857–1860

SCIENCE

Anisotropy and Spiral Organizing Centers in Patterned Excitable Media

Oliver Steinbock, Petteri Kettunen, and Kenneth Showalter*

Anisotropy and Spiral Organizing Centers in Patterned Excitable Media

Oliver Steinbock, Petteri Kettunen, Kenneth Showalter*

Chemical wave behavior in a patterned Belousov-Zhabotinsky system prepared by printing the catalyst of the reaction on membranes with an ink jet printer is described. Cellular inhomogeneities give rise to global anisotropy in wave propagation, with specific local patterns resulting in hexagonal, diamond, and pentagonal geometries. Spiral wave sources appear spontaneously and serve as organizing centers of the surrounding wave activity. The experimental methodology offers flexibility for studies of excitable media with made-to-order spatial inhomogeneities.

Propagating waves are observed in living organisms and biological tissues (*1*) as well as excitable chemical systems (*2*). The familiar rotating spiral waves and expanding target patterns of the Belousov-Zhabotinsky (BZ) reaction (*3*) are also observed in thin slices of heart tissue (*4*), in the cytoplasm of frog oocytes (*5*), and in animal retinas (*6*). Three-dimensional scroll waves, extensively studied in the BZ reaction (*7*), have now been characterized in migrating slugs of the slime mold *Dictyostelium discoideum* (*8*), and it is likely that these waves are precursors to ventricular fibrillation in mammals (*9*). The cellular nature of living systems, however, gives rise to inhomogeneities and anisotropy not present in homogeneous reaction systems, and these may play an important role in the behavior of biological media. A crucial example is found in the anisotropy of mammalian heart muscle (*10*). The cellular structure of cardiac tissue not only causes local variations in wave velocity (*4*) but also gives rise to propagation failure (*11*). In this report, we describe wave behavior in excitable media with well-defined cellular inhomogeneities obtained by printing catalyst patterns on a BZ-membrane system. Our experimental and numerical investigations show that local patterns determine the global wave geometry and give rise to spontaneous organizing centers.

Noszticzius and co-workers (*12*) have recently demonstrated that bathoferroin, a catalyst and indicator for the BZ reaction (*13*), is effectively immobilized on polysulphone membranes. Our experimental method is based on the precision loading of this catalyst onto the membranes with an ink jet printer (*14*). Patterns were generated as black and white images by a commercial graphics program, which were then printed with the catalyst solution on the polysulphone membranes. Following Noszticzius (*12*), the ready-to-use membranes were

Department of Chemistry, West Virginia University, Morgantown, WV 26506-6045, USA.

*To whom correspondence should be addressed.

placed on agarose gels containing BZ solution (*15*), which provided a continuous supply of reactants to the catalyst-loaded regions without hydrodynamic disturbances of the wave activity. The wave behavior was monitored by measuring the reflected light (wavelength λ = 500 nm) from the medium with a charge-coupled device (CCD) video camera.

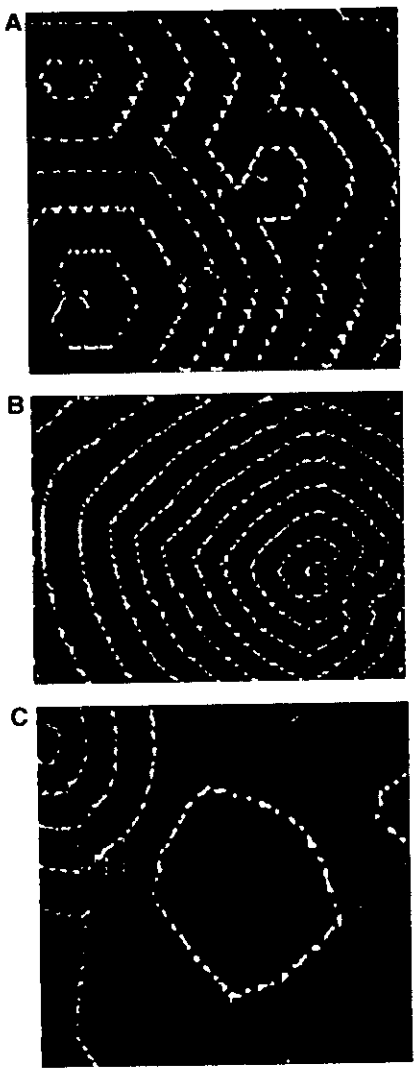

Fig. 1. Propagating waves on BZ membranes with cellular inhomogeneities. Catalyst patterns appear as the background in each figure; unloaded and loaded regions are light and dark gray, respectively: (**A**) Triangular cells of side length 1.65 mm; (**B**) superimposed linear and circular grids (~1 vertical line per millimeter; the radius of vertically shifted circle segments is ~4 cm); (**C**) superimposed circular grids (radius of circle segments is ~2.1 cm with a horizontal and vertical shift of ~1 curve/mm). The specific catalyst patterns gave rise to (A) hexagonal, (B) diamond-shaped, and (C) pentagonal wave patterns. Image areas are (A) 14.5 cm^2, (B) 13.5 cm^2, and (C) 8.4 cm^2. Line thickness in (B) and (C) was 0.33 mm. The positions of the waves, obtained by subtraction of successive video frames, were superimposed on the background image, with white assigned to the wave front and black assigned to the wave back. Spiral waves in (A) and (B) occurred spontaneously, whereas the wave in (C) was initiated by contacting the membrane with a silver wire.

Wave propagation was studied on various catalyst-loaded membranes, each printed with a different pattern. A checkerboard arrangement of triangular cells gave rise to hexagonal wave geometry (Fig. 1A). Similarly, diamond-shaped wave structures developed on cross-hatched linear grids, and deformations of higher complexity occurred on less symmetrical patterns. A nonlinear catalyst grid of superimposed parallel lines and vertically shifted circle segments (Fig. 1B) gave rise to a distorted diamond geometry with the left corner following a specific arc. Video frame sequences demonstrated that the spiral tips in Fig. 1, A and B, rotated around particular catalyst-free cells on the membrane, effectively pinning the spiral waves. A similar pinning of spiral waves in heart tissue to anatomical discontinuities such as small arteries has been reported (*4*).

Wave patterns with approximately fivefold symmetry may occur in catalyst grids consisting of superimposed arrays of shifted circular arcs (Fig. 1C). The pentagonal shape has four prominent corners that coincide with two catalyst-loaded arcs. The intersection of these arcs is close to the point of wave initiation. The fifth, somewhat smoother corner is directed along the unique symmetry axis of the catalyst pattern (toward the upper right).

We carried out numerical simulations of the wave behavior using the Tyson-Fife model (*16*, *17*) of the BZ reaction, modified to reflect the features of the patterned medium. The model has the form

$$\frac{\partial u}{\partial t} = \nabla^2 u + f(u, v) \qquad (1)$$

$$\frac{\partial v}{\partial t} = g(u, v) \qquad (2)$$

where the variables u and v describe the scaled concentrations of the propagator species $HBrO_2$ and the controller species bathoferriin, respectively. Catalyst-free regions on the membrane were modeled by omitting the equation for v and all terms in $f(u, v)$ that involve the catalyst (*17*). This allows the propagator species u to penetrate catalyst-free regions even though these areas do not support active wave propagation.

While the experimental measurements yield information about the wave propagation based on the bathoferriin concentration, the numerical simulations can provide insights in terms of the autocatalytic species $HBrO_2$. A grid of triangular cells (Fig. 2A) gives rise to a hexagonal wave pattern much like the experimentally measured waves (Fig. 1A). As in the experiment, the rotating spiral tips are pinned to specific catalyst-free cells. The pentagonal wave arising from a grid of superimposed arrays of shifted circular arcs (Fig. 2B) is also in good agreement with the corresponding experimental wave pattern (Fig. 1C). Elevated levels of u appear in catalyst-free cells behind the waves in both simulations (Fig. 2). These islands of autocatalyst are not able to initiate additional waves, however, because they are surrounded by catalyst-loaded cells in the refractory state (*18*). It is possible that such regions of elevated u are relevant to the appearance of "echo waves" in the trailing edge of a wave, a phenomenon observed in heart tissue (*19*).

The wave patterns in Figs. 1 and 2 can be understood in terms of a simple geometric mechanism. Assuming the catalyst-free cells to be impenetrable obstacles, the geometries

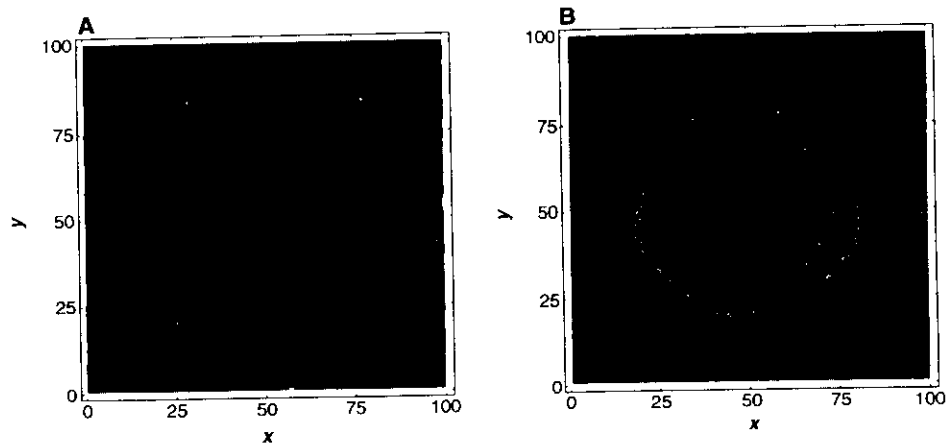

Fig. 2. Two-dimensional simulations of wave patterns. Black and gray areas indicate catalyst-loaded and catalyst-free regions, respectively. Superimposed white curves represent contour lines of the variable u at a given time. (**A**) Spiral pair forming hexagonal pattern (contour line at half-maximum of the propagator variable, $u_{max}/2$); (**B**) wave with pentagonal deformation (contour lines at $u_{max}/3$ and $2u_{max}/3$). Equations were integrated on a grid of 300 × 300 points (grid spacing Δx = 1/3; time step Δt = 0.001) with f = 2.5 for excitable kinetics (*17*).

can be deduced by determining paths along the catalyst-loaded cells of equal distance from the wave origin. Waves propagating along continuous lines of the catalyst grid therefore form corners of the pattern, and the most circuitous routes form the least advanced edges. In addition, the diffusion of $HBrO_2$ into the catalyst-free cells and its flux into neighboring catalyst-loaded cells provide a mechanism for wave transmission across the barriers. In experiments with catalyst-loaded squares separated by catalyst-free strips, continuous wave patterns formed across the array despite the unexcitable barriers (*20*). The extent of wave transmission across the catalyst-free regions depended on excitability and barrier width, with the corresponding wave geometries ranging from sharply polygonal to the familiar circles and spirals of homogeneous media.

Experiments were carried out to examine wave behavior in media containing random heterogeneities (Fig. 3A). Patterns were printed with a catalyst dot density linearly increasing from 0.1 to 1.0. The dot density was equally incremented each printed line for 300 lines, with the dots in each line placed according to a random number generator. The random heterogeneities were on a much finer scale than the patterns described above because they occurred dot-wise, close to the resolution of the printer. On the left side of the membrane (Fig. 3A), the dot density is insufficient to support wave activity. Irregular waves are exhibited between a density of about 0.3 and 0.5, below which only fleeting spots of excitation are found. The waves become regular at a dot density greater than about 0.6. Qualitatively similar behavior was found with reactant solutions of lower excitability (containing a lower sulfuric acid concentration), where the transition from irregular to regular behavior occurred at higher dot density. The wave segments in regions of intermediate dot density tended to serve as high-frequency sources, eventually entraining the behavior in the higher density regions. This entrainment resulted in overall wave propagation from regions of low dot density to high dot density (from left to right in Fig. 3).

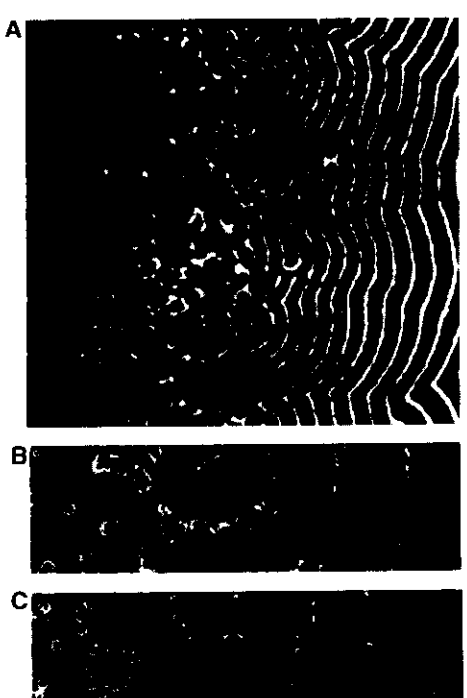

Fig. 3. Chemical waves on a linear dot density gradient with random dot locations perpendicular to the gradient. (**A**) Wave behavior on catalyst-loaded membrane; wave positions (white) obtained by image subtraction (Δt = 6 s). The density of catalyst-loaded dots varies from 0.1 (left) to 1.0 (right); field of view, 9.7 cm^2. (**B** and **C**) Numerical simulations of wave behavior: two successive images with Δt = 2. Wave patterns, indicated by white contour lines of the variable u (as in Fig. 2B), evolved slowly from uniform initial conditions. Dot density varies linearly from 0.1 (left) to 0.9 (right). Parameters of simulation: 600 × 150 grid points, grid spacing Δx = 1/3, time step Δt = 0.001, and ϵ = 1.25 for oscillatory kinetics (*17*).

Figure 3, B and C, shows successive images of the simulated behavior, with regions of elevated u within the contour curves (*21*). At very low dot density, regions of excitation appear but are ineffective in initiating waves. At an intermediate dot density between 0.3 and 0.4, larger regions of excitation form broken wave segments that serve as wave sources as they undergo spiral-like rotation. Waves also emanate from symmetrical pacemakers in this region. The waves become regular as they move into regions of higher dot density. While the intermediate level heterogeneity gives rise to organizing wave centers, the waves in regions of higher dot density are remarkably unaffected by the heterogeneity.

Spiral waves do not occur spontaneously in homogeneous media. In homogeneous BZ systems, they form at either physically or chemically induced wave breaks (*1*, *3*). Special initial conditions, such as cross-field stimulation (*4*, *22*) or wave initiation in the vulnerable region of a preceding wave (*23*) can also give rise to spiral waves. In biological excitable media, however, spiral waves appear spontaneously without special initial conditions or induced wave breaks. The most common explanation for their occurrence involves the heterogeneity in refractoriness of the medium (*24*), although it is now known that impenetrable obstacles may also lead to spiral wave formation (*25*).

Spiral waves and rotating wave segments also arise in heterogeneous systems from the interaction of cells or clusters of cells with different oscillatory frequencies. The experiment and simulation shown in Fig. 3 utilized oscillatory media, initially homogeneous throughout the system. Each catalyst pattern exhibited bulk oscillations, with spurious wave initiations occurring at higher frequency sites, which were located in the smaller catalyst regions and at the catalyst boundaries. The resulting loss of synchronization gave rise to the rotating wave sources shown in the experimental and calculated images (*26*). Several mechanisms could give rise to spiral waves in such asynchronous oscillatory media, for example, wave initiation in the vulnerable region of a precursor wave. The spiral waves in Fig. 1, A and B, also appeared spontaneously, and such spiral organizing centers were common in all the patterned media. Spiral centers form spontaneously in other cellular media, including the slime mold *D. discoideum* (*8*) and a catalyst-bead BZ system (*27*).

Polygonal wave patterns have also been observed in the reaction of NO + H_2 on Rh(110), where state-dependent diffusion anisotropy gives rise to wave deformations (*28*). Elliptical waves are observed in heart tissue as a result of different propagation velocities along the long axis of the cells and in the transverse direction (*4*). The printed BZ-membrane system, with well-defined and easily varied catalyst patterns, offers a convenient and versatile system for the study of anisotropy and cellular inhomogeneities in excitable media. Our study has shown that inhomogeneities on small length scales strongly influence global wave behavior, giving rise to patterns with pronounced anisotropy as well as spontaneous spiral wave sources. Such effects are undoubtedly present in the cellular media of excitable biological systems.

REFERENCES AND NOTES

1. J. D. Murray, *Mathematical Biology* (Springer, Berlin, 1989); A. T. Winfree, *When Time Breaks Down* (Princeton Univ. Press, Princeton, NJ, 1987).
2. R. J. Field and M. Burger, Eds., *Oscillations and Traveling Waves in Chemical Systems* (Wiley, New York, 1985); R. Kapral and K. Showalter, Eds., *Chemical Waves and Patterns* (Kluwer, Dordrecht, Netherlands, 1995); S. K. Scott, *Oscillations, Waves, and Chaos in Chemical Kinetics* (Oxford Univ. Press, Oxford, 1994).
3. A. N. Zaikin and A. M. Zhabotinsky, *Nature* **225**, 535 (1970); A. T. Winfree, *Science* **175**, 634 (1972).
4. J. M. Davidenko *et al.*, *Nature* **355**, 349 (1992).
5. J. Lechleiter, S. Girard, E. Peralta, D. Clapham, *Science* **252**, 123 (1991).
6. A. Gorelova and J. Bures, *J. Neurobiol.* **14**, 353 (1983).
7. A. T. Winfree, *The Geometry of Biological Time* (Springer, Berlin, 1980); B. J. Welsh *et al.*, *Nature* **304**, 611 (1983); A. T. Winfree, *Chaos* **1**, 303 (1991).
8. O. Steinbock, F. Siegert, S. C. Müller, C. J. Weijer, *Proc. Natl. Acad. Sci. U.S.A.* **90**, 7332 (1993).
9. A. T. Winfree, *Science* **266**, 1003 (1994); N. Wiener and A. Rosenblueth, *Arch. Inst. Cardiol. Mex.* **16**, 205 (1946).
10. L. Clerc, *J. Physiol. (London)* **255**, 335 (1976); J. P. Keener, *J. Math. Biol.* **29**, 629 (1991); A. V. Panfilov and J. P. Keener, *Int. J. Bifurcation Chaos* **3**, 445 (1993); P. M. F. Nielsen *et al.*, *Am. J. Physiol.* **260**, H1365 (1991).

11. M. Delmar *et al.*, *Circ. Res.* **60**, 780 (1987).
12. A. Lázár, Z. Noszticzius, H. Farkas, H.-D. Försterling, *Chaos* **5**, 443 (1995); A. Lázár, Z. Noszticzius, H.-D. Försterling, Zs. Nagy-Ungvárai, *Physica D* **84**, 112 (1995).
13. T. Yamaguchi, L. Kuhnert, Zs. Nagy-Ungvarai, S. C. Müller, B. Hess, *J. Phys. Chem.* **95**, 5831 (1991).
14. Solutions of the catalyst $Fe(batho)_3^{2+}$ were prepared by dissolving 50.0 mg of 4,7-diphenyl-1,10-phenanthroline (known as bathophenanthroline) and 31.4 mg of $FeSO_4 \cdot 7\ H_2O$ in 10.0 ml of glacial acetic acid. Approximately 5 ml of the filtered catalyst solution (filter pore size, 0.45 μm) were pipetted into a clean, dry printer cartridge (HP51626A), which was resealed. The cartridge was used with a Hewlett Packard DeskJet 520 to print the catalyst patterns onto the polysulphone membranes (Gelman Supor-450).
15. The gel was prepared by mixing 10 ml of liquid agar (Agar-Agar; Fluka, New York) with 10 ml of BZ solution (without catalyst) in a thermostated Petri dish (diameter, 8.5 cm) maintained at 25.0 ± 0.2°C. Resulting initial composition: 1.5% agar, $[NaBrO_3]$ = 0.26 M, [malonic acid] = 0.17 M, [NaBr] = 0.10 M, and $[H_2SO_4]$ = 0.31 M (Fig. 1) or 0.39 M (Fig. 3).
16. J. J. Tyson and P. C. Fife, *J. Chem. Phys.* **73**, 2224 (1980); J. P. Keener and J. J. Tyson, *Physica D* **21**, 307 (1986).
17. Functions f and g for the catalyst-loaded areas are defined as $f(u, v) = (1/\epsilon)[u - u^2 - fv(u - q)/(u + q)]$ and $g(u, v) = u - v$. Catalyst-free regions were described by Eq. 1 with $f(u, v) = (1/\epsilon)(-u^2)$. The Laplacian was approximated by a nine-point formula; parameters: ϵ = 0.05 and q = 0.002.
18. The retarded decay of $HBrO_2$ in catalyst-free regions is an intrinsic feature of the model and is consistent with the Field-Körös-Noyes mechanism of the BZ reaction [R. J. Field, E. Körös, R. M. Noyes, *J. Am. Chem. Soc.* **94**, 8649 (1972)]. It reflects the absence of the catalyzed production of the inhibitor bromide in these regions. One-dimensional simulations with the three-variable Oregonator model [R. J. Field and R. M. Noyes, *J. Chem. Phys.* **60**, 1877 (1974)] showed the same qualitative behavior.
19. J. Jalife, *Pacing Clin. Electrophysiol.* **6**, 1106 (1983).
20. The catalyst-free strips were 0.5 mm in width and the experimental conditions were the same as in Fig. 1 except $[H_2SO_4]$ = 0.39 M. Gap penetration by BZ waves has also been observed in an immobilized-catalyst sol-gel system [I. R. Epstein, I. Lengyel, S. Kádár, M. Kagan, M. Yokoyama, *Physica A* **188**, 26 (1992)].
21. The length scale for the calculation corresponds to an approximately threefold enlargement except for the dot-density gradient. This scale was required to achieve sufficient accuracy in feasible computational times. The number of dots per wavelength in simulation and experiment is approximately the same.
22. A. T. Winfree, *J. Theor. Biol.* **138**, 353 (1989).
23. M. Gómez-Gesteira *et al.*, *Physica D* **76**, 359 (1994)
24. G. K. Moe, W. C. Rheinboldt, J. A. Abildskov, *Am. Heart J.* **67**, 200 (1964).
25. K. Agladze *et al.*, *Science* **264**, 1746 (1994); M. Gómez-Gesteira *et al.*, *Phys. Rev. E* **50**, 4646 (1994); A. Babloyantz and J. A. Sepulchre, *Physica D* **49**, 52 (1991); J. A. Sepulchre and A. Babloyantz, in *Chemical Waves and Patterns*, R. Kapral and K. Showalter, Eds. (Kluwer, Dordrecht, Netherlands, 1995), pp. 191–217.
26. The experimental system (Fig. 3A) evolved to the asymptotic behavior in only a few oscillations, whereas the simulated system (Fig. 3, B and C) required many cycles; this difference is likely the result of a greater role played by external fluctuations and imperfections in the experimental system.
27. J. Maselko and K. Showalter, *Physica D* **49**, 21 (1991).
28. F. Mertens and R. Imbihl, *Nature* **370**, 124 (1994).
29. We thank Z. Noszticzius and V. Gáspár for advice on loading polysulphone membranes with bathoferroin. We are grateful to the National Science Foundation (CHE- 9222616), the Office of Naval Research (N00014-95-1-0247), and the Petroleum Research Fund (29565-AC6) for supporting this research. O.S. thanks the Fonds der Chemischen Industrie for a Liebig Fellowship.

22 May 1995; accepted 10 July 1995

Logic gates in excitable media

Ágota Tóth and Kenneth Showalter[a)]
Department of Chemistry, West Virginia University, Morgantown, West Virginia 26506-6045

(Received 26 January 1995; accepted 4 May 1995)

The interaction of chemical waves propagating through capillary tubes is studied experimentally and numerically. Certain combinations of two or more tubes give rise to logic gates based on input and output signals in the form of chemical waves and wave initiations. The geometrical configuration, the temporal synchronization of the waves, and the ratio of the tube radius to the critical radius of the excitable medium determine the features of the logic gates. © *1995 American Institute of Physics.*

I. INTRODUCTION

Nonlinear chemical reactions provide simple models for excitable media in biological systems. Studies of spiral waves in the Belousov–Zhabotinsky[1] (BZ) reaction, for example, have contributed important insights into the nature of tachycardia and fibrillation in the heart muscle.[2,3] Chemical model systems for signal transmission might similarly offer insights into the excitable dynamics of neurons and neuronal networks.[4] Narrow channels such as capillary tubes, for example, can be considered as signal carriers in excitable chemical systems.[5–7] For a single capillary tube, an input wave gives rise to a response of either **1** (an output wave) or **0** (no output wave), as well as complex resonance patterns for successive input waves. In the case of a neuron, however, one input signal is usually not sufficient to produce an output signal, i.e., multiple inputs are typically necessary for a neuron to fire. In this paper, we study the output signals arising from two or more input signals, in the form of chemical waves propagating through narrow capillary tubes. The multiple inputs give rise to logic gates, where the particular gate depends on the geometrical configuration and the properties of the excitable medium.

Logic gates can be constructed by using physical quantities involving binary states. In electronic devices these states are generally represented by different voltages. In devices based on fluid dynamics, the pressure of fluid flow compared to atmospheric pressure determines the state.[8] In chemical systems, systematically designed single molecules can serve as OR and AND gates, with the change in fluorescence of a receptor molecule on binding different ions providing the basis of the binary coding.[9,10]

Logic gates are the realization of Boolean functions $(\wedge,\vee,')$ operating on binary input sets.[11] We will consider binary coded elements with the values **0** (FALSE) and **1** (TRUE) in two input channels. The response of different gates to all four combinations of the input sets are summarized in Table I. An OR gate, for example, yields the value **1** as the output if the value of either or both input channels is **1**. The AND gate gives a response of **1** only when both inputs are **1**. The response of an XNOR gate is **1** if both inputs are the same and **0** if they are different. The NOR, NAND, and XOR gates can be realized by combining the NOT function, which yields an output of **1** (**0**) for an input of **0** (**1**), with the OR, AND, and XNOR gates.

A number of studies have appeared on the use of nonlinear chemical systems for computational devices. Logic operations in a bistable chemical system were described by Rössler over 20 years ago.[12] Recently, Ross and co-workers[13–15] have proposed methods for constructing chemical computers with reactor systems coupled by mass flow. Various logic gates as well as simple computational devices were demonstrated. Schneider and co-workers[16,17] have reported numerical and experimental studies of logic gates constructed from bistable reactions in coupled CSTRs, with the coupling externally controlled to satisfy different neural networks corresponding to particular gates. Okamoto and co-workers[18] have considered certain enzymatic reactions as basic switching elements in neural networks.

We describe in this paper numerical and experimental studies of logic gates based on chemical waves propagating through capillary tubes in excitable BZ solutions. Traveling waves of excitation are the basis of the binary coding: The states **1** and **0** are defined by the presence or absence of a wave at certain fixed locations. The features of various gates are examined with a generic model for excitable media in Sec. II, and experimental examples of logic gates in the excitable BZ reaction are described in Sec. III. Combinations of basic gates to yield higher order functions are described in Sec. IV, and we conclude in Sec. V with a look at possible connections to neural behavior.

II. NUMERICAL STUDY

A. Model

We use the Barkley model,[19] a computationally efficient algorithm for describing excitable media, to examine various multiple-channel arrays numerically. The spatiotemporal evolution of the fast and slow variables u and v is governed by the reaction-diffusion equations

$$\frac{\partial u}{\partial t}=\nabla^2 u+f(u,v), \quad \frac{\partial v}{\partial t}=\nabla^2 v+g(u,v), \tag{1}$$

where the functions f and g describe the local dynamics

$$f(u,v)=\frac{1}{\epsilon}u(1-u)[u-u_{\mathrm{th}}(v)], \quad g(u,v)=u-v. \tag{2}$$

[a)]To whom correspondence should be addressed.

 0021-9606/95/103(6)/2058/9/$6.00

TABLE I. Output of logic gates for different input sets.

I_1	I_2	OR	AND	XOR	NOR	NAND	XNOR
1	0	1	0	1	0	1	0
0	1	1	0	1	0	1	0
1	1	1	1	0	0	0	1
0	0	0	0	0	1	1	1

TABLE II. Critical radius as a function of parameter a.

a	r_c
0.8	0.0438±0.001
0.7	0.0683±0.0005
0.6	0.0938±0.0005
0.55	0.114±0.001

The threshold $u_{th}(v)$ is defined as $u_{th}(v) = (v + b)/a$ and ϵ is a "small parameter" that determines the relative time scales of u and v. The variables of this generic model are analogous to the dimensionless concentrations of bromous acid and ferriin in the Tyson–Fife model[20] of the BZ reaction. The specific behavior is determined by the parameters a, b, and ϵ ; to mimic an excitable BZ system we choose $b=0.01$ and $\epsilon=0.02$ with $0.45<a<0.9$.

The partial differential equations were integrated by an explicit Euler method with the grid spacing $h=0.065$ and the time step $\Delta t=10^{-3}$. The two-dimensional Laplacian was approximated by a five-point formula, and no-flux boundary conditions were applied at the walls and corners. To model the experimental configuration for an AND or OR gate an area of 51×301 grid points was used, with channels of three grid points in width (or "inner diameter") and 50 grid points in length, as shown in Fig. 1. The channels were arranged in the middle of the grid with a distance of five grid points between the exits. In some calculations, this distance was varied by varying the number of grid points in the gap (and the overall system width). Planar waves were initiated periodically by setting the value of u to 0.7 for one time step in a strip three grid points wide at the left and right boundaries. The waves were monitored close to each channel entrance and far from each channel exit, as indicated in Fig. 1.

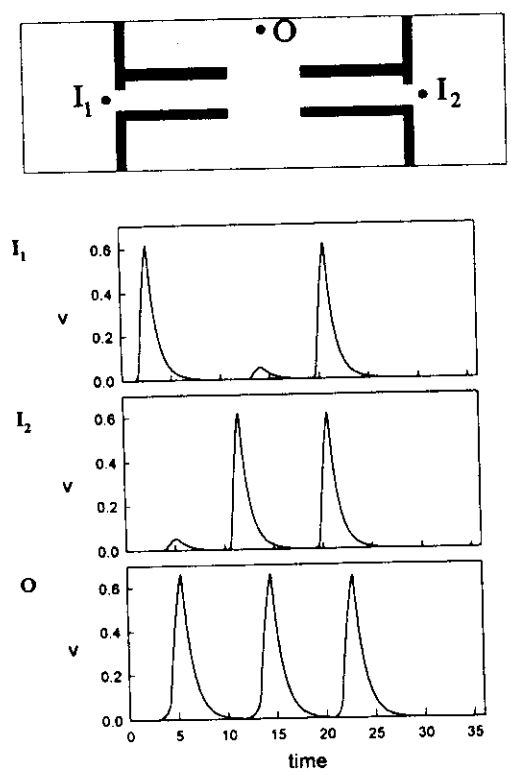

FIG. 1. Assembly for OR gate (top panel). Dots show monitoring sites of inputs I_1 and I_2 and output O. Time series show output of OR gate for different input signals. Top and middle time series correspond to inputs I_1 and I_2. Bottom time series shows output O for the corresponding inputs. Wave input period $\tau=9$, channel radius $r=0.065$, gap width $w=0.195$, and $a=0.6$.

B. Critical radius

The logic gates described here rely on an essential characteristic of excitable media: There exists a critical nucleation size for the successful initiation of wave activity. This is due to the dependence of wave velocity on front curvature, which is described to a good approximation by an eikonal relation,[21,22]

$$c=c_0+D\kappa, \tag{3}$$

where c is the normal wave velocity, c_0 is the planar wave velocity, D is the diffusion coefficient of the autocatalyst u, and κ is the curvature of the front. In an expanding region of excitation, the wave velocity is reduced due to the enhanced diffusive dispersion of the autocatalyst in the convex wave front (with $\kappa<0$). The normal wave velocity approaches zero as the radius of curvature ($r=1/|\kappa|$) approaches a critical value, which, from Eq. (3), is given by $r_c=D/c_0$. Regions of excitation with $r>r_c$ expand to form outwardly propagating waves, while regions with $r<r_c$ collapse. Although the eikonal equation is strictly applicable only for waves with slight curvature, it provides a remarkably good estimation of critical nucleation radius (where curvature is high). Experimental measurements of the critical nucleation radius have been made from BZ waves propagating through microcapillary tubes,[7] in which the hemisphere of excitation at the tube exit was assumed to have the same radius as that of the tube.

The planar wave velocity in the Barkley model can be varied by changing the parameter a. An increase in a results in a higher wave velocity, and, based on the eikonal equation, a smaller critical radius. For a given grid spacing, the critical radius can therefore be determined as a function of the parameter a. Table II shows values of critical radius determined for a single channel; we discuss below how the critical radius also depends on the gap width in the AND/OR configuration. The values show that the (fixed) channel radius of 0.065 is above the critical radius for $a\gtrsim 0.70$. For these values of a any wave propagating into the channel gives rise to the initiation of a wave at the channel exit. (The no-flux boundaries are defined by reflecting two rows of grid points on either side of the boundary; the radius of a channel three grid points in width is therefore $(2\times0.065)/2=0.065$.)

We also note that the half-width of the gap between the channel exits must be above the critical radius for the wave to expand into the middle chamber.

C. OR and AND gates

Figure 1 shows the configuration for the OR gate, where the channel radius is greater than the critical radius for the values of a and gap width. The top, middle, and bottom time series correspond to the input channels on the left and right, I_1 and I_2, and the output, O. From the response at the output to various input sets, we see that the system operates as an OR gate. Hence, an input of **1** in either or both channels results in an output of **1**.

In the case of only one input, the wave initiated from the channel can cross the output compartment and enter the second channel, which gives rise to a spurious wave initiation in the second compartment. To prevent this possibility, the half-width of each channel at its entrance was reduced to a value below the critical radius. This was accomplished by simply decreasing the width at each channel entrance by one grid point, as shown in Fig. 1. Thus when a wave is initiated in the middle chamber and enters the other channel, it is unable to propagate past the restricted channel entrance. The small perturbations in the time series in Fig. 1 are due to such waves collapsing at the restricted channel entrance.

On decreasing the value of a and thereby the wave velocity such that the channel radii are just below the critical radius, no output wave can be initiated from a single input wave. Two simultaneous input waves, however, give rise to the initiation of an output wave in the middle compartment. Figure 2 shows the configuration for the AND gate, which is the same as the OR gate except the value of a is slightly smaller. The output O, shown in the bottom time series, is **1** only if both inputs, I_1 and I_2, shown in the top and the middle time series, are also **1**. For a single input, the wave collapses at the channel exit in the middle compartment, which is seen in the other time series as a small perturbation. At still lower values of the parameter a, wave initiation does not occur at all in the central chamber, i.e., the output is **0** for all inputs.

Figure 3 shows the input-output response as a function of parameter a and the gap width w. The boundary between the AND and OR gate behavior represents values of a and w for which the channel radii are equal to the critical radius. For large gap widths, the value of a corresponding to the critical radius is similar to that for a single channel. For smaller gap widths, OR gate behavior is exhibited for values of a below that corresponding to the single channel critical radius. The restricted diffusion in the gap (compared to the unrestricted diffusion at the exit of a single channel) gives rise to smaller values of the effective critical radius. We also see AND gate behavior at lower values of a for small gap widths. At the opposite extreme of large gap widths, w must be small enough for two subcritical regions of excitation to combine to initiate a wave; no AND gate behavior is observed for $w>3$. Another factor that influences the output is the width of the wave, which increases with increasing a. Figure 4 shows the input–output response as a function of the ratio of gap width to wave width. (Wave width was determined by measuring the width of the u concentration profile at half its maximum amplitude.) The maximum value of this ratio for AND gate behavior is less than 0.5, indicating that substantial overlap of the regions of excitation is necessary for wave initiation.

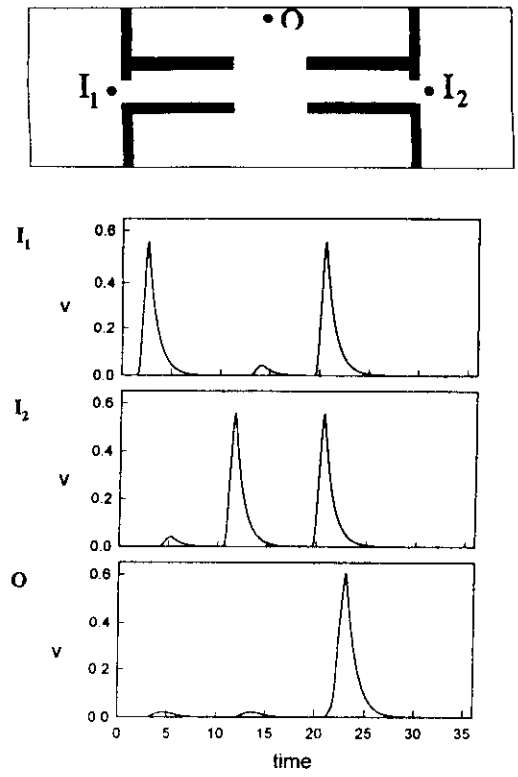

FIG. 2. Assembly for AND gate (top panel). Time series show output of AND gate for different input signals. The parameters are the same as in Fig. 1 except $a=0.55$.

Previous studies of wave propagation through single capillary tubes have shown that resonance patterns in the input–output response occur on varying the period of successive input waves.[7] We therefore anticipate the appearance

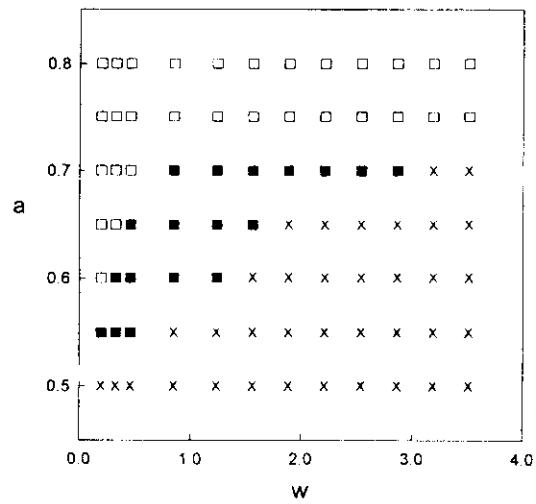

FIG. 3. Input–output response as a function of parameter a and gap width w. OR gate behavior shown by □, AND gate behavior by ■, and no waves initiated in output compartment by ×.

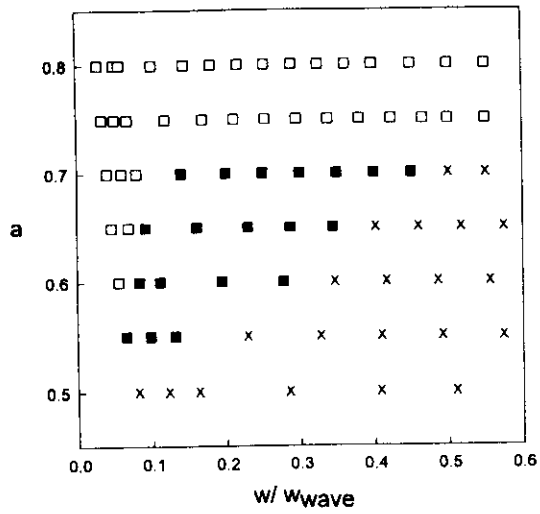

FIG. 4. Input–output response as a function of parameter a and ratio of gap width to wave width w/w_{wave}. OR gate behavior shown by □, AND gate behavior by ■, and no waves initiated in output compartment by ×.

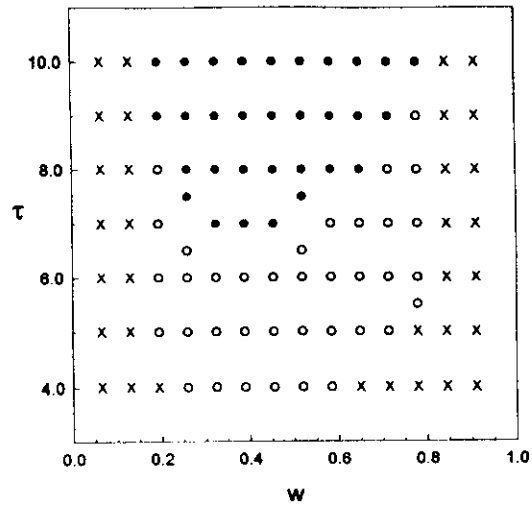

FIG. 6. Phase diagram showing resonance patterns for AND gate as a function of wave input period τ and gap width w. Patterns indicated by 1:1 (●), 1:2 (○), 0:1 (×). The parameters are the same as in Fig. 5.

of resonance patterns in the output response of the AND gate for successive input waves. The patterns can be characterized by the firing number fn,[23] defined as the ratio of the number of output waves to the number of input waves. On decreasing the period of the input waves, the system undergoes the bifurcations shown in Fig. 5. Each resonance pattern is characterized by $fn=(n-1)/n$, where n is the number of input waves and $(n-1)$ the number of output waves. As the input period is increased, the firing number rapidly approaches unity through a series of steps. This behavior is typical of forced excitable systems and can be characterized in terms of an interrupted circle map.[7,24] If the input period is decreased below the 1/2 resonance, no output waves are observed, i.e., $fn=0/1$. Wave initiation is inhibited at the channel exits because the system does not recover sufficiently to support wave behavior. The restricted diffusion in the small gap and small wave velocities near the critical radius cause the recovery period to be longer than the wave input period. This behavior is reminiscent of propagation failure, which has been found in certain discrete[25,26] and forced[27,28] excitable systems.

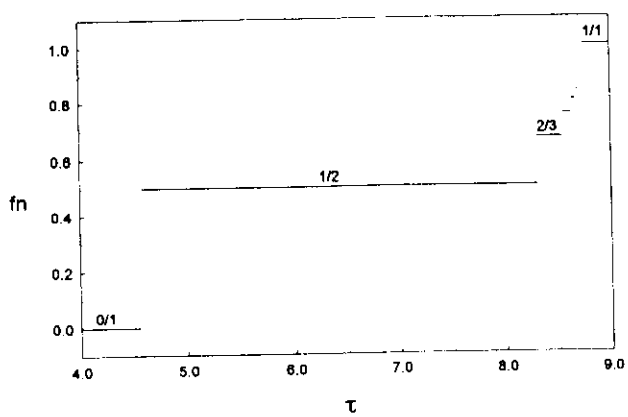

FIG. 5. Bifurcation diagram showing firing number fn as a function of wave input period τ for AND gate. The parameters are the same as in Fig. 2.

Figure 6 shows a phase diagram of the behavior for different input periods and gap widths, where only the 0, 1/2, and 1/1 resonance patterns are indicated. The bifurcation diagram in Fig. 5 appears in this diagram as the column at $w=0.2$. More complex patterns were also observed, where the firing numbers are characterized by Farey arithmetic sums of neighboring patterns.[29,30] For logic functions, we have restricted our study to the regime of simple behavior where $fn=1$. To ensure a firing number of unity, an input period of $\tau=9$ was used for each of the logic gates.

The timing of the input signals in the AND gate is of critical importance: Waves must enter the output chamber almost simultaneously for the successful initiation of a wave. If the arrival time differs by more than about 1% of the period, no output wave is observed. A limited study of the input–output response as a function of the arrival time difference revealed complex behavior over a narrow range of this parameter. Resonance patterns much like those in Fig. 5 are exhibited between the simple 1/1 response and the 0/1 response, where no output waves are observed.

D. NOT function and XNOR gate

Other types of gates can be created from assemblies with more than two channels. These are based on the observation that a phase difference between the input signals of an AND gate gives rise to an output signal of zero. We first consider the construction of a NOT function, in which an input of **1** results in an output of **0** and vice versa. This useful function can be connected in series with another gate to yield the opposite output for every input. Thus an AND gate followed by a NOT function generates a NAND gate, etc.

The configuration of a NOT function with three wave channels is shown in Fig. 7. The NOT function requires an internal periodic source to serve as a clock; therefore, two synchronized pacemakers, P, are incorporated in the left and right compartments. (A single periodic source would be sufficient in a configuration in which these compartments were connected.) The two pacemakers and coaxial channels con-

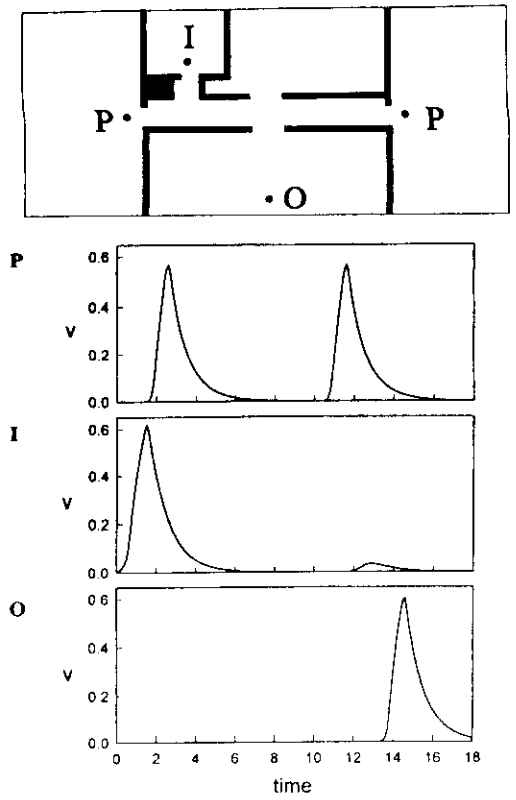

FIG. 7. Assembly for NOT function (top panel). Dots show monitoring sites of input I, output O, and periodic waves P. Time series show output of NOT function for different input signals. Top and middle time series correspond to periodic waves P and input I. Bottom time series shows output O for the corresponding inputs. The parameters are the same as in Fig. 2.

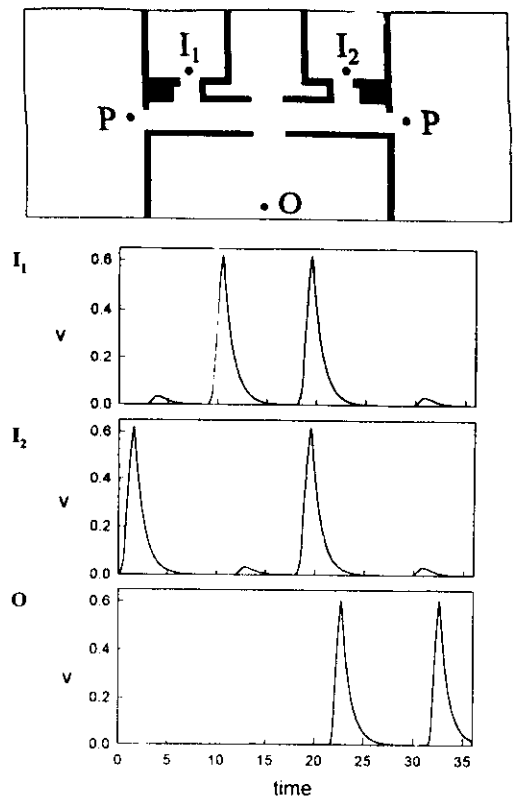

FIG. 8. Assembly for XNOR gate (top panel). Dots show monitoring sites of inputs I_1 and I_2, output O, and periodic waves P. Time series show output of XNOR gate for different input signals. Top and middle time series correspond to inputs I_1 and I_2. Bottom time series shows output O for the corresponding inputs. The parameters are the same as in Fig. 2.

stitute a periodic AND gate, with wave initiation occurring on the simultaneous arrival of the waves in the middle compartment. The input of the assembly is via the side channel. This is positioned so that the distance from the input to the exit in the middle compartment is shorter than the distance from each periodic source to the corresponding channel exit. The input signal is synchronized with the periodic sources so the signals respond in a 1:1 manner. The input wave therefore annihilates the signal from the left source and arrives at the middle chamber earlier than the signal generated by the right source. This temporal decoupling of the AND gate results in an output signal of **0** for an input signal of **1**. With no input signal, the periodic sources give rise to wave initiation; hence, an input of **0** generates an output of **1**.

The time series in Fig. 7 illustrates the action of the NOT function, showing the synchronous periodic sources P (top), the input signal I (middle), and the output signal O (bottom). The configuration qualitatively reverses the input signal: The result of an input wave is the absence of an output wave and vice versa. The calculations were carried out as described above, except the size of the domain was increased to 91 $\times$301 grid points.

An XNOR gate can be constructed by adding one more channel, as shown in Fig. 8. Based on the construction of the NOT function, two input channels are added to the AND gate in a symmetrical fashion. The time series show the output O for various combinations of the inputs, I_1 and I_2, where the calculations were carried out as in Fig. 7. The XNOR gate produces an output wave if both of the inputs are the same. Thus the output is **1** for inputs **1,1** or **0,0**, but **0** for inputs **1,0** or **0,1**.

III. EXPERIMENTAL STUDY

A. Procedures

The reaction mixtures were prepared as described previously,[7] with the exception of the metal catalyst. Instead of the anionic bathophenanthrolate complex used in our previous study, we used ferroin, prepared by mixing iron II-sulfate and 1,10-phenanthroline in a 1:3 mole ratio. The ferroin solution was standardized by measuring its optical absorbance at 510 nm (ϵ=11 100 M^{-1} cm^{-1}).[31] The polyimide coating of the capillary tubes (100 μm inner diameter, Polymicro Technologies) was removed by gentle heating over a Bunsen burner. The capillaries were then inserted through holes, with inner diameters matching the outside diameters of the tubes, drilled in Plexiglas blocks. Two Plexiglas-block barriers, each with mounted capillary tubes, were placed in a polycarbonate petri dish (10 cm diameter, Nalgene) so the gap between the coaxial tubes was ~0.5 cm. The Plexiglas barriers were sealed into place with acetone solvent. The capillary tubes were then carefully positioned such that the gap between them was ~200 μm.

A 12.5 ml solution was prepared with the concentrations given in Table III and swirled until an oxidation cycle was observed. The reaction mixture was then poured into the pe-

TABLE III. Reagent concentrations.

$NaBrO_3$	0.10–0.14 M
H_2SO_4	0.14 M
Malonic acid	2.0×10^{-2} M
Ferroin	1.0×10^{-2} M

tri dish, which was thermostated at 25.0±0.1 °C. Gaps between the Plexiglas barriers and the petri dish wall allowed the solution levels in the different compartments to quickly equalize. Absorption spectra of ferroin and ferriin showed that the largest difference in their molar absorptivities occurs at 510 nm. We therefore used a broad band interference filter with a 500 nm peak transmittance (Oriel) to monitor the waves. Details of the wave initiation and image processing techniques are described in Ref. 7.

B. Results

The critical radius r_c was first determined for an AND/OR gate assembly with a fixed gap width and capillary tube size. Because the planar wave velocity depends on $[BrO_3^-]$,[32] the critical radius can be varied continuously by changing the bromate concentration in the reaction mixture. Above a critical concentration, $[BrO_3^-]_c$, waves initiated in the right or left compartment give rise to wave initiation in the middle compartment at the tube exit. Below this concentration, no wave initiation is observed in the middle compartment for a single input wave. The critical bromate concentration $[BrO_3^-]_c = 0.11$ M was determined for tube radii of 50 μm and a gap width of 180 μm.

The radius of the capillary tube is above the critical radius for solutions with $[BrO_3^-] > 0.11$ M. If a wave enters one of the tubes, it propagates to the tube exit and a wave is initiated in the middle compartment, as shown in Fig. 9. When initiating waves simultaneously in the left and right compartments, we again observe an output in the form of wave initiation in the central compartment. This tube configuration therefore functions as an OR gate, provided the bromate concentration is above the critical value. An output signal of **1** is registered for input signals of (**1**,**0**), (**0**,**1**), or (**1**,**1**). The wave initiation in the central compartment is monitored far from the tube exits to ensure that the output signal represents a propagating wave.

The radius of the capillary is smaller than the critical radius for $[BrO_3^-] < 0.11$M. In solutions with bromate concentrations just below the critical value, no wave is initiated in the central compartment when a wave reaches the tube exit. As shown in Fig. 10, the small hemisphere of excitation collapses at the tube exit. Wave initiation in the central compartment becomes possible, however, with two simultaneous input waves. As shown in Fig. 11, waves initiated simultaneously in the left and right compartments result in an output signal of **1**. Thus the tube configuration now serves as an AND gate, provided the bromate concentration is only slightly below the critical value. An output signal of **1** is registered only for input signals of **1**,**1**; for input signals of **1**,**0** or **0**,**1** an output signal of **0** is registered.

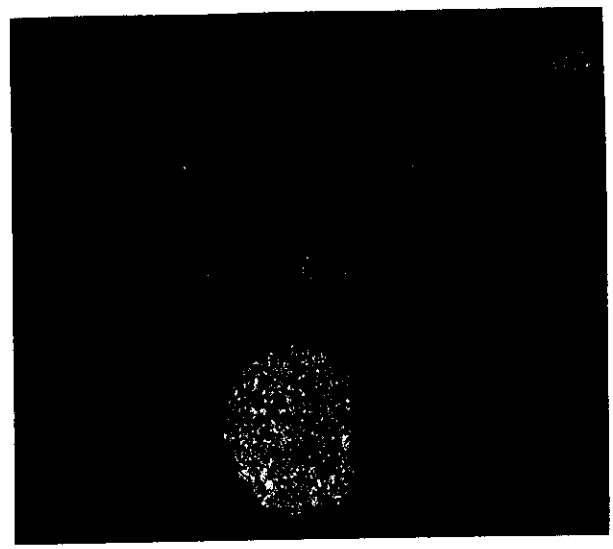

FIG. 9. Subtraction images showing a chemical wave at 10 s intervals traveling inside a capillary tube of 50 μm radius. Inputs of **0** (left tube) and **1** (right tube) with output of **1** demonstrate OR gate behavior. Concentrations given in Table III with $[BrO_3^-]=0.14$ M. Field of view showing middle compartment of AND/OR assembly: 0.38 mm×2.42 mm for top three panels and 0.82 mm×2.42 mm for bottom panel. The gap between the tube exits is 180 μm.

The timing of the input waves and the gap width are of critical importance in these experiments. Figure 12 shows the AND gate where the time between the appearance of the exiting waves is too large to support wave initiation. The first excitation collapses before the second develops, and no output wave is initiated. The outcome is similar if the tube exits are too far apart: The two hemispheres of excitation collapse in the gap even for simultaneous input waves. For successive wave initiations, no output signal is observed with high frequency input signals even when the timing and gap width are appropriate, since the recovery period for the excitable medium at each exit is longer than the wave initiation period.

FIG. 10. Subtraction images showing a chemical wave at 10 s intervals traveling inside a capillary tube. Inputs of **0** (left tube) and **1** (right tube) with output of **0** demonstrate AND gate behavior. Solution composition, distance between the tube exits and the tube radii are the same as in Fig. 9, except $[BrO_3^-] = 0.1085$M. Field of view showing middle compartment of AND/OR assembly: 0.38 mm×2.58 mm in each panel.

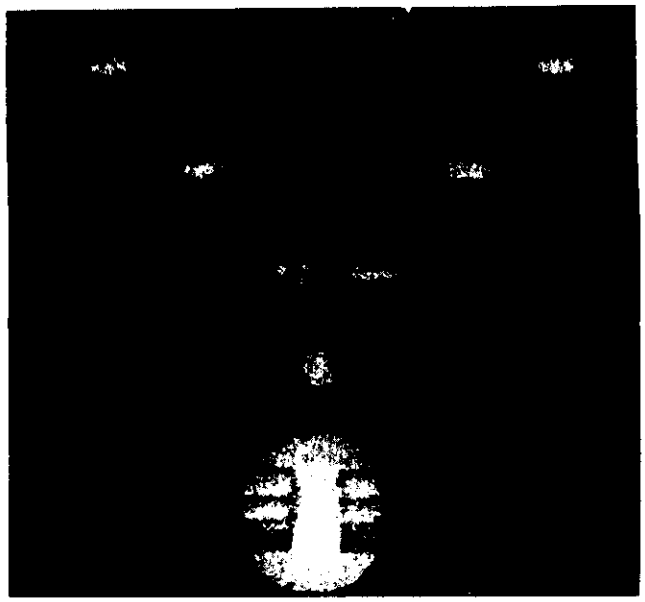

FIG. 11. Subtraction images showing chemical waves at 10 s intervals traveling inside capillary tubes. Inputs of **1** in both tubes with output of **1** demonstrate AND gate behavior. Conditions are the same as in Fig. 10. Field of view showing middle compartment of AND/OR assembly: 0.38 mm $\times$2.58 mm in top four panels and 0.64 mm$\times$2.58 mm in bottom panel.

IV. DISCUSSION

The spatial and temporal coupling of excitable elements can be used as the basis for logic gates. We have used chemical waves exiting from the ends of capillary tubes with radii near the critical nucleation radius as excitable elements. Two coaxial tubes through barriers separating a central output chamber from two input chambers form the basis of AND and OR gates. A slight adjustment in the reaction mixture composition is sufficient to convert the assembly from an OR gate to an AND gate and vice versa. Chemical analogues of

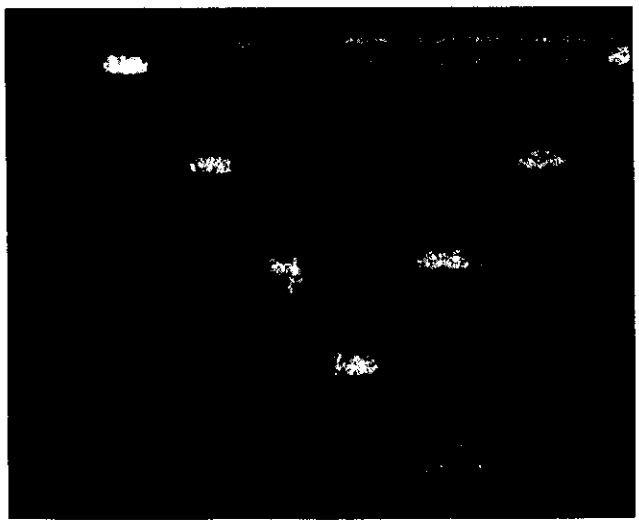

FIG. 12. Subtraction images showing chemical waves at 10 s intervals traveling inside capillary tubes. Inputs are **1** in both left and right tubes but with a delay of $\sim$10 s, resulting in an output of **0**. Conditions are the same as in Fig. 10. Field of view showing middle compartment of AND/OR assembly: 0.38 mm$\times$2.58 mm in each panel.

the NOT function and the XNOR gate can be constructed by adding periodic wave sources and additional wave channels to the AND/OR assembly. These gates are based on the input signals interfering with the synchronized internal periodic waves.

Other types of gates can be constructed by combining the above gates in various configurations. For example, the serial combination of an OR gate and a NOT function—where the output of the OR is the input of the NOT—yields a NOR gate. This composite gate gives an output of **0** for inputs of **(0,1)**, **(1,0)**, or **(1,1)** and an output of **1** for an input of **0,0**. A similar serial combination of an AND gate and a NOT function yields a NAND gate, with outputs opposite of the AND gate. Combining the XNOR gate with the NOT function yields the XOR gate to complete the basic gates listed in Table I.

The key element in all the gates, with the exception of the OR gate, is the union of two subcritical regions of excitation to initiate an output wave—the basis of AND gate behavior. The parameters affecting AND gate behavior are gap width, wave width, and the period and timing of the waves exiting into the output compartment. For a range of solution compositions (or values of a in the Barkley model), AND gate behavior is exhibited between a minimum and a maximum gap width. The minimum gap width is defined by twice the critical radius. Below this value, waves are unable to exit from the gap. Examples of this behavior are shown by the first two columns of values in Fig. 6, where $w<2r_c$. The maximum gap width is highly dependent on the wave width. For wave widths that are small compared to the critical radius we would anticipate the maximum gap width to be approximately $2\times r_c$, based on wave initiation arising from the combination of two subcritical hemispheres of excitation. Examination of Fig. 3 shows, however, that the gap width may be much greater than this for AND gate behavior, particularly as the channel (or tube) radius approaches the critical radius. This is because the wave width increases with increasing velocity (or value of a), and for very wide waves the region of excitation at the tube exit is substantially extended. Figure 4 shows that the ratio of gap width to wave width is less than 0.5 for the maximum value of AND gate behavior, indicating that significant overlap of the excitation regions must occur for wave initiation.

The arrival of the input signals at the channel exits must be nearly synchronous for AND gate behavior. Wave initiation does not occur when the arrival time differs by more than about 1%. The basis of the NOT and XNOR gates is a deliberate dephasing of the excitations via interference by the input signals. In the case of the NOT function, the input signal arrives at the output compartment slightly before the pacemaker signal, and no wave initiation can occur. This is also the case for the XNOR gate with inputs of **0,1** or **1,0**; however, with an input of **0,0** or **1,1** the signals are synchronized (even though from different sources) and the result is wave initiation in the output compartment.

The timing requirement of the AND gate can be used to generate an additional function—namely a frequency selector. For two input signals with different periods, output signals are observed only for the least common multiples of the

periods (provided the input signals are in phase). Thus the unknown frequency of one input signal could be determined by scanning through the frequency of the other input signal and monitoring the output signal.

The period of successive input waves determines whether the input and output signals have a simple 1:1 relationship or whether complex resonance patterns occur, as shown in Fig. 5. At high periods where $fn=1$, the system has sufficient time to relax to the steady state to function consecutively as an AND or OR gate. At lower periods, the firing number varies through a sequence of $(n-1)/n$ patterns. The complex behavior may allow further interesting input–output processing. The $(n-1)/n$ patterns occur in a stepwise fashion, each appearing over a range of input frequency, as shown in Fig. 5. As described in Ref. 7, each is a distinct pattern; for example, the 3/4 resonance is a repeating train of three "quarter notes" followed by a "quarter rest." Because ranges of the input frequency correspond to particular output patterns, the assembly could be used as a frequency coder.

At high frequencies, no output waves are generated beyond a threshold frequency of input waves. Because the wave velocity approaches zero as the channel radius approaches the critical radius, the relaxation to the steady state is slower at the channel exit than in the case of an unrestricted wave. Above the frequency threshold, wave initiation is inhibited because the system has no time to recover to its excitable state. The gap width also plays an important role in this behavior, since the diffusive dispersion of the autocatalyst is restricted as the gap width is decreased. This behavior is similar to propagation failure in discrete and forced excitable systems.[25–27]

Computational devices can be created by combining logic gates in particular arrays. For example, a binary adding machine can be made by operating an AND gate and an XOR gate in parallel. Thus inputs of **1,1** yield an output of **1** for the AND gate and **0** for the XOR gate, which interpreted as the binary output (10) yields the decimal sum of the inputs (1+1=2). Similarly, inputs of (**0,0**), (**0,1**), and (**1,0**) yield binary outputs of (00), (01), and (01), or the decimal sums 0, 1, and 1 of the inputs. Hjelmfelt, Weinberger, and Ross[14] have used the switching enzymatic model of Okamoto[18] to develop examples of a binary decoder, binary adder, and stack memory. Logic gates based on excitable media can be similarly combined to yield more complex computing devices.

V. CONCLUSION

We have studied logic gates based on the properties of excitable media, where the signals are coded by the presence or absence of chemical waves. Intriguing analogies can be drawn between the various gates we have considered and the simplest descriptions of nerve cell firing. Signals arriving on multiple axons are transferred via synaptic connections to the dendrites, which carry the excitation to the nerve cell body. The nerve fires, sending an action potential down its axon, when a threshold is reached from the accumulated signal input. Similarly, multiple signals are necessary for "firing" in an AND gate based on excitable media. We have studied assemblies based on two channels; however, it is easy to imagine AND type behavior arising in assemblies with many channels. The gate fires when a threshold is reached, determined by a sufficient region of excitation for the initiation of a wave. As a specific example of a multichannel gate, one can imagine adding a third channel to the AND gates in Figs. 2 or 11 to form a T-shaped assembly. The simultaneous input of three waves would transform parameter regions in Fig. 3 from no response to AND gate behavior (e.g., at $a=0.65$, $w=2.0$).

Another example of multiple input signals for triggering an output signal is seen in the complex $(n-1)/n$ resonance patterns with successive waves. The $fn=1/2$ pattern, for example, requires two input waves for every output wave. Thus n oscillations are necessary to trigger a burst of $n-1$ oscillations in an output wavetrain. This behavior is reminiscent of bursting behavior seen in certain single and coupled nerve cell assemblies.[33]

Finally, we note that while the above analogies apply to excitatory connections there is also behavior analogous to inhibitory connections. The "dephasing" caused by an input signal in the NOT and XNOR gates gives rise to an inhibition of wave initiation. The input channels can therefore be considered as "inhibitory connections" in these gates.

Logic gate assemblies become increasingly difficult to construct as multiple channels with special features are required. Other techniques, such as those developed by Noszticzius and co-workers,[34] where the catalyst is bound to a membrane in a desired pattern, might allow the construction of more complex gates. We also note that miniaturized assemblies could provide logic gates that operate on much faster time scales than the tube assemblies. Recent studies have shown that narrow channels can be created by using photolithography in the CO–platinum system.[35] It should be possible using similar methods to construct miniature logic gates based on excitable media in this system, thus providing faster chemical based computing devices.

ACKNOWLEDGMENTS

We thank Oliver Steinbock for helpful discussions on logic gates in excitable media and for critically reading the manuscript. We are grateful to the National Science Foundation (CHE-9222616) and the Office of Naval Research (N00014-95-1-0247) for supporting this research. Acknowledgment is made to the donors of The Petroleum Research Fund, administered by the American Chemical Society, for partial support of this research.

[1] A. N. Zaikin and A. M. Zhabotinsky, Nature (London) **225**, 535 (1970).
[2] A. T. Winfree, *The Geometry of Biological Time* (Springer, Berlin, 1980).
[3] J. M. Davidenko, A. M. Pertsov, R. Salomonsz, W. Baxter, and J. Jalife, Nature (London) **355**, 349 (1992).
[4] E. R. Kandel and J. H. Schwartz, *Principles of Neural Science* (Elsevier, New York, 1985).
[5] A. Babloyantz and J. A. Sepulchre, Physica D **49**, 52 (1991).
[6] A. Babloyantz and J. A. Sepulchre, Phys. Rev. Lett. **66**, 1314 (1991).
[7] Á. Tóth, V. Gáspár, and K. Showalter, J. Phys. Chem. **98**, 522 (1994).
[8] D. Bouteille and C. Guidot, *Fluid Logic Controls and Industrial Automation* (Wiley & Sons, New York, 1973).
[9] A. P. de Silva, H. Q. N. Gunaratne, and K. R. A. S. Sandanayake, Tetrahedron Lett. **31**, 5193 (1990).

[10] A. P. de Silva, H. Q. N. Gunaratne, and C. P. McCoy, Nature (London) **364**, 42 (1993).
[11] E. Mendelson, *Theory and Problems of Boolean Algebra and Switching Circuits* (McGraw-Hill, New York, 1970).
[12] O. E. Rössler, in *Physics and Mathematics of the Nervous System*, edited by M. Conrad, W. Güttinger, and M. Dal Cin (Springer, Berlin, 1974), pp. 399–418.
[13] A. Hjelmfelt, E. D. Weinberger, and J. Ross, Proc. Natl. Acad. Sci. USA **88**, 10983 (1991).
[14] A. Hjelmfelt, E. D. Weinberger, and J. Ross, Proc. Natl. Acad. Sci. USA **89**, 383 (1992).
[15] A. Hjelmfelt, F. W. Schneider, and J. Ross, Science **260**, 335 (1993).
[16] D. Lebender and F. W. Schneider, J. Phys. Chem. **98**, 7533 (1994).
[17] K.-P. Zeyer, G. Dechert, W. Hohmann, R. Blittersdorf, and F. W. Schneider, Z. Naturforsch. Teil A **49**, 953 (1994).
[18] M. Okamoto, T. Sakai, and K. Hayashi, Biol. Cybern. **58**, 295 (1988).
[19] D. Barkley, Physica D **49**, 61 (1991).
[20] J. J. Tyson and P. C. Fife, J. Chem. Phys. **73**, 2224 (1980).
[21] J. J. Tyson and J. P. Keener, Physica D **32**, 327 (1988).
[22] V. S. Zykov, Biophysics **25**, 906 (1980).
[23] L. Glass and M. C. Mackey, *From Clocks to Chaos* (Princeton, New Jersey, 1988).
[24] J. Finkeová, M. Dolnik, B. Hrudka, and M. Marek, J. Phys. Chem. **94**, 4110 (1990).
[25] J. P. Keener, J. Theor. Biol. **148**, 49 (1991).
[26] J.-P. Laplante and T. Erneaux, J. Phys. Chem. **96**, 4931 (1992).
[27] J. Kosek and M. Marek, J. Phys. Chem. **97**, 120 (1993).
[28] J. Kosek, I. Schreiber, and M. Marek, Philos. Trans. R. Soc. London A **347**, 643 (1994).
[29] J. Farey, Philos. Mag. J. (London) **47**, 385 (1816).
[30] J. Maselko and H. L. Swinney, J. Chem. Phys. **85**, 6430 (1986).
[31] A. A. Schilt, *Analytical Applications of 1,10-phenanthroline and Related Compounds* (Pergamon, London, 1969).
[32] R. J. Field and R. M. Noyes, J. Am. Chem. Soc. **96**, 2001 (1974).
[33] M. Colding-Jørgensen, in *Complexity, Chaos, and Biological Evolution*, edited by E. Mosekilde and L. Mosekilde (Plenum, New York, 1991).
[34] A. Lázár, Z. Noszticzius, H.-D. Försterling, and Zs. Nagy-Ungvárai, Chaos (to be published).
[35] M. D. Graham, I. G. Kevrekidis, K. Asakura, J. Lauterbach, K. Krischer, H.-H. Rotermund, and G. Ertl, Science **264**, 80 (1994).

Wave-Induced Chemical Chaos

John H. Merkin,[1] Valery Petrov,[2] Stephen K. Scott,[3] and Kenneth Showalter[2]
[1]*Department of Applied Mathematical Studies, University of Leeds, Leeds, LS2 9JT, United Kingdom*
[2]*Department of Chemistry, West Virginia University, Morgantown, West Virginia 26506-6045*
[3]*School of Chemistry, University of Leeds, Leeds, LS2 9JT, United Kingdom*
(Received 25 September 1995)

Spatiotemporal chaos in a two-variable, cubic autocatalator model with equal diffusivities of the species is described. The interplay between an unstable homogeneous state and propagating fronts which return the system to that state gives rise to a reinjection mechanism for chaotic behavior. Extreme sensitivity to initial conditions in both space and time and a rapid falloff of the spatial correlation function are exhibited in the chaotic regime.

PACS numbers: 82.40.Bj, 05.45.+b

Spatiotemporal chaos may arise in distributed reaction-diffusion systems by several different dynamical processes [1]. Mixed-mode chaos [2], for example, occurs when a Hopf instability of the stationary state interacts with a diffusion-induced Turing instability [3]. The stationary Turing pattern loses temporal stability when the ratio of the diffusivities for the inhibitor and the activator species becomes sufficiently small. As this ratio is further decreased, the Turing and Hopf modes increasingly mix to give rise to turbulent behavior. In this Letter, we describe spatiotemporal chaos in a reaction-diffusion system that arises from a mechanism distinctly different from this scenario or other scenarios such as phase turbulence or defect mediated turbulence [4,5]. We study a two-variable, cubic autocatalator model [6] in an open spatial reactor—with equal diffusion coefficients of the species. Reaction-diffusion structures emerge from an initial traveling wave, which persist indefinitely in a self-sustaining dynamical process having all the features of spatiotemporal chaos.

The governing reaction-diffusion equations for the open, unstirred autocatalator [7,8] can be written in the following dimensionless form:

$$\frac{\partial \alpha}{\partial t} = \delta \frac{\partial^2 \alpha}{\partial x^2} + 1 - \alpha - \mu \alpha \beta^2, \tag{1a}$$

$$\frac{\partial \beta}{\partial t} = \frac{\partial^2 \beta}{\partial x^2} + \mu \alpha \beta^2 - \phi \beta, \tag{1b}$$

where α and β are the dimensionless concentrations of the reactant A and autocatalyst B, respectively, and μ and ϕ are parameters related to the residence time and autocatalyst decay step. The parameter δ is the ratio of the diffusion coefficients D_A/D_B. Throughout this work we take $\delta = 1$: the equal diffusivities case.

Reaction occurs over the domain $0 \le x \le x_0$, subject to the following initial conditions:

$$\alpha = 1, \ \beta = \beta_0 g(x) \quad \text{for } t = 0,$$

where $g(x)$ is some function with compact support representing a localize input of the autocatalyst. Zero flux boundary conditions are imposed at $x = 0$ and $x = x_0$.

The bifurcation structure of the spatially homogeneous system has the following important features (see Fig. 1). (i) There are three possible steady state solutions: the "unreacting" or extinguished state, $(\alpha_s, \beta_s) = (1, 0)$, and a pair of nonzero states, $(\alpha_s^{\pm}, \beta_s^{\pm})$, given by

$$\alpha_s^{\pm} = \frac{\mu \mp \sqrt{\mu^2 - 4\mu\phi^2}}{2\mu},$$

$$\beta_s^{\pm} = \frac{\mu \pm \sqrt{\mu^2 - 4\mu\phi^2}}{2\mu\phi}, \tag{2}$$

which exist for $\mu \ge \mu_{sn}$. The locus of saddle-node points is given by $\mu_{sn} = 4\phi^2$. (ii) The $(1, 0)$ state is a stable node for all parameter values. (iii) The (α_s^-, β_s^-) state is a saddle point. (iv) The (α_s^+, β_s^+) state has a Hopf bifurcation locus emerging from a double-zero eigenvalue

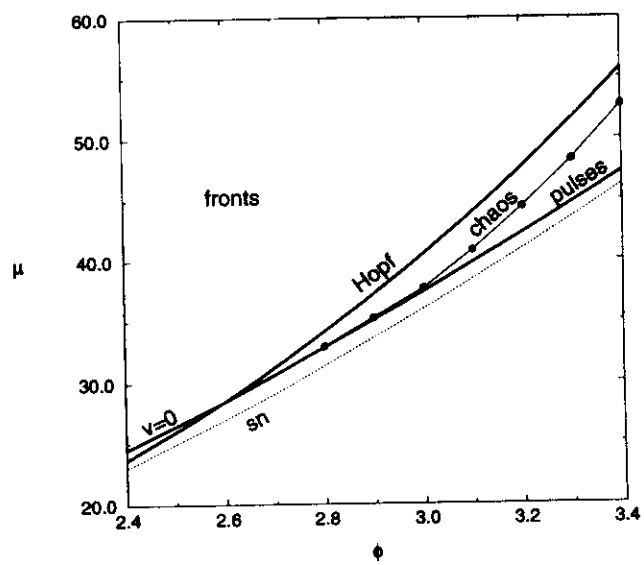

FIG. 1. Two-parameter bifurcation diagram. Simple propagating fronts are exhibited when the system is bistable, above the Hopf bifurcation line. The zero velocity line ($v = 0$) gives the lower boundary for the existence of propagating waves. The dotted line corresponds to the saddle-node bifurcation. Chaotic behavior is found in the area between the Hopf bifurcation line and the solid line with circles.

 0031-9007/96/76(3)/546(4)$06.00

point at $\mu = 16$, $\phi = 2$, given by

$$\mu_H = \phi^4/(\phi - 1), \quad \phi > 2, \tag{3}$$

with (α_s^+, β_s^+) being unstable for $\mu < \mu_H$. The bifurcation is subcritical (unstable limit cycle emerges in $\mu > \mu_H$) over the range $2 < \phi < 4$, which includes the range of interest here. For $\phi > 4$, the Hopf bifurcation is supercritical.

The reaction-diffusion equations, subject to the above initial conditions, allow for two different types of traveling wave solutions. First, there is a simple pulse which connects the (1,0) state ahead to the same state behind the propagating wave. Such a wave will pass across the reaction domain and be extinguished at the x_0 boundary, leaving the system uniformly in the (1,0) state. The second type of traveling wave connects the (1,0) state ahead to the (α_s^+, β_s^+) state behind, propagating with a characteristic velocity v. An important feature of this front structure is the damped oscillatory approach to (α_s^+, β_s^+) at the rear of the wave, which arises from the focal character of the steady state. The pulse and front solutions correspond, respectively, to homoclinic and heteroclinic connections in the α-β phase plane, and exist for particular regions of the μ-ϕ parameter plane. Of particular interest in the present context is the locus in the parameter plane for which the traveling wave front solution has zero velocity, shown along with the loci for the saddle-node and Hopf bifurcations in Fig. 1.

The detailed spatiotemporal behavior of this system has been determined by direct numerical integrations of Eqs. (1a) and (1b) for various parameter values. At larger μ, above the Hopf curve in Fig. 1, the (α_s^+, β_s^+) state is stable, and simple propagating fronts connecting this state and the initial (1,0) state are established from suitable, nonzero inputs of autocatalyst. For parameter values above the saddle-node curve but below the zero-velocity locus, the heteroclinic front solutions have negative velocity and cannot be established from the initial input conditions studied here. Complex spatiotemporal behavior is found in the region lying between the zero velocity locus and Hopf curve. This region can be divided into two subregions, one (at lower μ) corresponding to homoclinic pulse solutions connecting the (1,0) state to itself, the other to heteroclinic front solutions connecting the (1,0) and (α_s^+, β_s^+) states. The focal state is a *temporally unstable* state of the homogeneous system, so a uniform concentration behind the front corresponding to this state cannot be established. Instead, we observe complex spatiotemporal responses in this region of parameter values, which are initiated by the first front and sustained by subsequent fronts triggered by the system itself.

An example of the spatiotemporal evolution in this region is shown in Fig. 2. In this case, an initial input of autocatalyst is supplied over a narrow region close to the origin [$\beta_0 g(x) = 1$ for $0 \le x \le 0.33$]. After a short initial transient phase, the front propagates to the right with a constant velocity ($v \approx 0.79$ for $\mu = 38$ and $\phi = 3$) into

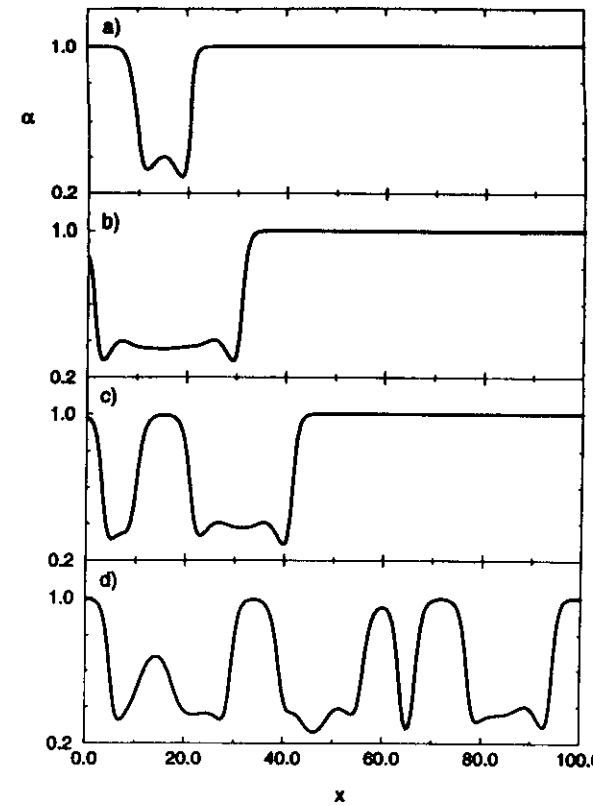

FIG. 2. Concentration profiles for α at different times after initiation at the left boundary: (a) $t = 10$, (b) $t = 24$, (c) $t = 38$, (d) $t = 120$. The width of the reaction zone is $x_0 = 100.0$ and $\phi = 3.0$, $\mu = 38.0$. The calculation was carried out by numerical integration of the 1D reaction-diffusion system 1(a) and 1(b) using a finite-difference approximation with 300 grid points over the spatial domain.

the region of high α. At the rear of the wave, there is an almost uniform region with a composition in the vicinity of the focal steady state; $(\alpha_s^+, \beta_s^+) = (0.3853, 0.2049)$ for these parameter values. The system then evolves away from this state in an initially divergent oscillatory manner. The subsequent evolution cause the system to evolve toward the (1,0) state, i.e., for the reaction to be extinguished locally. Figure 2(a) shows this state reestablished near the origin as the original front, now located at $x \approx 20$, propagates to the right. In the spatially uniform system, the (1,0) state would represent the global attractor and would be established asymptotically. In the spatially inhomogeneous situation, however, created by the progress of the initial reaction-diffusion wave, the local region of high reactant concentration is adjacent to a region of nonzero autocatalyst concentration. This situation allows a subsequent reaction-diffusion wave to develop, propagating now to the left into the region of high α, Fig. 2(b). Thus there is another reinjection of the system locally to the vicinity of the unstable steady state, (α_s^+, β_s^+). Also visible in Fig. 2(b) is the developing divergence from the unstable steady state over a region centered approximately on $x = 15$. This gives rise to a region with $\alpha \approx 1$ and $\beta \approx 0$, shown in Fig. 2(c), into

which a pair of fronts will subsequently propagate. Between this region and the original front, there is a further region, around $x \approx 30$, in which the system is evolving away from (α_s^+, β_s^+). The spatial asymmetry—arising as a consequence of spatially inhomogeneous initiation—is more clearly evident in this picture. Again, the system will approach the (1,0) state in this region, and a pair of inwardly propagating fronts will subsequently give rise to reinjections to the vicinity of the (α_s^+, β_s^+) state.

Figure 2(d) shows an example of the instantaneous α profile at a much later time. The original front has almost left the system on reaching x_0, but a complex and dynamic reaction-diffusion structure is sustained by repeated, spontaneous local extinction events followed by a wave-driven reinjection process.

The long-time evolution of the system is further illustrated in Fig. 3. In this space-time plot the concentration of the reactant is represented by a linear gray scale, where white corresponds to regions with $\alpha \approx 1$ and black to regions with $\alpha \approx 0$. The initial front propagates diagonally across the diagram with a constant slope characteristic of the wave velocity. The subsequent localized extinction events lead to patches near the (1,0) state. These have approximately triangular shape, reflecting the constant velocity of the subsequent reaction-diffusion fronts propagating into these regions. The velocities of the subsequent fronts are similar to that of the original front.

The system does not achieve a regular spatial pattern, although some indication of a characteristic wavelength can be seen. There are phases of almost periodic evolution over localized regions, for instance, in the vicinity of the origin for $600 < t < 900$ and for much of the evolution at the right-hand boundary, but these are interspersed with aperiodic "bursts" of larger-scale extinction events. To test this aperiodicity for the characteristics of chaos, the single-point spatial correlation function was determined

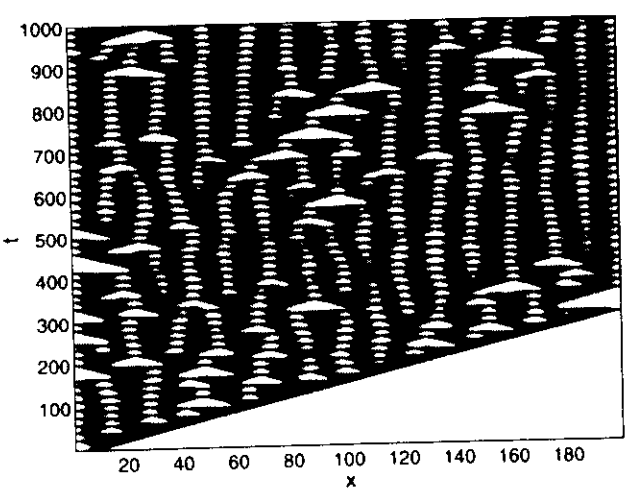

FIG. 3. Space-time plot of α in the chaotic regime, where white corresponds to $\alpha = 1.0$ and black to $\alpha = 0.0$. The front was initiated at the left boundary at $t = 0$; parameter values are the same as in Fig. 2 except the width of the reaction zone is $x_0 = 200.0$.

relative to the midpoint of the domain and the resulting correlation length l_{corr} was evaluated. The correlation falls off rapidly, with $l_{\text{corr}} = 3.2$. This value is consistent with the minimum domain length for which complex spatiotemporal responses were observed, $x_{0,\min} \approx 2l_{\text{corr}}$.

Sensitivity to initial conditions was also demonstrated. Two identical systems were computed until the post-transient behavior was established. A localized, small perturbation was then imposed on one system, and the difference in the subsequent evolution of the two systems was monitored. Not only is there a local exponential divergence of the two systems, but they also rapidly become spatially uncorrelated. These tests provide strong evidence for the existence of spatiotemporal chaos in this system for these parameter values.

The chaotic behavior is observed over a finite region in the μ-ϕ parameter plane, as indicated in Fig. 1, but there are smooth qualitative changes in the character of the spatiotemporal evolution within this domain. For parameter values close to the Hopf locus, which also marks the upper boundary for the region of chaotic behavior, the system exhibits spatially extended areas in the vicinity of the (α_s^+, β_s^+) state. These regions persist over long times, reflecting the near stability of this state, and are interspersed with widely spaced, localized bursts of extinction [approaching the (1,0) state]. The apparent wavelength of the structures also varies across the region, reflecting the dependence of the wave front velocity and the characteristic chemical time scale for the divergence from the (α_s^+, β_s^+) state on the system parameters.

A phase portrait obtained by plotting the variation of α with respect to β at a single point in the domain is shown in Fig. 4. Also shown on this figure are (i) the heteroclinic connection formed by the outset of the unstable focus (α_s^+, β_s^+) and the inset along the slow manifold to the stable node (1,0) of the ODE system (solid, heavy curve) and (ii) the heteroclinic connection from (1,0) to (α_s^+, β_s^+) formed by the constant-velocity, constant-form traveling wave front solution for this system (dashed curve). These two connections form a closed loop which plays an organizing role similar to that of homoclinic connections in the Sil'nikov mechanism for chaos [9,10]. The fixed-point eigenvalues associated with the divergence from the unstable steady state λ_+ and with the reinjection from the front connection λ_- have been calculated for various parameter values throughout the chaos region. Both are complex pairs in this region, with $\mathrm{Re}(\lambda_+) > 0$ and $\mathrm{Re}(\lambda_-) < 0$. The ratio of the magnitude of the real parts $|\mathrm{Re}(\lambda_-)|/\mathrm{Re}(\lambda_+)$ decreases from infinity at the Hopf locus [where $\mathrm{Re}(\lambda_+) = 0$] to a value that approaches approximately unity at the boundary between chaos and the pulse solution. Within the chaotic region of the parameter plane, therefore, the Sil'nikov criterion that the attracting manifold should have faster dynamics than the outset manifold appears to be satisfied, which is consistent with the existence of nearby chaotic orbits. This idea can be pursued further to explain, at least semiquantitatively, the

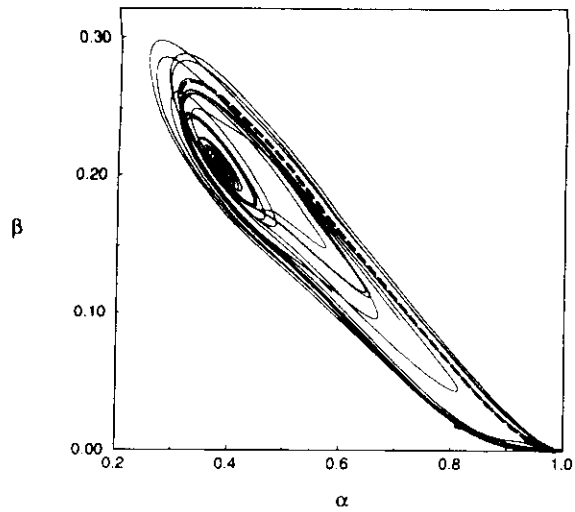

FIG. 4. The α-β phase plane for $\mu = 38.0$ and $\phi = 3.0$, with $x_0 = 100.0$. The thin line shows trajectories of the reaction-diffusion system taken at the middle of the reaction zone ($x = 50.0$). The heavy line represents the trajectory of the spatially homogeneous system spiraling out from the unstable focus. The heavy dashed line corresponds to the traveling wave solution of the reaction-diffusion system.

transition from chaotic behavior associated with the front reinjection mechanism to the simple, traveling pulse response. Within the region of chaos, the reinjection to the vicinity of (α_s^+, β_s^+) is stronger than the outward evolution along the unstable manifold, in the sense of the relative magnitudes of the inset and outset eigenvalues. The trajectories are therefore qualitatively altered by the unstable focus with a corresponding loss of phase information. In the pulse region, however, the instability of the (α_s^+, β_s^+) state is somewhat stronger and the reinjection weaker. The latter arises because the front velocity, which is involved as a multiplicative factor in the temporal eigenvalue, rapidly approaches zero as μ is decreased in the vicinity of the $v = 0$ locus. Trajectories are thus more effectively repelled from the focal region and return directly to the vicinity of $(1,0)$ without experiencing the phase loss near (α_s^+, β_s^+).

The spatiotemporal chaos reported here arises from the mixing of two distinct dynamical processes. Propagating fronts convert regions near the $(1,0)$ state, where little reaction occurs, to the vicinity of the (α_s^+, β_s^+) state, where both the extent of reaction and the autocatalyst concentration are significant. These regions would remain in this state were it not for the fact that it is an unstable state of the homogeneous system. Instead, the system spirals out from the unstable focal state to return to the $(1,0)$ state. The process is then repeated with fronts propagating into the new regions in the $(1,0)$ state. The behavior depends on inhomogeneous initial conditions, which in this study were in the form of an initial front. We note that the behavior is not dependent on the complete lack of reaction in the $(1,0)$ state. Calculations were also carried out with low concentrations of autocatalyst in the input stream, and the change of the stable steady state (of the ODE system) from no reaction to slight but finite reaction had essentially no effect on the wave-induced chaotic behavior.

An essential mechanistic feature of the chaos is the wave-mediated reinjection of the system to the unstable focus, a process reminiscent of the Sil'kinov mechanism for homoclinic chaos [9,10]. The chaotic behavior depends on the stable manifold of the (α_s^+, β_s^+) state being more strongly attracting than the unstable manifold is repelling. Phase information is lost as the system is injected into and then spirals out from the focal steady state. Chemical turbulence has also been studied by Kapral and co-workers [11,12] in the Brusselator and the complex Ginzburg-Landau equation for the case of equal diffusivities. This chaotic behavior develops in a two-dimensional medium from the interaction of vortices initiated by inhomogeneous, random initial conditions. The spatiotemporal chaos described here arises from the interplay between an unstable homogeneous state and propagating fronts which return the system to that state.

J. H. M. and S. K. S. wish to thank the Department of Chemistry, West Virginia University for their kind hospitality. K. S. is grateful to the National Science Foundation (CHE-9222616), the Office of Naval Research (N00014-95-1-0247), and the Petroleum Research Fund (29565-AC6) for supporting this research.

[1] M. C. Cross and P. C. Hohenberg, Rev. Mod. Phys. **65**, 851 (1993).
[2] A. DeWit, G. Dewel, and P. Borckmans, Phys. Rev. E **48**, R4191 (1993).
[3] A. Turing, Philos. Trans. R. Soc. London B **237**, 37 (1952).
[4] Y. Kuramoto, *Chemical Oscillations, Waves and Turbulence* (Springer, Tokyo, 1984).
[5] P. Coullet, L. Gil, and J. Lega, Phys. Rev. Lett. **62**, 1619 (1989).
[6] P. Gray and S. K. Scott, Chem. Engin. Sci. **39**, 1087 (1984).
[7] J. E. Pearson, Science **261**, 189 (1993); W. N. Reynolds, J. E. Pearson, and S. Ponce-Dawson, Phys. Rev. Lett. **72**, 2797 (1994); K.-J. Lee, W. D. McCormick, J. E. Pearson, and H. L. Swinney, Nature (London) **369**, 215 (1994).
[8] V. Petrov, S. K. Scott, and K. Showalter, Philos. Trans. R. Soc. London A **443**, 631 (1994).
[9] L. P. Sil'nikov, Sov. Math. Dokl. **6**, 163 (1965); **8**, 54 (1967).
[10] P. Gaspard and G. Nicolis, J. Stat. Phys. **31**, 399 (1983); P. Gaspard and X.-J. Wang, J. Stat. Phys. **48**, 151 (1987).
[11] X.-G. Wu, M.-N. Chee, and R. Kapral, Chaos **1**, 421 (1991).
[12] X.-G. Wu and R. Kapral, J. Chem. Phys. **94**, 1411 (1991).